Chapter 4
Hardware

In October 2008, a sensationalist newspaper headline was published, stating, "*Christmas could bring with it a new hazard as you wrap your gifts—X-ray-emitting sticky tape*" [1]. This was relating to the Nature publication by Camara et al. from UCLA, which stated that rapidly peeling off sticky tape would produce X-rays [2]. Based on this, the term "triboluminescence" (the phenomenon in which light is emitted when an object is rubbed, destroyed, or deformed) was coined and there were numerous reports where X-rays were actually detected. Camara et al. promptly founded a venture company named Tribogenics and developed a small-scale X-ray source based on triboluminescence. Within five years of their publication in Nature, they developed a miniature X-ray imaging device that weighed less than 2.5 kg, which was able to take X-ray images of electric calculators [3]. Progress in science and engineering devices relating to X-rays has been remarkable in recent years. We as users cannot remain ignorant to the latest technological trends as this is the era in which we currently live.

However, simply chasing after new things will not yield satisfactory measurements in X-ray tomography. This is because an X-ray CT scanner comprises various constituent devices and technical elements and, depending on its selection or setup/experimental conditions, the obtained 3D image quality may greatly decrease or phenomena that should be visible may no longer be at times. It is also attributable to the fact that the structural size of the observed subject and spatial resolution of the X-ray CT scanner are relatively similar. This aspect differs extremely from other highly generalizable observation devices that will produce some manner of observation so long as the indicated switch is turned on (e.g. light microscopes, various electron microscopes, etc).

The objective of this chapter is to assist in developing a fundamental understanding of instrument principles, types, and assessment methods, as part of a first step in selecting the constituent devices, understanding the technical elements, and correctly setting up the experimental conditions. Typical hardware that constitute an X-ray CT scanner are classified from X-ray generation to detection, are introduced here.

H. Toda, *X-Ray CT*,
https://doi.org/10.1007/978-981-16-0590-1_4

4.1 X-ray Source

4.1.1 X-ray Generation

Interactions between the electromagnetic wave and atoms were discussed in Sect. 2.1.2. An overview of the interactions between the *charged particle* beam, with a focus on electron beams, and the atoms is presented here.

(1) Bremsstrahlung

Figure 4.1 schematically shows the interactions generated at the level of a single atom when a high-speed electron is incident onto an object. Furthermore, Fig. 4.2 schematically shows the X-ray spectra emitted from the object at that time. Figure 4.1a–c shows *continuous X-ray* generation due to *bremsstrahlung* (the etymology is German. Pronounced [brɛmz˩ʃtra:lʊŋ]). Figure 4.2 shows that continuous X-rays are distributed across a wide energy range. These types of X-rays are referred to as *white X-rays*. Furthermore, we can see that the intensity increases as the energy becomes lower (dotted line in the figure).

In Fig. 4.1a, the electron directly collides with the nucleus. The electron loses all of its kinetic energy in a single collision, and X-rays are generated through *bremsstrahlung*. This generates high-energy X-rays. The upper limit of the spectra in Fig. 4.2 is regulated by this (so-called *Duane-Hunt law*). However, this occurrence is an extremely rare phenomenon and the X-ray intensity on the edge at the high-energy side in Fig. 4.2 is extremely small. The *tube voltage* V_a [V] of the X-ray tube and the electron charge e ($= 1.602 \times 10^{-19}$ C) are used to express the upper limit value E_{max} of the generated X-ray energy, which is expressed as follows:

$$E_{max} = eV_a \tag{4.1}$$

The peak value of tube voltage is expressed by kV and its units are often expressed as [kVp] but this text uses [kV] as units. As shown in Fig. 4.2, $E_{max} = 120$ keV when tube voltage $V_a = 120$ kV; $E_{max} = 100$ keV when $V_a = 100$ kV. As with the dashed line in Fig. 4.2, intensity varies while E_{max} remains the same when the tube voltage is the same and the object into which the electron collides is different. Incidentally, the use of solid lines in Fig. 4.2 assumes that the X-ray spectra were generated from an X-ray tube. The drop in X-ray intensity in the low-energy side in Fig. 4.2 is stipulated by the absorption of the X-ray by the target itself or in the window material of the X-ray tube. Recently, beryllium has frequently been used as a window material, and the drop in X-ray intensity in the low-energy side is in this case limited. Readers who require such data can calculate them using Eqs. (2.2) and (2.2) and the data in Table 2.10. Figure 4.2 shows extremely complex behavior, such as characteristic X-ray peaks (discussed later) and right-hand-side decay induced by the K absorption edge of the target material itself.

Figure 4.3 shows the average X-ray energy generated by *bremsstrahlung* as a function of the tube voltage of the X-ray tube [4]. Knowing the average energy is

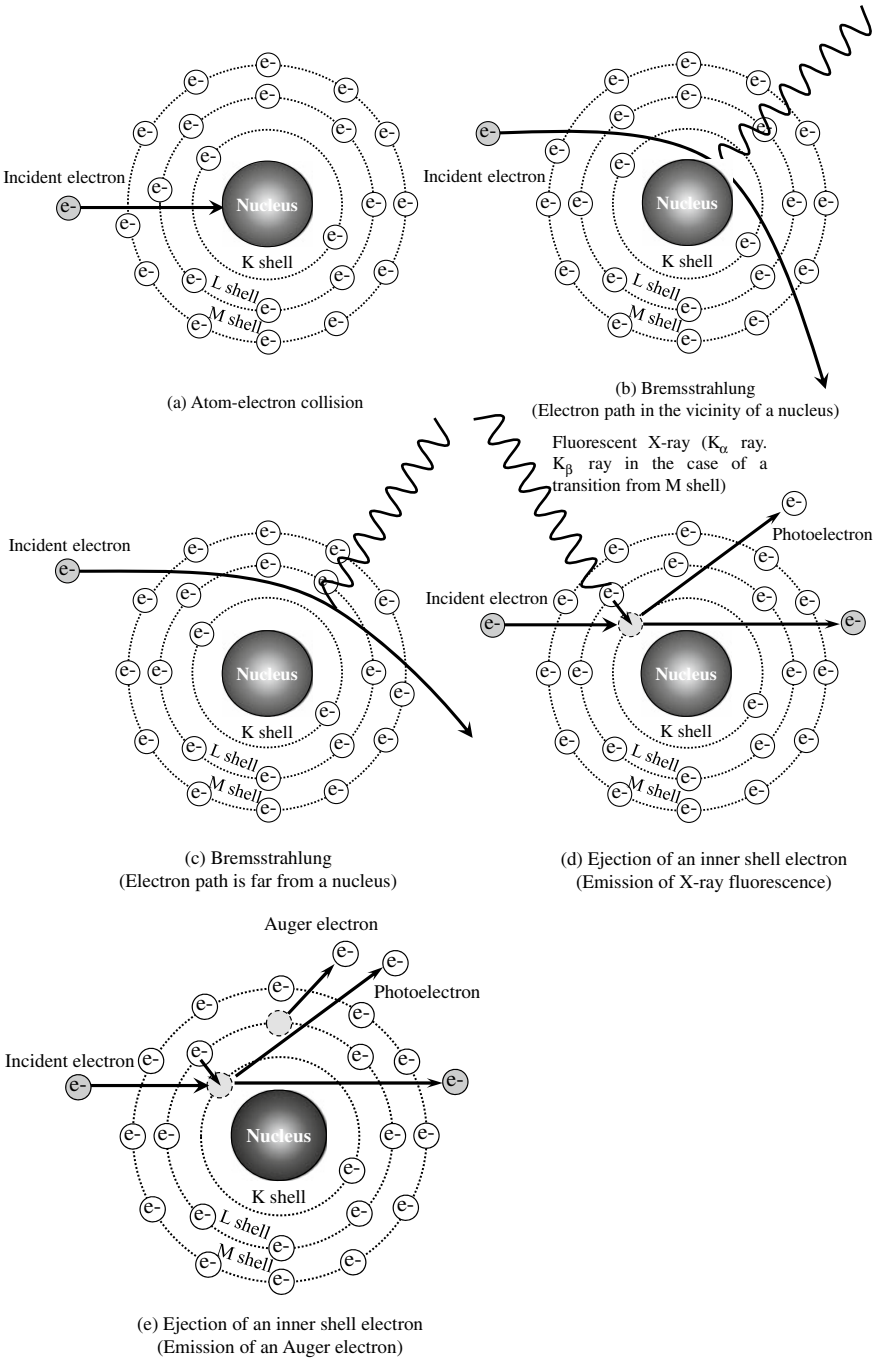

Fig. 4.1 Schematic of the various interactions between an accelerated electron and atom

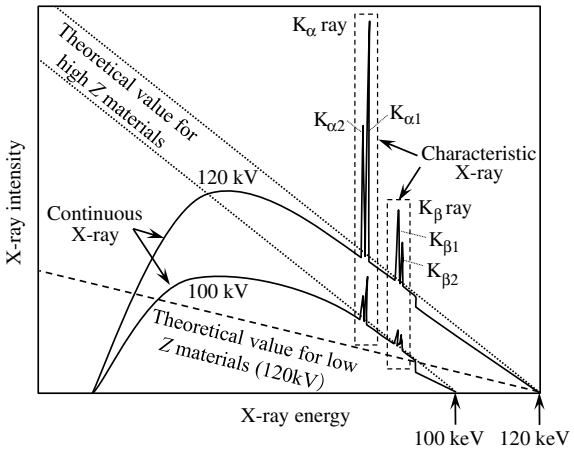

Fig. 4.2 Schematic of X-ray spectra obtained when an accelerated electron beam is incident to a metal target (dotted line). The dashed line shows the spectra formed when the electron collides into an object with low atomic number relative to the dotted lines and the solid lines show the X-ray spectra generated from the X-ray tube

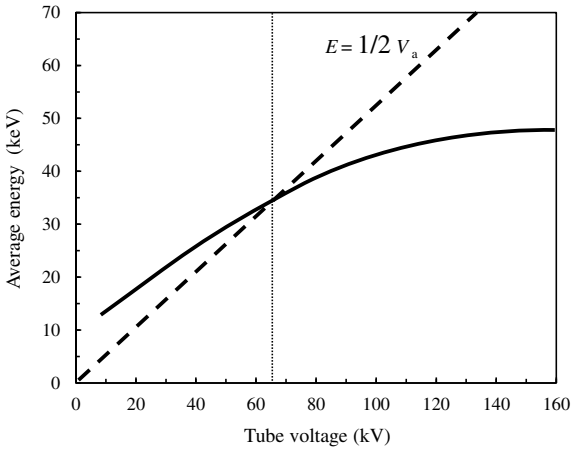

Fig. 4.3 Schematic of the relationship between the tube voltage and the average energy generated from *bremsstrahlung*. The dashed line in the figure shows the point at which X-ray energy is exactly ½ of the tube energy; the dotted line shows the intersection between that dashed line and the average energy [4]

useful for estimating the size of the sample that can be imaged and the tube voltage necessary for imaging, provided the linear absorption coefficient is investigated. At a tube voltage of approximately 60 to 70 kV, the average energy value is roughly half that of the tube voltage, a fact that should be borne in mind [4].

Incidentally, *bremsstrahlung* can occur even in charged particles other than electrons. Setting the incident charged particle mass and charge as m and ze, respectively, and the charge of the object as Ze (Z is the atomic number), then the total intensity I_b, where the X-ray intensities generated by *bremsstrahlung* are integrated across all energies and directions, is as follows [4]:

$$I_b \propto \frac{Z^2 z^4 e^6}{m^2} \tag{4.2}$$

For example, the masses of the proton and α particle (nucleus of the helium atom ^{4}He) are 1.8×10^3 and 7.3×10^3 times that of the electron, respectively. Thus, the *bremsstrahlung* due to the electron is several orders of magnitude larger than that from protons and α particles. Furthermore, Eq. (4.2) indicates that a high X-ray intensity can be obtained when metallic targets with a high atomic number are used.

If the electron does not collide with the nucleus, then it will pass through near the nucleus, as shown in Fig. 4.1b, c. In this case, the electron path is simultaneously curved and slowed in the Coulomb field of the nucleus. The accompanying X-ray generation, which occurs with *bremsstrahlung*, is the primary mechanism by which X-rays are obtained with X-ray tubes. The intensity of X-rays generated in this manner increases with the incident electron energy and atomic number of the object. When comparing Fig. 4.1b, c, the electron is curved and decelerated further in Fig. 4.1b, where the electron passes by closer to the nucleus. X-rays with higher energy are emitted as a result.

The ratio of the kinetic energy of the electron and *bremsstrahlung* energy is defined by the X-ray's *efficiency of bremsstrahlung production* η:

$$\eta = K Z V_a \tag{4.3}$$

Here, $K = 9.2 \times 10^{-7}$ (kV) is a constant [5]. This equation is obtained by dividing the X-ray energy generated per unit time $KZV_a{}^2 J$ (J is electric current) by the electron energy $V_a J$. When η is calculated with copper and tungsten when the tube voltage is 100 kV, the values become 0.27% and 0.68%, respectively; in other words, most of the input energy is dissipated as heat. Most of the energy transmitted to the object from the incident electron serves to ionize the object and does not generate X-rays. As such, the X-ray tube target experiences a considerable temperature increase. For this reason, the usage of metallic materials that are heat-resistant and can efficiently conduct heat to its surroundings is optimal. The melting point and thermal conductivity of various metals are provided for reference in Table 4.1 [9]. In that sense, materials like tungsten, which have a high melting point and superior thermal conductivity, are suitable target materials.

(2) Characteristic X-rays

In the case of Fig. 4.1d, electrons are ejected from the K-shell due to the incident electron, and the atom enters an *excited state*. As seen in Sect. 2.1.2, fluorescent

Table 4.1 Melting point, thermal conductivity, and work function of various metallic materials and electron-emitting materials [9]

Material	Melting point (°C)	Thermal conductivity (W/mK)	Work function (eV)
Ag	961	425	4.5
Cu	1083	397	4.6
Co	1478	96	4.4
Fe	1539	78.2	4.5
Rh	1967	148	4.7
Zr	1855	22.6	4.1
Mo	2622	137	4.2
W	3382	174	4.5
LaB_6	2210	47	2.8
TiC	3067	33.5	3.5
TaC	3983	21.9	3.8
HfC	3928	30	3.4
NbC	3600	15.0	3.8

X-rays are generated owing to the transition of an electron from an outer shell. The energy of fluorescent X-rays is dependent on the fluorescing atom and this is referred to as a *characteristic X-ray* due to the emission of an X-ray with an energy that corresponds to the difference in binding energy of the trajectory before and after the transition. For this reason, there is a minimum tube voltage necessary for generating characteristic X-rays in the case of X-ray tubes, which is referred to as an *excitation voltage*. Of these, the characteristic X-ray, which occurs due to an electron transition from the L-shell, is referred to as a K_α X-ray; those due to an electron transition from the M- or N-shells are referred to as K_β X-rays. The numerous sharp peaks shown in Fig. 4.2 correspond to these characteristic X-rays. Typically, K_α and K_β X-rays can be easily distinguished. They each have extremely narrow energy ranges, so characteristic X-rays are used for experiments where monochromatic X-rays are necessary. The relationship between characteristic X-ray energy E_c and atomic number Z of the object can be easily calculated with *Moseley's law* [6].

$$\sqrt{\frac{E_c}{R_y}} = (Z - \sigma_n)\sqrt{\frac{1}{n_1^2} - \frac{1}{n_2^2}} \tag{4.4}$$

Here, $R_y = 2.18 \times 10^{-18}$ J ≈ 13.6 eV and corresponds to the electron binding energy of the ground-state hydrogen atom ($Z = 1$). Furthermore, n_i is 1, 2, and 3 for the K-, L-, and M-shells, respectively. The term σ_n is a constant that corresponds to the correction term from the hydrogen atom model for multi-electron systems; σ_n is dependent on n_i and Z but $\sigma_n \approx 1$ when $Z < 30$. As such, this can be simplified in the following equation when only K_α X-rays are considered:

$$\sqrt{\frac{E_c}{R_y}} = (Z-1)\sqrt{\frac{3}{4}} \tag{4.5}$$

In Table 2.3, there are slight differences in energy even for electrons that follow the same trajectory. This is typically expressed with numbered subscripts. For example, of the L_I shell (2 s trajectory of the L-shell), L_{II} shell, and L_{III} shell (2p trajectory of L-shell) in Table 2.3, only the L_{III}- and L_{II}-shells can transition into the K-shell and are each distinguished with $K_{\alpha 1}$ and $K_{\alpha 2}$ X-rays, respectively. The $K_{\alpha 1}/K_{\alpha 2}$ intensity ratio is 2:1 [7] and it is used without distinction due to its extremely close values. A weighted average of the two values is used for the wavelength value in this case [7].

$$\lambda_{K_\alpha} = \frac{2\lambda_{K_{\alpha 1}} + \lambda_{K_{\alpha 2}}}{3} \tag{4.6}$$

Here, λ_{K_α}, $\lambda_{K_{\alpha 1}}$, and $\lambda_{K_{\alpha 2}}$ are each the wavelengths of the characteristic X-ray corresponding to the average value, L_{III}-shell, and L_{II}-shell, respectively. The K_β X-ray boasts only a fraction of their strength. The characteristic X-ray energy values corresponding to representative metallic elements used in the X-ray tube target are summarized for reference in Table 4.2 [8]. When X-rays are used for analysis, it is important to not only consider the atomic number dependencies of the intensities shown in Eq. (4.2), but also that the characteristic X-rays of the target material do not overlap with those of the sample to be analyzed. Furthermore, based on Tables 2.1 and 4.2, the K absorption edge of copper, for example, is 8.98 keV and its $K_{\alpha 1}$ and $K_{\alpha 2}$ are 8.05 keV and 8.03 keV, respectively. As such, the characteristic X-ray generated when copper is used as a target, is relatively minimally absorbed in the target material itself. However, when emitting X-rays from a copper target to a sample containing iron (K absorption edge of 7.11 keV) and cobalt (K absorption edge of 7.71 keV), both of which have slightly smaller atomic numbers than copper, the absorption of characteristic X-ray due to the sample significantly increases and background levels increase due to the generation of fluorescent X-rays.

Table 4.2 Energy values (units of eV) of characteristic X-rays for representative elements used in the X-ray tube target [8]

Atomic number	Element	$K_{\alpha 1}$	$K_{\alpha 2}$	K_α (Average)	$K_{\beta 1}$
24	Cr	5414.72	5405.51	5411.65	5946.71
26	Fe	6403.84	6390.84	6399.51	7057.98
27	Co	6930.32	6915.30	6925.31	7649.43
29	Cu	8047.78	8027.83	8041.13	8905.29
42	Mo	17479.34	17374.30	17444.33	19608.30
45	Rh	20216.10	20073.70	20168.63	22723.60
47	Ag	22162.92	21990.30	22105.38	24942.40
74	W	59318.24	57981.70	58872.73	67244.30

Returning from the excited state mentioned above, Auger electrons could be emitted like the case shown in Fig. 4.1e, which is also discussed in Chap. 2. The fluorescence yield, which expresses the probability of whether fluorescent X-rays or Auger electrons being generated, has already been summarized in Fig. 2.6 for many elements.

Figure 4.2 shows two spectra for X-ray tubes when its tube voltages are changed. When a high voltage is applied, the intensities of characteristic and continuous X-rays increase. The peak positions of characteristic X-rays are unique to the material and do not change but the peaks of the continuous X-rays shift to the high-energy side.

4.1.2 X-Ray Tube

The Crookes tube used during Roentgen's era generated electrons by discharging electricity between electrodes placed in a low-pressure gas. The structure of X-ray tubes widely used today is fundamentally identical to the Coolidge tube developed by the eponymous scientist in 1913. This section provides an overview of these constituent elements in order.

X-ray tubes are important constituent devices that stipulate the imaging capability or quality based on industrial X-ray CT scanners. The corresponding physics, which serve as its basis, are described in Sect. 4.1.1. The fixed anode X-ray tube shown schematically in Fig. 4.4 comprises a *filament*, which discharges electrons (*cathode*); the target, which produces the X-ray (*anode*); and the vacuum-sealed tube container, which envelops these elements and is kept at around 10^{-6} Pa. This is referred to as a

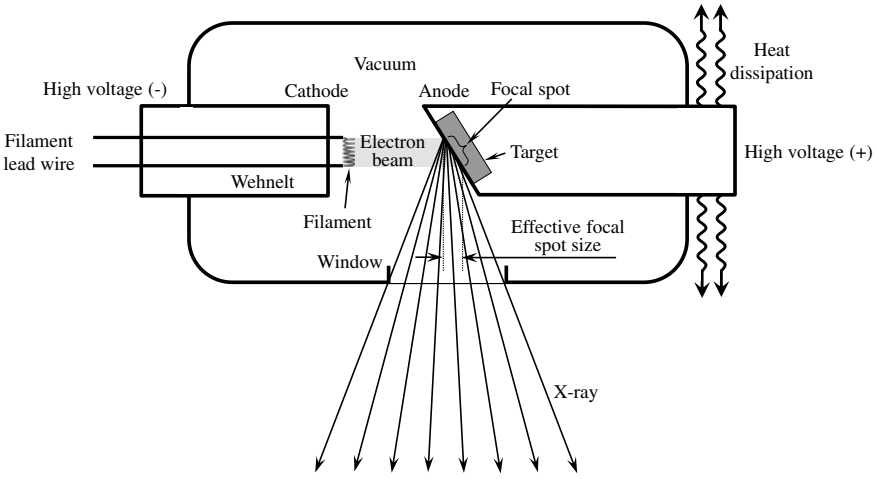

Fig. 4.4 Schematic of the fixed anode X-ray tube structure

sealed X-ray tube. Furthermore, there are also *open X-ray tubes*, which have a vacuum pump installed outside of the tube and constantly evacuate the tube interior with the pump. The target and filament can be replaced if an open system is used. A high voltage of around 500–600 kV is applied between the cathode and anode. Generally, the target is slanted in a single direction to irradiate the X-ray (reflection-type), and the generated cone-beam X-ray exits from the window portion. The window is made of either a thin glass or beryllium film (about 150–500 μm in the microfocus tube). Specialized carbon materials are also used in commercially available X-ray CT scanners shown later in Table 6.1; aluminum is also used for high-energy cases. Beryllium can be toxic and reacts with water, so care must be taken with regard to its handling. Furthermore, it is a light element at $Z = 4$, effectively transmitting X-rays. For example, a beryllium window of an approximately 500 μm thickness will transmit over 95% and 98% of X-rays with 10-keV and 20-keV energies, respectively. Some designs ensure that the thermally-conducting metals like copper are distributed and that air-cooling and even water-cooling or oil-cooling at times is installed to ensure that the high-temperature target is sufficiently cooled.

(1) Cathode

Electrons need to be obtained for X-rays to generate. Phenomena that result in the emission of electrons from metals include *thermionic emission*, photoelectron emission, field emission, and secondary electron emission. Of these, X-ray tubes primarily use *thermions*, which are obtained primarily from thermionic emission. Incidentally, this thermionic emission is also used in the electron guns of linear accelerators in synchrotron radiation facilities, vacuum tubes, and Braun tubes used in old televisions.

Thermionic emission is a phenomenon where applying energy to a free electron in the conduction band results in its overcoming the surface barrier and emission. Figure 4.5 schematically shows the relationship between the electron state density within metals as determined by the *Fermi-Dirac distribution* and potential of the cathode surface. The minimum energy needed for a single electron to jump into the vacuum is referred to as the *work function* ϕ. This corresponds to the difference between the Fermi level and vacuum level shown in Fig. 4.5. Furthermore, this ϕ value is known to vary by metal. Table 4.1 shows the work function values for representative materials used when generating thermions [9]. As indicated by the dashed line in Fig. 4.5, the area below the Fermi level is completely filled with electrons at a temperature of absolute zero and the existence probability of electrons that have energy above this is zero. Electrons at the Fermi level will be emitted into the vacuum if they obtain energy greater than that of the work function. The filament metal should be heated with Joule heat by transmitting a filament heating current to apply an energy corresponding to the work function to the electron. As indicated by the dotted line (temperature T_1) in the left half of Fig. 4.5, the existence probability of electrons gradually reaches high energy levels as the temperature increases. The top edge of the solid line in the left half of Fig. 4.5 (temperature T_2, where $T_2 > T_1$) exceeds the vacuum level and the electrons of an amount corresponding to the

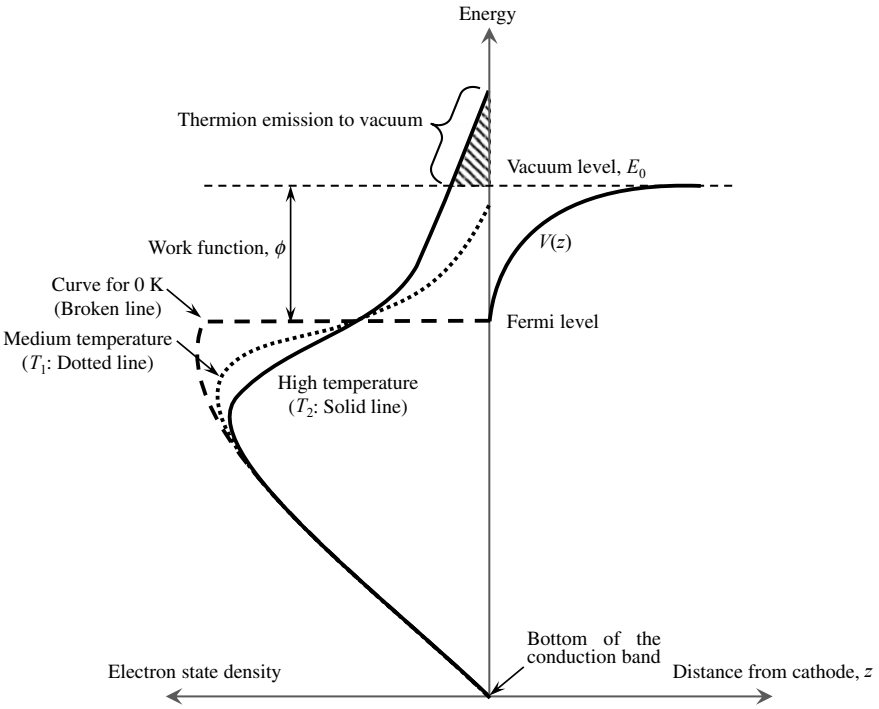

Fig. 4.5 Schematic showing an overview of thermionic emission. The right half shows the potential of the cathode surface. The left half shows the electron energy distribution at absolute zero and temperatures T_1 and T_2 ($T_1 < T_2$)

hatched area are emitted. Thermionic emission occurs all at once when the surface barrier is exceeded, so the energy distribution is biased towards the low-energy side. The potential $V(z)$ of the cathode surface shown on the right half of Fig. 4.5 is the mirror-image potential created by the electron itself on the metallic surface. This is expressed as follows, with the distance between the electron and cathode as z, and the vacuum level as E_0:

$$V(z) = E_0 - \frac{e^2}{16\pi\varepsilon_0 z} \tag{4.7}$$

Here, ε_0 is the vacuum permittivity. Also, when a relatively high electric field F is applied, an electric field potential component, which includes the slope of the electric field, is added as shown in Fig. 4.6.

$$V(z) = E_0 - \frac{e^2}{16\pi\varepsilon_0 z} - eFz \tag{4.8}$$

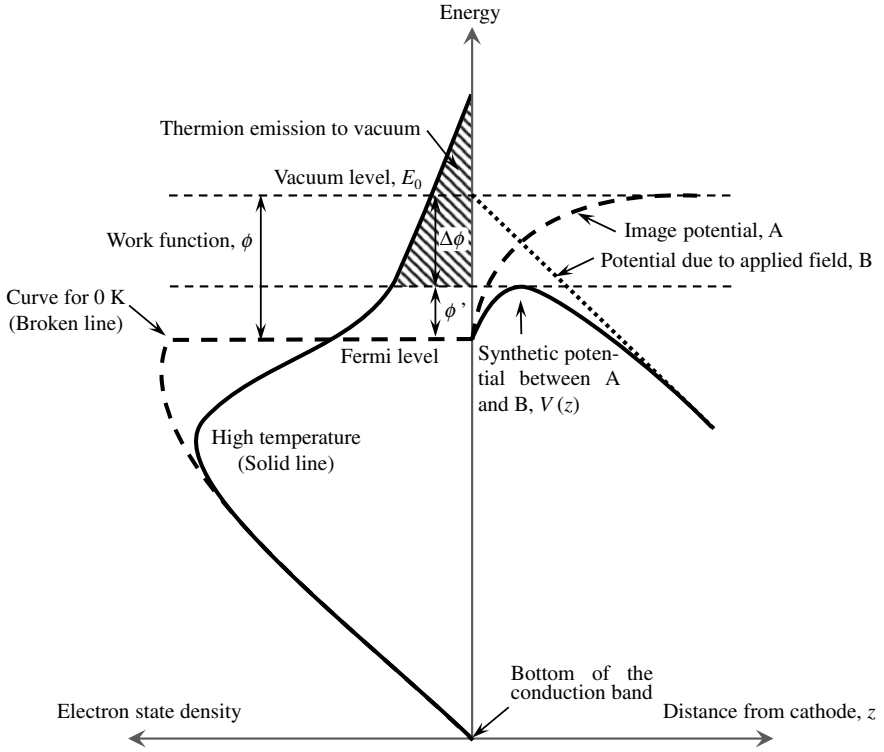

Fig. 4.6 Schematic showing an overview of thermionic emission when an electric field is applied on the cathode surface. The right half shows the potential of the cathode surface; the left half shows the electron energy distribution at high temperatures

The effective work function ϕ' in these cases is reduced by $\Delta\phi$ from its original value. This type of electric field effect is referred to as the *Shottky effect*. The decrease in the potential barrier due to the Shottky effect is at a maximum value at:

$$z = \frac{1}{4}\sqrt{\frac{e}{\pi\varepsilon_0 F}} \tag{4.9}$$

where ϕ' takes the following form:

$$\phi' = \phi - \frac{e}{2}\sqrt{\frac{eF}{\pi\varepsilon_0}} \tag{4.10}$$

So what types of materials are suited for supplying electrons when thermionic emission is utilized? If there is no electric field effect and if the amount of thermions emitted per unit surface is expressed as the electric current density J_c [A/m^2], this is

expressed as follows [10] and can be obtained by integrating the energy distribution higher than the vacuum level (inclined line portion) in Fig. 4.5:

$$J_c = \frac{4\pi mek^2}{h^3} T^2 e^{-\phi/kT} \tag{4.11}$$

Here, h is the Planck constant, k is the Boltzmann constant, m is the electron mass, and T is the absolute temperature. This equation is referred to as the *Richardson-Dushman equation*. The coefficient portion on the right-hand side of Eq. (4.11) is generally referred to as the thermionic emission constant. This coefficient is fixed regardless of the type of metal and its theoretical value is 1.20×10^6 [A/(m^2·K^2)]. The ideal thermion beam current can be determined by multiplying the cathode surface area to the electric current density in Eq. (4.11).

The electric current density of the thermion beam also increases relative to that in Eq. (4.11) when the electric field is present, as shown in the following equation:

$$J_c' = \frac{4\pi mek^2}{h^3} T^2 exp\left(\frac{-\phi - \beta F^{\frac{1}{2}}}{kT}\right) \tag{4.12}$$

$$\beta = \frac{e}{2}\sqrt{\frac{e}{\pi\varepsilon_0}} \tag{4.13}$$

Equation (4.11), which does not consider the influence of the electric field, is used to calculate the J_c values of tungsten, platinum, copper, and iron. The result is Fig. 4.7. The plot is cut off near the melting point for all metals except tungsten,

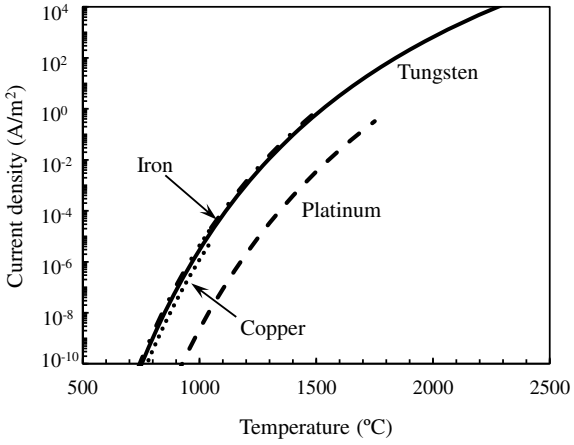

Fig. 4.7 Relationship between saturation current density of thermions, when various metals were used as an X-ray filament, and temperature. Except for tungsten (solid line), the plots of platinum (dashed line), copper (dotted line), and iron (dash-dot line) are all cut off near the melting point

which has a melting point around 900 °C higher than the upper limit of the horizontal axis. It is clear when considering heat resistance that these materials can only tolerate temperatures considerably lower than its melting point during actual use. From this figure, it is evident that tungsten, which has a high melting point and superior high-temperature strength, may not necessarily have a small ϕ but is suited as filament material. The favorable workability of the material is also one of the reasons why tungsten is used. Furthermore, other metallic materials melt before thermionic emission occurs. The working temperature of tungsten filaments is set at −2500 °C. The emission current density, in this case, is thought to be around 1000–4000 A/m^2.

A photograph of a tungsten filament from an X-ray tube is shown in Fig. 4.8. The tungsten wire is used in a coiled form. The cathode of the X-ray tube may also use *indirectly heated cathodes*, similar to those in miniature-tube-type vacuum tubes used in the past. Reported structures include a barium or strontium oxide coating on the surface of nickel cylinders, in which an insulated heating filament is placed [11]. A characteristic of oxides like oxidized barium or strontium is that their work function is significantly lower than that of the metals alone [11]. Using this enables the operation of cathodes at temperatures of 700–900 °C, which is significantly lower than that used when the tungsten filament is directly heated [11]. This also results in the longevity of the X-ray tube. Figure 4.9 shows a comparison between the thermionic emission from oxides (barium-strontium dioxide: BaO–SrO, a complex oxide of barium and strontium) and tungsten. Sufficient current density can be achieved at a temperature considerably lower than that of tungsten. Here, the work function and constant of the Richardson-Dushman equation for barium-strontium dioxide were set as 0.95 eV and 100 [A/(m^2·K^2)]. For reference, the work function of the barium used in the figure was 2.11 eV. Oxide coatings can be created by applying carbonates of barium, strontium, calcium, etc. on the substrate metal and heat treating the metal under high-temperature and high-vacuum conditions [12].

The filament is placed within a hollow referred to as a cathode cub and is set up so that the focal spot is aligned in a fixed location on the anode. An electron beam can be collimated by insulating the cathode cup from the filament and applying a negative

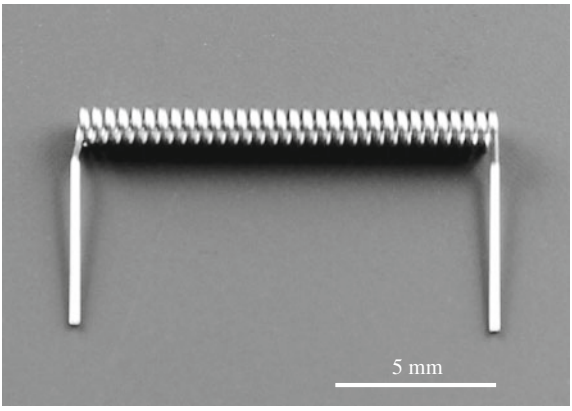

Fig. 4.8 Photograph of a cathode filament part (made from tungsten) in an X-ray tube (courtesy of Yasuaki Takeishi of Takeishi Electric, Co., Ltd.)

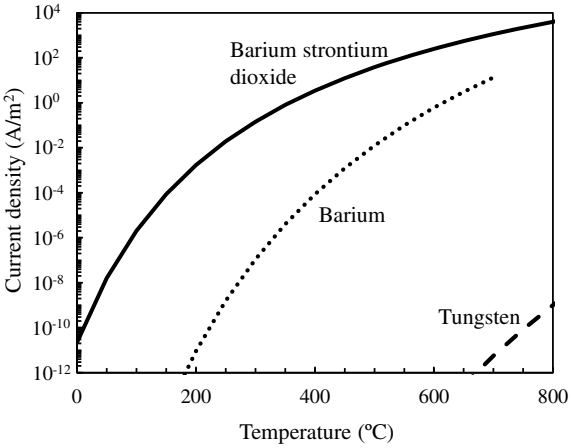

Fig. 4.9 Relationship between the saturation current density of thermions, when barium-strontium dioxide, barium, and tungsten were used as a cathode for an X-ray tube, and temperature

bias voltage. A light source that is brighter than cases where electron radiation is generated in all directions can be created using this method. For example, reports have indicated that the bias voltage application of −2000 V to the cathode cup allows for the focal spot size to be 1/4 the value of when a bias voltage is not applied [13].

As shown in Fig. 4.10a, most of the thermions generated in the filament can reach the anode when the tube voltage is high ($V_a > 40$ kV). As shown in Fig. 4.11, increasing the filament heating current and emitting more thermions results in an increased *tube current* (anode current). Meanwhile, as shown in Fig. 4.10b some of the thermions reach the anode when the tube voltage is low ($V_a < 40$ kV); the rest, however, remain as a *space charge* near the cathode. The existence of the space charge works in the direction where the emission of thermions from the cathode is suppressed. Increasing the filament heating current, in this case, does not increase the tube current as seen in Fig. 4.11 and instead saturates it. The effect of this space charge is why thermionic emission is stable and easy to control. When the space charge is predominant in this way, the following *Child-Langmuir equation* is established:

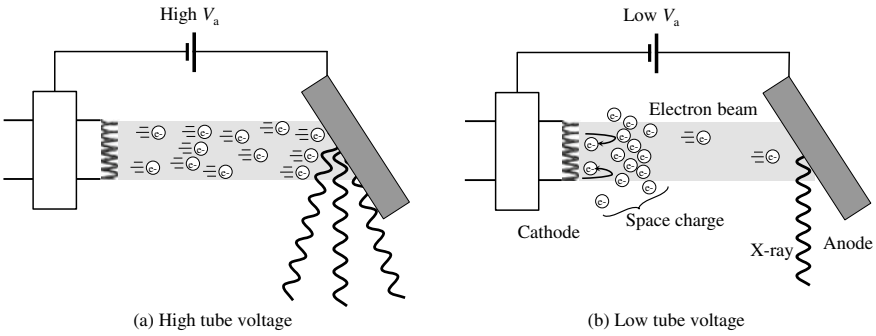

Fig. 4.10 Schematic showing the influence of space potential

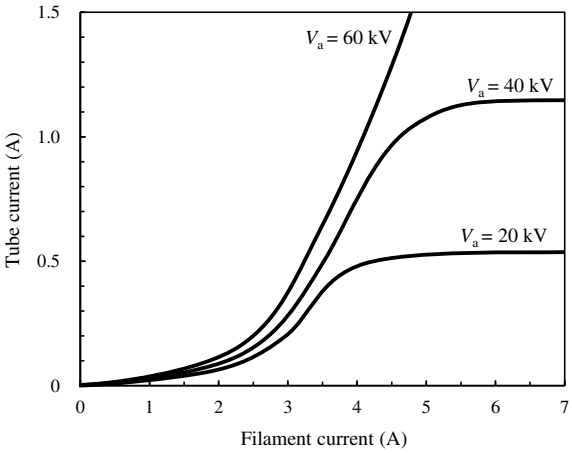

Fig. 4.11 Schematic showing the relationship between the filament heating current and tube current. Low-tube current cases where the space charge is dominant and high-tube current cases where the filament current is dominant are shown

$$J_a = K \frac{V_a^{\frac{3}{2}}}{d^2} \tag{4.14}$$

Here, K is a constant and d is the distance between the anode and cathode. Equation (4.14) indicates how the tube current increases relative to tube voltage by a power of 3/2, shown on the left-hand side of the schematic of the relationship between tube current and tube voltage in Fig. 4.12. The right-hand side of Fig. 4.12 shows that the filament heating current can be increased or decreased to regulate the filament temperature, which in turn allows for the control of the tube current. In this way, it is necessary to understand that there are cases where the tube current barely changes when the tube voltage is regulated and cases where it is acutely sensitive, depending on the focal spot size of the X-ray tube, as well as the tube current and voltage values.

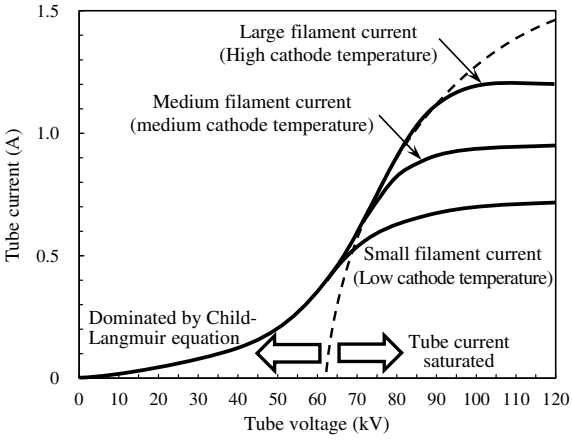

Fig. 4.12 Schematic showing the relationship between tube voltage and tube current. The figure shows three cases, ranging from where the filament current and temperature are low to cases where the filament current is high and thermionic emission is active

Incidentally, there have been reports of scanning electron microscope (SEM)-based X-ray CT scanners with the electron optics systems of an SEM that use electron beams from compounds with a ϕ value smaller than that of tungsten (e.g. LaB_6), or *field emission* guns. Recent trials by Perini et al. used targets of either bulk (i.e. several mm^2), thin-film, or nanowire tungsten in SEMs with a field emission gun, generating X-rays using a 1000 nA, 30 kV electron beam [14]. A maximum of 60 nm spatial resolution was obtained in transmission observations when using a 400-nm–2-μm length, 70-nm width nanowire as a target [14]. Although the X-ray energy, in this case, was approximately 10 keV and flux was also low, this was an extremely interesting trial that visualized the microstructures of small samples at a deep sub-micron scale.

Here, field emission refers to when electrons inside a metal are emitted when a high electric field is applied. Figure 4.13 shows a schematic of field emission. The potential barrier width becomes considerably smaller when the electric field strength significantly increases (GV/m level) compared to Fig. 4.6 and electrons are emitted through a quantum mechanical phenomenon referred to as the tunnel effect. Cathodes

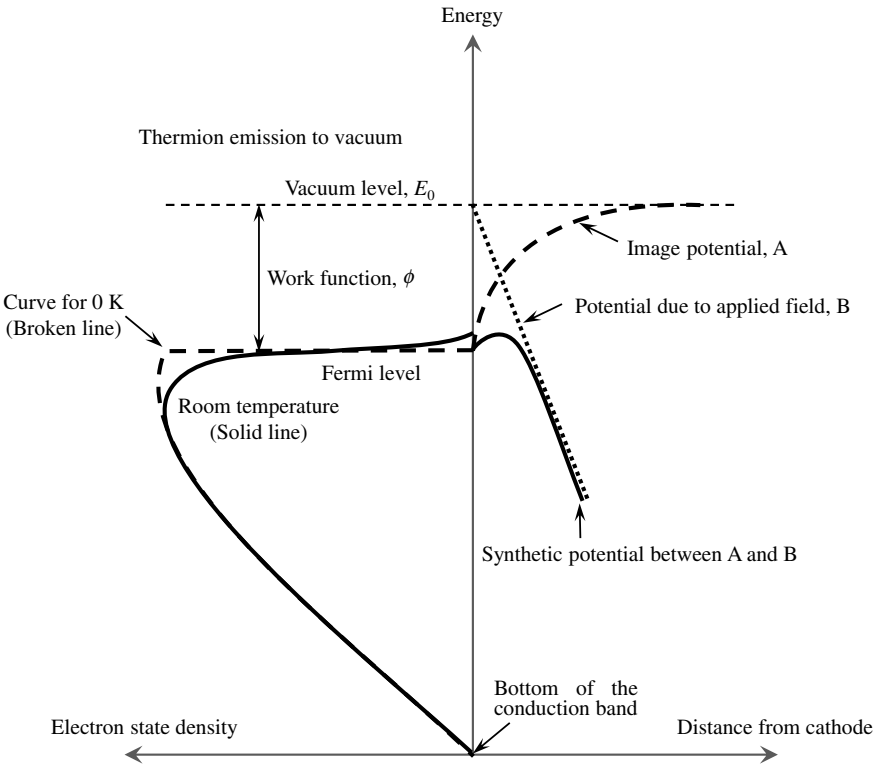

Fig. 4.13 Schematic of field emission when a large electric current is applied on the cathode surface. The right half shows the cathode surface potential; the left half shows the electron energy distribution at room temperature

do not need to be heated with field emission, so this process is also referred to as *cold emission*, in contrast to thermionic emission. This process also has the advantage of requiring less power consumption as a result. The current density for field emission cases takes the form of the Fowler-Nordheim equation, shown below:

$$J_c^F = AF^2 exp\left(\frac{-B\phi^{3/2}}{F}\right) \tag{4.15}$$

Here, A and B are constants that depend on ϕ. From the above equation, the emission current density is extremely dependent on the electric field. For this reason, even slight changes in the electric field at a level of around 1×10^9 (V/m) can rapidly change the emission current density from effectively 0 to an extremely large value.

(2) Anode

The physical phenomena of X-ray generation when the electron beam is incident to the target has been described in Sect. 4.1.1. Here, the important characteristic of X-ray tubes other than X-ray energy and intensity discussed in that section is most likely spatial resolution. Figure 4.14 shows a schematic of how focal spot size influences spatial resolution. The X-rays emitted from points A and B, which are respectively on the left- and right-hand side of the focal spot, are detected at different pixels in the detector after transmitting through the same position in the sample. This results

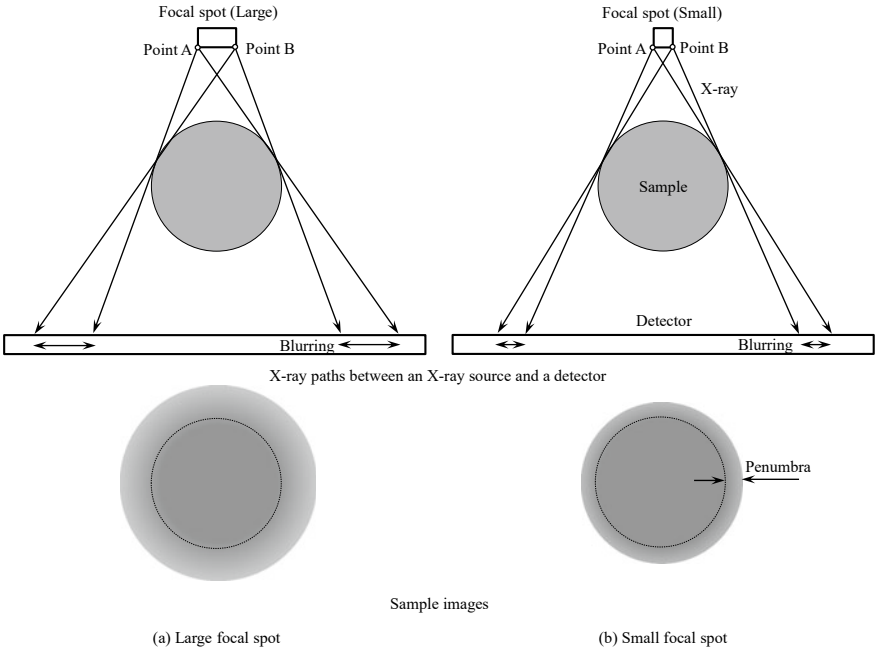

Fig. 4.14 Schematic showing the influence of focal spot size on image blur

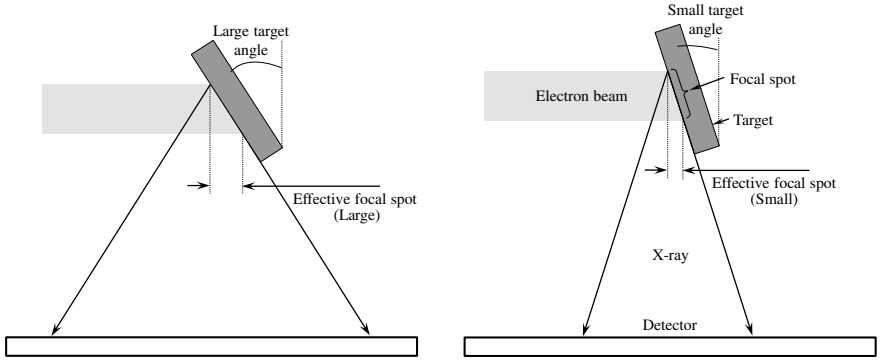

(a) Large target angle (b) Small target angle

Fig. 4.15 Schematic showing the influence of the target inclination angle; a smaller target angle results in a narrower X-ray irradiation range

in image blur. Comparisons between Fig. 4.14a, b show that this blur increases when the focal spot size increases. The lower half of Fig. 4.14 shows the *penumbra* around the visualized sample. For the same reason, X-rays generated by electrons colliding into areas other than the anode target also result in decreased spatial resolution and contrast. This can be up to 10% of the overall intensity at certain times. As seen in Figs. 4.4 and 4.15, targets in the anodes of actual X-ray tubes are inclined several to several dozen degrees from the direction facing the detector from the target. The actual focal spot takes the shape of a narrow rectangle, which corresponds to the shape of the filament. Meanwhile, the *effective focal spot* size shown in the figure is the apparent focal spot size (filament length in this figure) as seen from the direction of the detector. This is important when considering spatial resolution. When reproducing the same effective focal spot size, a smaller target angle can increase the filament length, as in Fig. 4.16. It can be observed from Table 6.1 shown later that X-ray tubes with a relatively large target angle of around 45° are used for commercially-available X-ray CT scanners.

Important elements that stipulate the effective focal spot size are the filament length, coil diameter, the electron beam convergence due to the cathode cup as in Sect. 4.1.2 (1), target inclination angle (*target angle*) in Fig. 4.15, tube voltage, and tube current. The focal spot size generally increases when the tube current increases while keeping the tube voltage fixed, or when the tube voltage is low while keeping the tube current fixed. Decreasing the effective focal spot directly results in improving the spatial resolution in cases where the spatial resolution of the X-ray CT scanner is limited by the X-ray tube. Meanwhile, as shown in Fig. 4.15, decreasing the target angle has the disadvantage of generating X-ray absorption due to the target itself from one side of the X-ray beam, and limiting the range of X-ray irradiation.

Incidentally, the intensities of X-rays generated by *bremsstrahlung* or fluorescent X-rays should ideally be homogeneous. However, actual X-ray intensities are far from this ideal. This is primarily due to a phenomenon referred to as the *heel effect* shown

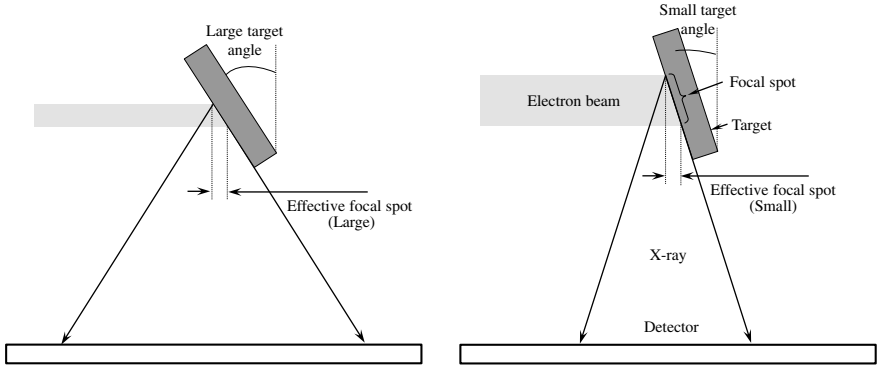

(a) Large target angle and short filament

(b) Small target angle and long filament

Fig. 4.16 Schematic showing the influence of the target inclination angle. The filament length needs to be decreased as shown in (**a**) when the target angle is large in order to maintain the same effective focal spot size

in Fig. 4.17. Up until now, we have only considered simplified cases in Figs. 4.15 and 4.16 where X-rays were generated on the target surface. However, in reality, electrons penetrate up to a depth stipulated by its kinetic energy and the target material, and X-rays are generated inside the target material. For example, Monte Carlo simulations conducted by Poludniowski et al. showed that electrons penetrate tungsten targets up

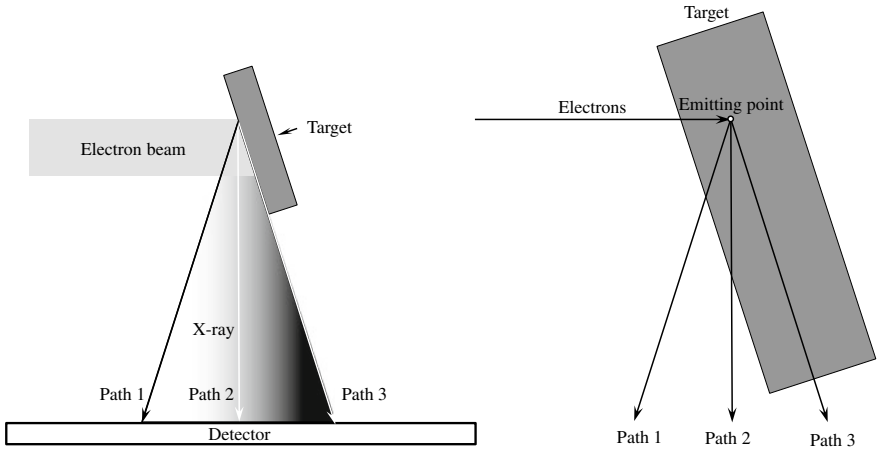

(a) Inhomogeneous X-ray intensity due to the heel effect

(b) Magnified view of the target

Fig. 4.17 Heel effect generated due to target inclination; **a** is a schematic showing X-ray intensity unevenness due to the heel effect and **b** is its magnified view, showing a schematic of X-ray paths 1, 2, and 3 in order from the cathode side, and the difference in transmission distances of the X-ray in the anode

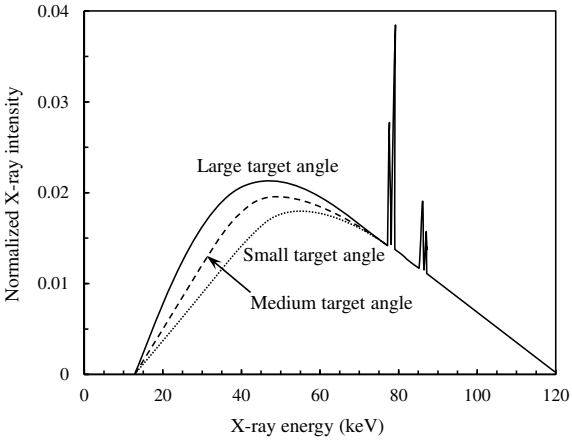

Fig. 4.18 Schematic of X-ray spectra obtained when an accelerated electron beam is incident to a metal target (solid line). The dashed lines and dotted lines are spectra for when the target angles are lower than the solid line

to a depth of around 14 μm with a tube voltage up to 150 kV [15]. For this reason, X-rays near the cathode in the generated cone beam have a relatively short distance for transmitting through the anode, while in contrast those near the anode have a longer distance. The target itself acts as a filter on the anode side, so X-rays attenuate, and their low-energy components are lost. Meanwhile, this influence is minimal on the cathode side, X-rays retain their high brilliance, and the low-energy components are not lost. Furthermore, a transition in X-ray intensity and energy distribution occurs in the intermediate position. A characteristic X-ray intensity distribution is generated in this manner. The heel effect becomes particularly strong when the target angle becomes smaller. Figure 4.18 shows a schematic of the influence of the target angle on the X-ray spectra. A smaller target angle results in the peak of the continuous X-ray on the low-energy side simultaneously becoming lower and shifting to the high-energy side. Furthermore, care must be taken as the influence of the heel effect becomes stronger with deteriorated X-ray tubes.

Next, we discuss heat production. As previously discussed, over 99% of the energy in electrons is dissipated as heat. For this reason, materials with favorable thermal conductivity are placed around the target and heat is removed through heat transmission and heat radiation, as shown in Fig. 4.4. Furthermore, coolants are further used to ensure that the target material retains a lower temperature and does not vaporize or melt. This cooling presence or extent is determined by factors such as X-ray tube output. A rotating-anode structure like that shown in Fig. 4.19 is generally used for medical CT scanners. The structure of the anode has a relatively high heat capacity, and this is rotated at a rapid speed of around several thousand to 10,000 rpm. Compared to the fixed-anode case, X-rays are generated across a wider area (typically by a factor of several dozens), and it is advantageous in that heat is not concentrated in a small area. The typically tolerable load is proportional to $\sqrt{dn_r}$, where d is the disk diameter and n_r is the number of rotations. This system has been used in medical CT scanners from the third generation (shown in Fig. 3.1b) onward. This system is used in industrial X-ray CT scanners as well for high-energy/high-output

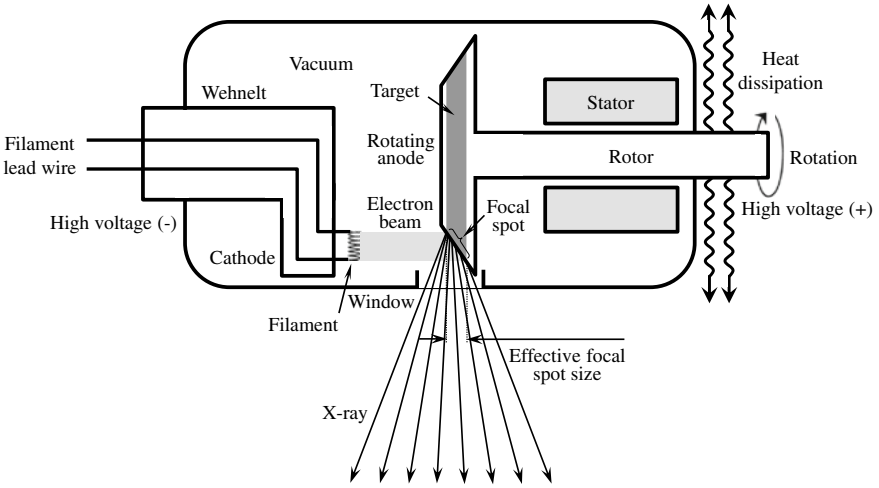

Fig. 4.19 Schematic of rotating-anode X-ray tube structure

tube cases. However, this requires bearings for the high-speed rotation of the anode in vacuum at local temperatures over 2000 °C, as well as technology for insulation from high voltages [16]. For example, gallium, which is a liquid at room temperature, has been used in liquid metal hydrodynamic bearings in order to increase cooling efficiency through liquid-metal-based conduction cooling [16]. Rotating-anode systems are ideal for medical CT scanners which conduct exposures at high output for short periods of time and which have sufficient cooldown times due to patient turnover, but have a minor role in industrial X-ray CT scanners.

Figure 4.20 shows a photograph of a tungsten target in a commercially-available X-ray tube. Fixed-anode systems like those in Fig. 4.4 typically use copper as a base and have a structure where the target is embedded in the portion where the electron hits. Rotating-anode systems like those shown in Fig. 4.19 typically have a W–10% Re alloy coated on a dispersion-hardening molybdenum alloy disk referred to as TZM (Mo–0.5Ti–0.08Zr –0.025C alloy) or MHC (Mo–1Hf –0.1C alloy). Structures whose heat capacity is assured are also used by affixing graphite, which has a high specific heat at high temperatures, to metals. Rhenium (Re) additions to tungsten increase tungsten strength and ductility at high temperatures, as well as improve its resistance to repeated thermal stress [17]. This also prevents coarsening and grain boundary embrittlement due to the recrystallization, which occurs when temperatures exceed 1500 K in pure tungsten, greatly improving its fracture toughness [18].

(3) High-Voltage Equipment

A high-voltage transformer is typically used to increase alternating current (AC) to supply tube voltages ranging from 10 to several hundred kV and tube currents ranging from 1 to several thousand mA. The high voltages obtained are applied to the X-ray tube after converting to direct current (DC) using a rectifier. Two pulses are

Fig. 4.20 Photograph of the rotating-anode portion (made from tungsten) of the X-ray tube (courtesy of Toshiba Materials, Co., Ltd.)

generated for each AC cycle when single-phase power sources are used and a voltage waveform is generated where the output peaks are continuous. Furthermore, three-phase/six-peak high-voltage X-ray devices, where a three-phase power source and six rectifiers are used to conduct full-wave rectification, produce output waveforms where six pulse peaks are superimposed per cycle. Furthermore, 3-phase/12-peak high-voltage X-ray devices, where 12 rectifiers are used, produce output waveforms that have an even smaller voltage ripple factor. Other than these, inverter-type high-voltage X-ray devices are generally widely used. In the case of the inverter-type, voltages are converted to act at high frequencies of several 100 Hz to several 10 kHz in the high-frequency inverter section, after which it is applied to the high-voltage generating section, whereupon its voltage is increased and rectified. For this reason, direct currents with even smaller ripples are output. As a result, a sufficiently smooth output can be obtained even with a single-phase power source.

(4) X-ray Tube Longevity

Most malfunctions in an X-ray tube are due to heat generation. For example, major malfunctions include melting or destruction of the anode, target material vaporization or deposition, cutting of the filament, loss of vacuum in the tube container in the sealed case, bearing malfunctions in the case of a rotating-anode type, destruction of the tube container, and decreased insulation performance of the insulating oil due to carbonization in the case of oil cooling.

For the cutting of filaments, using *thorium oxide* (ThO_2) in pure tungsten allows for a larger current density to be obtained at a lower temperature of 1900 K relative to that of pure tungsten and for longevity to be achieved [19]. For example, short-term heating of a tungsten wire with 1–2% additions of thorium oxide at temperatures

around 2800 K produces a single-atom layer of thorium and reduces its work function considerably to around 2.6. For this reason, the emitted current increases by orders of magnitude at the same temperature. There have been recent investigations on carbide substitutions that do not use thorium oxide, which is a radioactive material [20]. The thermionic emission-type cathode, which uses oxides with a low work function have already been discussed. There has also been an increasing number of reports on X-ray tubes with cooled cathode-type power sources, which use a carbon nanotube and field emission to emit electrons even at low voltages. There have been over 30 publications on this since the initial 2001 publication by Sugie et al. of the Nagoya Institute of Technology [21]. There have been reports among these of X-ray tubes where the focal spot diameter was below 1μm [22].

(5) Commercially-Available X-Ray Tubes

Specifications of commercially available X-ray tubes currently available (as of August 2017), which manufacturers have indicated are used as industrial X-ray CT scanners, are shown in Table 4.3. These are all fixed-anode X-ray tubes. The numerical specification values were directly obtained from the manufacturers' websites [23–25]. Care must be taken as the devices specified in the table have spatial resolutions of transmission images measured from test charts like the X-ray resolution chart specimens from the Japanese Inspection Instrument Manufacturers' Association [26]; their values may be considerably smaller than the focal spot dimension provided. Methods for end-users to measure the focal spot size are stipulated by ASTM, etc. (e.g. ASTM E1165-12).

Figures 4.21 and 4.22 show the external appearance of representative devices among those in Table 4.3 with large and small outputs (microfocus tube), respectively. The energy range varies widely, with a tube voltage from 5 kV to 600 kV. The tube current also ranges over four orders of magnitude, from 0.15 mA to 4900 mA. Considering the output, this can range from around 4.5 W in devices for microfocus use to a maximum of 4200 W. The focal spot size can be as small as 250 nm for microfocus tubes. However, the output, in this case, is below 10 W.

Microfocus tubes come in two forms, namely of an open and sealed type. The sealed type, which has already been considered in this book, uses a reflective target like that in Fig. 4.23a and is generally used to obtain a microfocus spot and relatively large output. An additional advantage is that it is maintenance-free. Meanwhile, the open type typically has a transmissive target as in Fig. 4.23b and has the characteristics of a focal spot size smaller than the sealed-type and a high magnification due to an even shorter focal spot to sample distance can be obtained [27]. There have also recently been products where a transmissive target is used in a sealed-type system, as shown in Table 4.3. We can see that X-ray tubes with reflective targets are primarily used in commercially-available X-ray CT scanners in Table 6.1, shown later.

In Figs. 3.32 and 3.37, we discussed projections in fan-beam or cone-beam optical systems considering a distance D between the point light source and sample center of rotation. Attention must be paid to the fact that this D does not represent the distance measured from the window in Figs. 4.4 or 4.19 but rather the location of the focal spot inside the X-ray tube. As seen in Fig. 3.32, the image magnification

Table 4.3 Representative commercially available X-ray tubes and their specifications

Manufacturer	COMET							Feinfocus	
Type	MXR-601HP/11	MXR-451HP/11	MXR-320HP/11	MXR-225HP/11	MXR-160HP/11	MXR-100HP/20	MXR-75HP/20	FXE (Transmission)	FXE (Scanning)
Output (W)	700/1500	700/1500	800/1800	800/1800	800/1800	1000	1000	−10	−40
Tube voltage (kV)	600	450	320	225	160	100	75	−225	−225
Tube current (mA)	3700/4100	4100/4200	4100/4200	4100	4100	3700	3700	0.001–1	0.001–1
Focal spot size (μm)	700/2000	400/1000	400/1000	400/1000	400/1000	1000	1000	0.3–	−10
Target	W	W	W	W	W	W	W	W	W
Target angle (°)	11	11	11	11	11	20	20	–	–
Irradiation angle (°)	40×30	40×30	40×30	40×30	40×30	40	40	170	150
Coolant	Oil	Oil	Oil	Water	Water	Water	Water	–	–
Weight (kg)	145	95	40	11	8	2.1	2.1	–	–

(continued)

Table 4.3 (continued)

Matsusada Precision															
XTR-Be	XTFR	XF80-80	XRC50-50	XPR600-30	XPR1200-30	XPR600-60	XPR1200-60	XPR600-100	XPR1000-100	XPR640-160	XM6	XM10	XF40-130	XF8-90	XF18-90
−100	−60	−80	50	600	1200	600	1200	600	1000	640	6	10	−40	−8	−18
5–50	6–60	20–80	5–50	20–30	20–30	20–60	20–60	20–100	20–100	20–160	10–40	10–60	40–130	30–90	30–90
2	1	2	1	20	40	10	20	6	10	4	0.03–0.15	0.033–0.166	0–0.3	0–0.088	0–0.2
500[a]	100[a]	15–25[a]	70[a]	3000[a]	3000[a]	3000[a]	3000[a]	3000[a]	3000[a]	3000[a]	50–1000[a]	50–1000[a]	4[a]	3[a]	4[a]
W	W	W	W	W	W	W	W	W	W	W	W	W	W	W	W
–	20	–	–	–	–	–	–	–	–	–	19	19	–	–	–
50	20	33	25	40	40	40	40	40	40	40	28	20	30	30	30
Oil	Oil	Air	Oil	Water	Water	Water	Water	Water	Water	Water	Air	Air	Air	Air	Air
6	6	3.2	3	3.5	3.5	3.5	3.5	3.5	3.5	3.5	5	5	6	6	6

(continued)

Table 4.3 (continued)

Hamamatsu Photonics											X-ray WorX				
L9421-02	L10101	L10321	L9631	L9181-02	L9181-05	L12161-07	L12531	L11091	L10711-03	L10801	XWT-160CT	XWT-190CT	XWT-225CT	XWT-240CT	XWT-300CT
8	20	20	50	39	39	75	16	8	8	200	350	350	350	350	350
20–90	40–100	40–100	40–110	40–130	40–130	40–150	40–110	20–160	20–160	20–230	20–160	20–190	20–225	20–240	50–300
10–200	10–200	10–200	10–800	10–300	10–300	10–500	10–200	5–200	5–200	10–1000	50–3000	50–3000	50–3000	50–3000	50–2000
5–	5–	5–	15–	5–	15–	5–	2–[a]	1–[a]	0.25–[a]	4–[a]	2000	2000	2000	2000	3000
W	W	W	W	W	W	W	W	W	W	W	W	W	W	W	W
–	–	–	–	–		–	–	–	–	–	–	–	–	–	–
39	42	118	62	45	100	43	120	120	140	40	30	30	30	30	30
空気	Air	Air	Air	Air	Air	Air	Air	Air	Water	Water	Water	Water	Water	Water	Water
10	10	10	12	11	11	20	19	62	72	98	36	36	50	50	69

[a]Spatial resolution of a projection image measured using a resolution evaluation chart

Fig. 4.21 Example of a commercially-available X-ray tube, COMET MXR-601HP in Table 4.3 (courtesy of Mr. Matsuda from Comcraft, Co.)

(a) (b)

Fig. 4.22 Example of a commercially-available microfocus X-ray tube from Table 4.3; **a** Hamamatsu Photonics L10711-03 (courtesy of Hamamatsu Photonics) and **b** Matsusada Precision XF40-130 (courtesy of Toyotoshi Ueyanagi from Matsusada Precision, Inc.)

M is expressed with the following equation when the distance D_0 from the point light source to the detector is considered. Making D smaller is important when it is necessary to conduct projections with a larger magnification and obtaining superior spatial resolution.

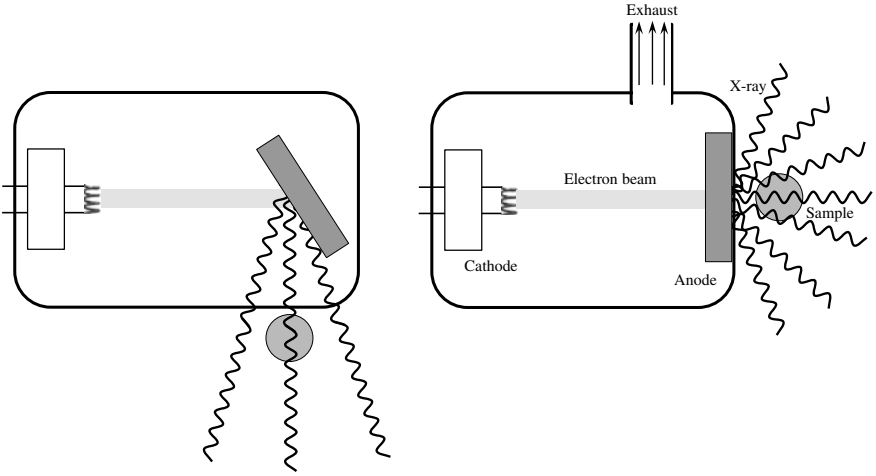

Fig. 4.23 Schematic of two microfocus tube systems

$$M = \frac{D + D_0}{D} \tag{4.16}$$

Incidentally, the minimum distance between the sample and focal spot is stipulated by the distance between the window and focal spot. Open-type microfocus X-ray tubes shown in Fig. 4.24 that use a transmissive target, described in Table 4.3, have a minimum distance of around 0.5 mm, whereas sealed-type X-ray tubes, which use a reflective target, have a relatively increased distance of between 7 to several dozen of mm. When pursuing the smallest focal spot size in open-type X-ray tubes, the electron beam should be narrowed using either a one or two-step (i.e. combination of

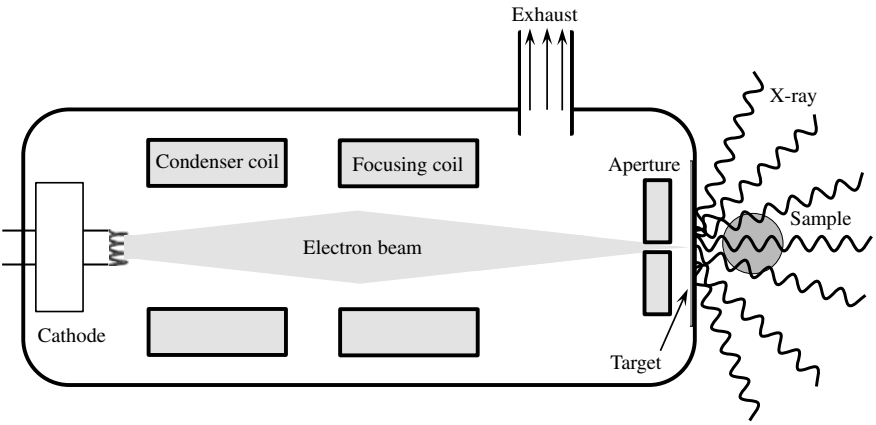

Fig. 4.24 Schematic of a microfocus tube with an extremely small effective focal spot

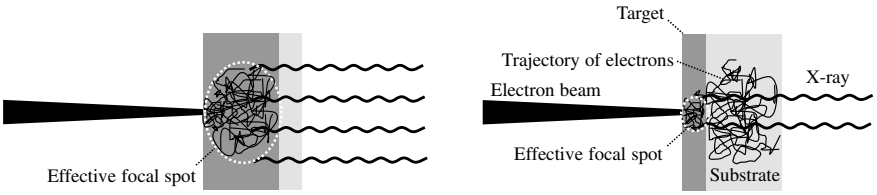

(a) Thick target (b) Thin target

Fig. 4.25 Schematic of X-ray emission behavior from a transmissive target

condenser coil and *focusing coil*) electron beam optics system and *objective aperture*; this should be directed to the thin film of the target. A thin tungsten film coated on a substrate composed of light elements like beryllium is to be used as the target. The fact that electrons enter the interior of the target from its surface has already been discussed. As shown schematically in Fig. 4.25, the electrons spread wider due to scattering in the target and X-rays are generated from an area larger than the electron beam diameter. This is the effective focal spot size in this case. A higher tube voltage increases the scattering volume and the effective focal spot size also increases. The effective focal spot size can be reduced when a thin target is used, as in Fig. 4.25b. In contrast, a thicker target increases the intensity of X-rays generated in the target. However, the generated X-rays in transmissive targets do not come out if they do not transmit through the target interior. For this reason, thicker targets result in increased absorption by the target itself. Simulations conducted by Nasseri indicated that the maximum X-ray intensity, which considered absorption by the tungsten target itself, can be obtained when the following thickness t_{opt} (μm) is obtained [28]:

$$t_{opt} = -1.45 + 0.075E \tag{4.17}$$

Here, E (keV) is the X-ray energy; for example, the maximum transmissive target thickness value for a 30 keV X-ray is approximately 1 μm.

The *brilliance* of X-ray tubes can generally be compared by dividing the maximum output by the focal spot size (surface area). However, decreased effective focal spot sizes in microfocus X-ray tubes result in smaller X-ray outputs as well. Figure 4.26 shows the relationship between the focal spot size and maximum output of all X-ray tubes shown in Table 4.3. Although there is some variation at the smaller focal spot sizes, strong correlations are observed across four orders of magnitude for the focal spot size, and three orders of magnitude for the maximum output.

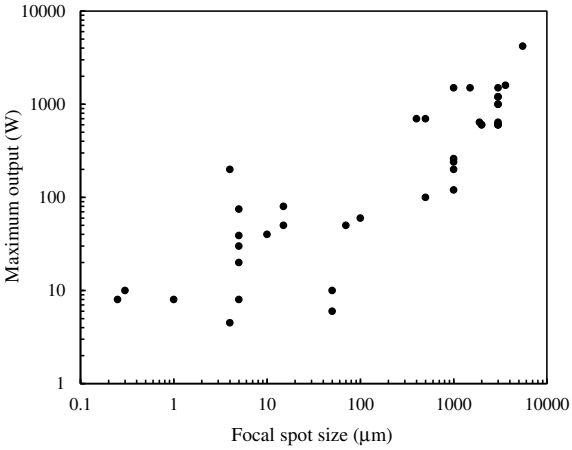

Fig. 4.26 Relationship between focal spot size and maximum output of commercially-available X-ray tubes; all products in Table 4.3 are plotted here

4.1.3 Compact Electron Accelerators

Figure 4.27 shows the thickness of iron and aluminum samples for 10% X-ray transmission calculated across a wide range of X-ray energies. In terms of image quality, this can be thought of as the maximum sample thickness under which the transmitted image can be somewhat obtained. As shown in Table 4.3, the tube voltage range of commercially-available X-ray tubes is around 5–600 kV. The maximum X-ray energies obtained in these X-ray tubes are approximately 5–600 keV and the average X-ray energies obtained from *bremsstrahlung* are thought to be about 1/2–1/3 of these values. The samples that can be imaged at the maximum X-ray energies of 200–300 keV, obtained with commercially-available X-ray tubes, are at thicknesses of at most 20–30 mm for solid iron and 70–80 mm for solid aluminum, according

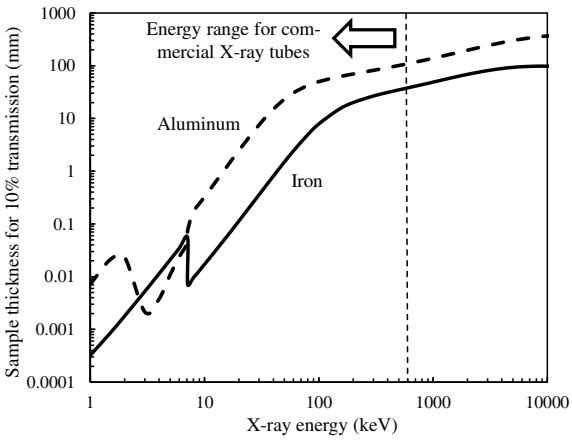

Fig. 4.27 Relationship between X-ray energy when 10% of the incident X-ray transmits through iron (solid line) and aluminum (dashed line) samples and sample thickness

to Fig. 4.27. Even higher-energy X-rays would need to be generated if imaging of thicker materials were to be conducted in the laboratory.

Van de Graaff generators, invented in 1920, and *betatrons*, invented in 1942, were used in the past to generate higher-energy X-rays. Today, we use *compact electron accelerators* and *radioisotopes* (RIs) [29]. Generally, X-ray energies at the 1-MeV level or higher are required, and RIs are used when flux is not a problem; these compact and low-cost characteristics are then effectively utilized. Meanwhile, electron accelerators are used when both X-ray energies at the 1-MeV level or higher and a sufficient flux are needed. Electron accelerators are a large-scale setup and their costs for introduction far exceed those of X-ray tubes or RIs. However, using these would enable the imaging of thicker and higher-density materials (e.g. iron with a thickness of several dozen cm); this also allows for imaging that is faster than with RI for materials with the same thickness. Electron accelerators have an additional characteristic in which there are no handling difficulties like those associated with RIs (i.e. the X-ray stops immediately when the power source is cut off). Electron accelerators first saw production in the 1950s primarily for military use [29]. Today, they are used not only for imaging of military products but for various civilian products as well. They are also used as electron injectors into synchrotrons.

Linear accelerators are referred to as *lineac* or *linac*. The former is more commonly used in Japanese, whereas the latter is more commonly used in English. As shown in Fig. 4.28, the electron linac comprises an *electron gun*, *buncher*, and *accelerating waveguide*. Figure 4.28 shows a schematic of a traveling-wave-type accelerating waveguide with a simple structure, primarily used for large-scale devices. Traveling-wave-type accelerating waveguides have disks with holes opened in them set up at equal intervals. The basic structure of the accelerating waveguide is the same for high-energy cases as well (e.g. for synchrotron injection use).

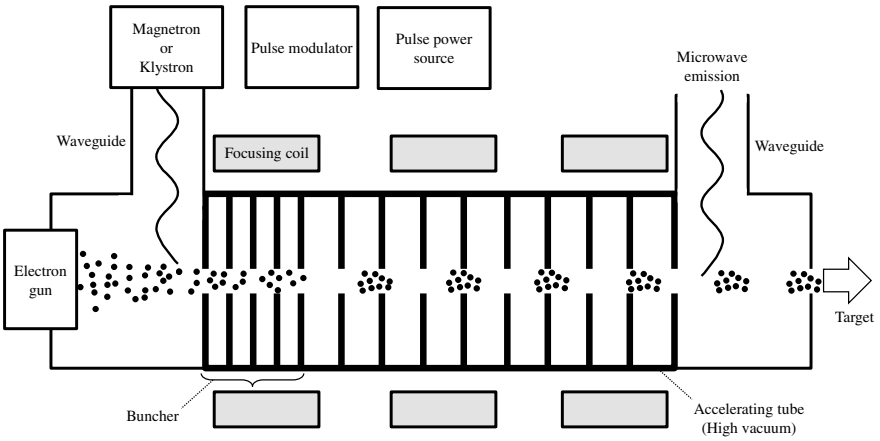

Fig. 4.28 Schematic of a compact electron accelerator with a progressive wave-type accelerating tube

First, the electrons generated with an electron gun are brought together in what is referred to as a bunch by the buncher. In a linear accelerator, an electron beam where the electrons are bunched together is obtained in the traveling direction of the electron, as well as the direction perpendicular to it. Generally, the pulse width is several μs and pulse repetition frequency is 50–500 Hz [29]. For this reason, the duty cycle (percentage of time where the pulse is on) is in the order of 0.1–0.01%.

Microwaves with a frequency of approximately 3 GHz (so-called S-band) to 9 GHz (so-called X-band) produced by a *magnetron* or *klystron* are guided through the accelerating waveguide and an electric field is generated in this cavity. The klystron is larger in scale relative to the magnetron and is more expensive, but its frequency and power control is more accurate and can be used with high-output accelerators [29]. When the microwave speed is set as equivalent to the electron speed, the electron advances under a constant drift potential within the accelerating waveguide, thereby accelerating it. Meanwhile, standing wave-type accelerating waveguides have the advantage of high acceleration efficiency per unit length, accelerating electrons over a shorter length than with progressive-wave-type accelerating waveguides. The subsequent mechanism in which the electron coming out of the accelerator collides with the target and generates X-rays is the same as that with X-ray tubes. Given the magnitude of heat inputs, the target is oftentimes water-cooled. The penetration depth of the electron into the target is approximately several hundred μm when the energy is 1 MeV and approximately several mm when the energy is 10 MeV [30]. For this reason, the target thickness would need to be 2 mm if, for example, a 9 MeV accelerator is used [30]. The range of obtained X-ray energies is around 1–15 MeV; of these, the 3–9-MeV level is widely used [29]. The focal spot size is typically approximately 2 mm and it is possible to have this below 1 mm as well [29].

A point of caution is that *neutrons*, protons, and π-mesons are also generated when the photonuclear reactions mentioned in Sect. 2.1.2 occur at the target and when X-ray energies over 6–7 MeV are used [29]. Appropriate shielding, which absorbs neutrons, should be set up in these cases. Detectors capable of handling high-energy X-rays (discussed later) should also be used.

4.1.4 Radioactive Isotopes

The half-life of commonly-used radioactive isotopes and the gamma-ray energies produced are summarized in Table 4.4 [31]. Gamma rays are the electromagnetic waves emitted by unstable nuclei when undergoing radioactive decay, which is similar to the X-rays discussed previously. Atoms in a metastable state in Table 4.4 are indicated with a superscript of "m" (for "metastable") after the atomic mass number. Atoms from Table 4.4, which are frequently used in imaging, include the following, in ascending order of gamma-ray energy: ^{241}Am (energy of 59.5 keV), ^{75}Se (270 keV), ^{192}Ir (310.5, 469.1 keV), ^{137}Cs (662 keV), and ^{60}Co (1173, 1332 keV). A characteristic of RIs is that they can be used to obtain either monochromatic or bichromatic gamma rays (gamma rays where energies are concentrated at two

Table 4.4 Half-life and gamma-ray energy of various radioactive isotopes [31]

Radioactive isotope	Half-life (s)	γ ray energy (MeV)
^{3}H	3.9×10^{8}	–
^{7}Be	4.6×10^{6}	0.48
^{10}Be	4.7×10^{13}	–
^{14}C	1.8×10^{11}	–
^{22}Na	8.2×10^{7}	1.28
^{24}Na	5.4×10^{4}	1.37
^{26}A1	2.3×10^{13}	1.84
^{32}Si	5.4×10^{9}	–
^{32}P	1.2×10^{6}	–
^{37}Ar	3.0×10^{6}	–
^{40}K	4.0×10^{16}	1.46
^{51}Cr	2.4×10^{6}	0.325
^{54}Mn	2.7×10^{7}	0.84
^{55}Fe	8.6×10^{7}	0.006
^{57}Co	2.4×10^{7}	0.122
^{60}Co	1.7×10^{8}	1.17 & 1.33
^{66} Ga	3.4×10^{4}	1.04
^{68}Ga	4.1×10^{3}	1.07
^{85}Kr	3.4×10^{8}	0.52
^{89}Sr	4.4×10^{6}	–
^{90}Sr	9.1×10^{5}	–
^{90}Y	2.3×10^{5}	–
^{99}mTc	2.2×10^{4}	0.14
^{106}Ru	3.2×10^{7}	–
^{106}Rh	3.0×10^{1}	0.51
^{112}Ag	1.1×10^{4}	0.62
^{109}Cd	4.0×10^{7}	–
^{109m}Ag	4.0×10^{1}	0.088
^{113}Sn	9.9×10^{6}	0.392
^{132}Te	2.8×10^{5}	0.23
^{125}1	5.2×10^{6}	0.035
^{129}I	5.0×10^{14}	0.038
^{131}I	7.0×10^{5}	0.36
^{133}Xe	4.5×10^{5}	0.08
^{134}Cs	6.5×10^{7}	0.61
^{137}Cs	9.5×10^{8}	0.66
^{137m}Ba	1.6×10^{2}	0.66

(continued)

Table 4.4 (continued)

Radioactive isotope	Half-life (s)	γ ray energy (MeV)
^{133}Ba	3.3×10^{8}	0.36
^{140}La	1.4×10^{5} s	1.60
^{144}Ce	$2.5 \times$ l0^{7}	0.13
^{144}Pr	l.l $\times 10^{3}$	0.69
^{144}Nd	7.3×10^{22}	–
^{152}Eu	4.3×10^{8}	0.122
^{192}Ir	6.4×10^{6}	0.32
^{198}Au	2.3×10^{5}	0.41
^{204}Tl	1.2×10^{8}	–
^{207}Bi	1.0×10^{9}	0.57
^{222}Rn	3.3×10^{5}	0.51
^{218}Po	1.9×10^{2}	–
^{214}Pb	1.6×10^{3}	0.35
^{214}Bi	1.2×10^{3}	0.61
^{226}Ra	5.0×10^{10}	0.19
^{228}Th	6.0×10^{7}	0.24
^{234}U	7.9×10^{12}	0.05
^{235}U	2.2×10^{16}	0.19
^{238}U	1.4×10^{17}	0.05
^{239}Pu	7.6×10^{11}	0.05
^{240}Pu	7.6×10^{11}	0.05
^{241}Am	1.4×10^{10}	0.06
^{252}Cf	8.2×10^{7}	0.04
^{252}Fm	9.0×10^{4}	0.096
^{268}Mt	7.0×10^{-2}	–

energy levels). The usage of monochromatic light does not result in beam hardening issues (discussed later), which occurs when using an X-ray tube or compact electron accelerator. For example, the low gamma-ray energy ^{241}Am is used for imaging of wooden materials [32]. Meanwhile, ^{137}Cs or ^{60}Co is used for large-scale containers made of iron [33, 34]. Reference [33] reports imaging of aluminum structures within a plexiglass container with a diameter of 440 mm using a 3.7 GBq (giga-becquerel, 10^{9} becquerels; which are the quantity of radioactive decay of a radioactive isotope element for a unit period of time) ^{137}Cs. Reference [34] reports the imaging of a stainless-steel disk with a diameter of 60 mm using a 74 GBq ^{137}Cs. The obtained flux in each case is in the order of 1/100 compared to using X-ray tubes [35]. This results in long imaging times, as well as lower image quality.

RI-based imaging can also quantitatively determine local density or average atomic number from images utilizing gamma rays with two different energy levels

from bichromatic sources, such as ^{192}Ir [36]. As seen in Sect. 2.1.2 (1) and (2), the extent of photoelectric absorption decreases with increased X-ray energy, whereas Compton scattering becomes more active with increased X-ray energy, up to a level of several MeV. Furthermore, photoelectric absorption has a large atomic number dependency, whereas Compton scattering does not depend on the atomic number. These trends can also be re-confirmed in Figs. 2.10, 2.11, 2.12 and 2.13. In this manner, quantitative assessments can be conducted with bichromatic gamma rays as two absorption/scattering processes with completely different energy and atomic number dependencies compete with one another.

4.1.5 Synchrotron Radiation

Synchrotron radiation refers to electromagnetic waves generated in the tangential direction of the synchrotron when the advancing direction of the electrons orbiting the synchrotron is changed using magnets. The advancing and accelerating directions of the electron are parallel in the case of *bremsstrahlung*, whereas both intersect in the case of synchrotron radiation. Synchrotron radiation has the advantages of a small radiation source size, high X-ray beam interference due to a long beamline, and high brilliance; additionally, its monochromatic capabilities indicate that the X-ray energy can be changed relatively freely. Furthermore, it has the characteristics of polarizability and pulsed light. A higher resolution, superior image quality, and S/N ratio can be obtained using these characteristics. In that sense, it would not be an exaggeration to say that synchrotron radiation X-ray tomography is the flagship of X-ray tomography technology.

The generation of synchrotron radiation was first experimentally confirmed by Langmuir et al. in 1947. The electron energy of the synchrotron at this time was 70 MeV. Afterward, first-generation radiation facilities, where accelerators subsequently created for high-energy physics research were diverted to conduct applied radiation research; second-generation radiation facilities from the 1970s onwards such as SOR-RING (1975) and the Photon Factory (1982), which used radiation generated from bending magnets; and third-generation radiation facilities like SPring-8, APS (1996, U.S.), and ESRF (1994, 19 countries of the EU), which used undulators and wigglers to generate high-brilliance radiation, were developed and used in order. Figure 4.29 shows synchrotron radiation obtained from SPring-8 compared with X-ray tubes [37]. X-ray brilliance is expressed in units of [photons/s/mm^2/mrad^2/0.1% bandwidth]; where rotating-anode X-ray tubes are approximately 10^9 in this unit, this is about 10^{12} in first-generation radiation facilities, 10^{14} in second-generation facilities, and up to 10^{19}–10^{20} in standard undulator light sources in SPring-8. It is evident that radiation facility performance has improved rapidly at each order of magnitude. Incidentally, fourth-generation radiation refers not to X-ray free-electron lasers (XFEL) based on linac principles, but radiation sources with lower emittance than third-generation radiation (e.g. MAX-IV, Sweden).

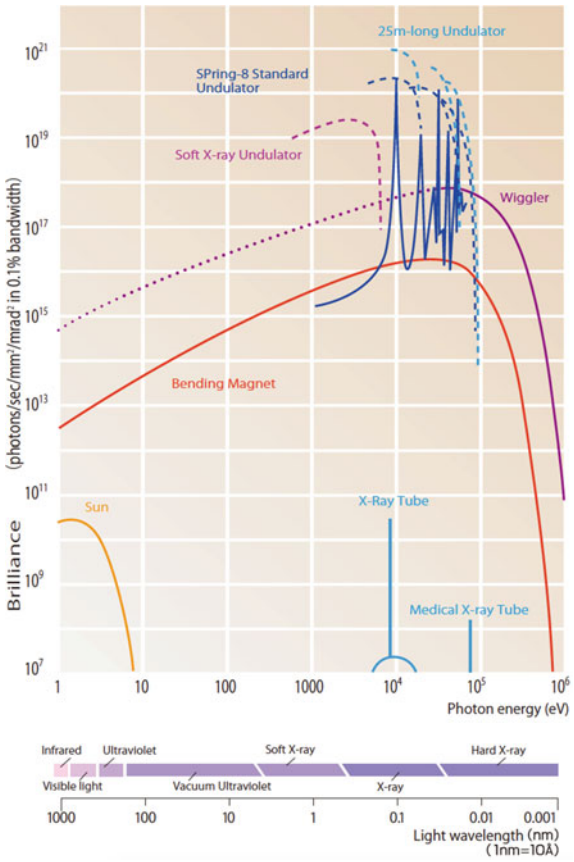

Fig. 4.29 Brilliance of radiation at SPring-8 (provided by Riken) [37]

Focusing on the wavelength in Fig. 4.29, it can be observed that synchrotron radiation covers a wide range from infrared to visible light to hard X-rays. Furthermore, synchrotron radiation is a row of pulsed light, where bunches lasting for 20–500 ps are repeated at 2 ns–1 μs -interval frequencies; for example, the length of a bunch with a width 100 ps is 3 cm.

Incidentally, the synchrotron itself cannot accelerate low-energy electrons. For this reason, electrons must be accelerated to an energy of at least several dozens of MeV before being injected into the synchrotron; in other words, the general structure of the synchrotron comprises sections that accelerate the electron beforehand (e.g. a linac) and *storage rings*, as shown schematically in Fig. 4.30. The University of Hyogo NewSUBARU adjacent to SPring-8 primarily uses electrons in the extreme ultraviolet ray to soft X-ray region, so they are directly injected from the linac to the storage ring as shown in Fig. 4.30a. Meanwhile, SPring-8 injects at the GeV energy level and combines the same electron linac as with NewSUBARU with an

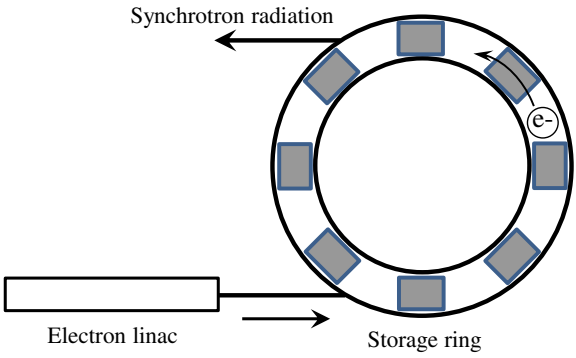

(a) Direct incident to a storage ring

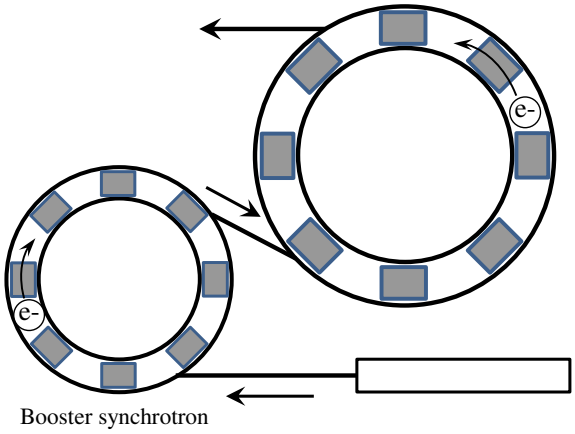

(b) Booster synchrotron as an electron accelerator

Fig. 4.30 Schematic of a synchrotron structure

electron synchrotron, as shown in Fig. 4.30b. Some microtrons combine a high-frequency electric field for accelerating electrons and a DC magnetic field for creating a circular trajectory but these are omitted here as they are not widely used in Japan. The structures in Fig. 4.30 are discussed in order below.

(1) Electron Linac

The basic principles of an electron linac in a synchrotron radiation facility are the same as those of a compact electron accelerator introduced in Sect. 4.1.3; what varies is their size and energy. Here, we primarily take SPring-8 as an example and provide an overview with a focus on its specifications.

Table 4.5 shows an overview of the electron linacs and electron synchrotrons in the major synchrotron radiation facilities in Japan [37–40]. Furthermore, Fig. 4.31 shows a photograph of the external appearance of a SPring-8 electron linac [37]. The SPring-8 electron linac is 140 m in length and accelerates an electron beam

Table 4.5 Electron accelerators of representative synchrotron radiation facilities used for X-ray microtomography [37–40]

	Type	Linac + booster synchrotron		Linac	
	Facility	SPring-8	Aichi Synchrotron Radiation Center	Photon Factory (KEKB)	Kyushu Synchrotron Light Research Center
	Location	Sayo town, Hyogo, Japan	Seto city, Aichi, Japan	Tsukuba city, Ibaraki, Japan	Tosu city, Saga, Japan
Electron linac	Energy (GeV)	1	0.05	2.5	0.26
	Type	Travelling wave accelerator	Travelling wave accelerator	Travelling wave accelerator	Travelling wave accelerator
	Number of accelerating tubes	25	2	240	6
	Peak current (mA)	2000 (Single bunch mode) 350 (Multi bunch mode)	100	50	–
	Pulse width (ns)	2 (Single bunch mode) 40 (Multi bunch mode)	1	3	200
	Repetition rate (Hz)	60	1	25	1
	High frequency acceleration frequency (MHz)	2856	2856	2856	2856
	Length (m)	140	10	400	30
Booster synchrotron	Energy (GeV)	8	1.2	–	–
	Emittance (nmrad)	230	200	–	–
	Beam current (mA)	10	5	–	–
	Repetition rate (Hz)	1	1	–	–
	High frequency acceleration frequency (MHz)	508.6	499.654	–	–
	Perimeter (m)	396	48	–	–

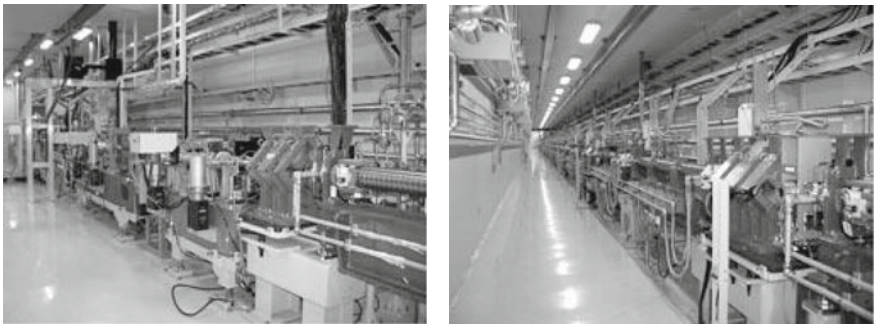

(a) First stage of the linac (b) Whole linac

Fig. 4.31 Photograph of the electron linac in SPring-8 (provided by Riken) [37]

emitted from an electron gun operating with a voltage of approximately 180 kV up to 1.0 GeV [37]. The electron gun used is the thermionic type introduced in Sect. 4.1.3, it uses porous tungsten with impregnated barium as a filament material [37]. High-temperature activation following barium impregnation can reduce its work function to approximately 1.6 eV due to the presence of free barium; owing to this, electrons can be emitted at a relatively low temperature. The process of forming bunches of the electron beam using the buncher is the same as in Fig. 4.28. As in Sect. 4.1.3, a high-frequency electric field was used to accelerate the electron beam. The accelerating waveguide portion of the SPring-8 electron linac is composed of 25 individual accelerating waveguides, each measuring 3 m in length, all joined [37]. A single accelerating waveguide is composed of 81 accelerating cavities [41] and the electron acceleration from a single accelerating waveguide is approximately 40 MeV [41]. High-frequency power is applied from a klystron every two accelerating waveguides [41]. The high-energy (1.0 GeV) electron beam obtained from this process undergoes energy width reduction in the *energy compression system* section, after which it is supplied directly to the electron storage ring of the adjacent University of Hyogo NewSUBARU through the beam transfer system. For SPring-8, it is first injected into the booster synchrotron. The energy compression system is set up at the end of the linac and is comprised of a chicane electromagnet section, where the bunch length is extended according to the energy distribution of the electron beam and an accelerating waveguide section, where energy modulation is applied to compress the energy spread [42]. Energy stability also improves due to the energy compression system and improvements in large current injection and energy stability (rms of less than 0.01% for small current) are achieved [42].

Incidentally, for electron beam obtained at the synchrotron radiation facility, high electric current, high energy, and high quality are required. *Emittance* is the primary factor that stipulates these qualities. A major objective at the currently-planned SPring-II is also reducing the emittance of the storage ring (approximately 2.4 nm rad at present to approximately 150 pm rad). The emittance, which is used to show beam performance at the accelerator, primarily expresses the volume occupied by particles

in the phase space. When considering an electron beam, the horizontal direction of emittance relative to the advancing direction of the beam is often expressed. Beams with low emittance are essentially parallel beams with a small size and whose directions are aligned. Here, the emittance of the electron beam emitted from the electron gun (thermal emittance) ε_{th} is as shown below:

$$\varepsilon_{th} = \sigma\sqrt{\frac{kT}{mc^2}} \tag{4.18}$$

Here, σ is the cathode spot size and c is the speed of light. The emission current from the cathode is determined from the work function and temperature, but the emittance is not dependent on the work function; moreover, if the temperature is equivalent, it is only dependent on the cathode spot size. As such, it is important to make the cathode radius as small as possible. Incidentally, as can be seen in Eq. (4.18), emittance usually has the dimensions of length. However, it can also be related to the beam inclination and expressed in units of mm·rad or multiplied by π and expressed in π mm·rad. Hence, care must be taken for its definition.

The emittance of electron beams in synchrotron radiation facilities can vary widely by the performance of the upstream electron gun. However, emittance worsens even during acceleration in a linac. This is because the electron is influenced by the electromagnetic field generated by itself.

(2) Electron Synchrotron

The electron synchrotron mentioned here is the so-called booster synchrotron, which is used to increase the energy of the electron beam injected into the storage ring. This enables top-up operations, where the electron is not accelerated in the storage ring. Synchrotron radiation with a fixed intensity can be constantly generated and makes large contributions to X-ray imaging. Circular accelerators that change the magnetic field with increases in acceleration energy and where the electron orbits a fixed trajectory are referred to as synchrotrons. *Bending magnets* are arranged in a circle, electrons are moved in a pseudo-circular manner, and they are accelerated up to high energy through high-frequency cavities (Fig. 4.32 [43]) placed in the electron trajectory. In the case of synchrotrons, the magnetic field is strengthened with increased energy and the electron is extracted once it reaches a given energy level. Much content overlaps with the "(3) Storage Ring" (discussed later). When compared to a storage ring, the electron synchrotron has a relatively small number of *quadrupole electromagnets* and *six-pole electromagnets* relative to bending magnets. This is due to the different usage applications of the synchrotron, such as not needing to store the electron beam [41]. Furthermore, this typically has a structure referred to as FODO, where bending magnets and quadrupole magnets are arranged in alternate order.

In the case of SPring-8, an electron beam accelerated up to 1 GeV with an electron linac is injected into the electron synchrotron at an angle of 15° using an on-axis injection method. This is accelerated up to 8 GeV and then outputted to the storage

ring, which is repeated in 1 s intervals [43]. This can be broken down as follows: 1 GeV injection, 150 ms; electron acceleration, 400 ms; 8 GeV electron beam ejection, 150 ms; and deceleration period, 300 ms [43]. Electron synchrotrons have two klystron units set up in the klystron facility; high-frequency power for acceleration is supplied through a waveguide [41]. Progressively higher energies can be obtained if the synchrotron trajectory radius is increased and the magnetic field is strengthened. Electron beams accelerated by a synchrotron are transferred from a junction, such as in Fig. 4.32b, to a storage ring using a beam transfer setup as in Fig. 4.33. The synchrotron building, which houses the electron synchrotron, is placed in a position approximately 10 m below that of the storage ring, enters the interior of the storage ring by going underground as seen in Fig. 4.33, and is connected to the storage ring from the inside.

(3) Storage Ring

Figure 4.34 shows the storage ring size and storage electron energy of the major synchrotron radiation facilities in Japan and overseas. There are a number of synchrotron radiation facilities of various scales throughout the world, with storage rings up to 1 km or more in perimeter and storage electron energies ranging from around 0.5 GeV to 8 GeV in SPring-8. In Japan, facilities from Kyushu and the Kanto region, particularly the relatively low-energy facilities and SPring-8, which has the world's largest storage electron energy, serve as opposite ends, with a total

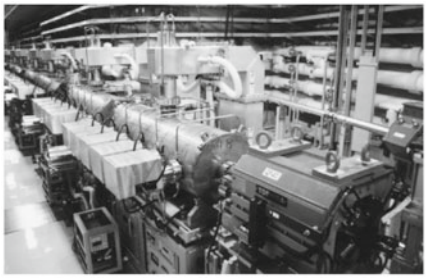

(a) High frequency acceleration cavity

(b) Beam injection section into the storage ring (right) from the beam transportation line (right)

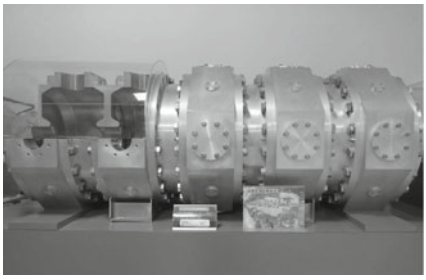

(c) 5-cell acceleration cavity for synchrotron

Fig. 4.32 Photograph of electron synchrotron in SPring-8 [37, 43] (**a**: courtesy of Hiroto Yonehara, **b** provided by Riken, and **c** is a photograph of a SPring-8 display)

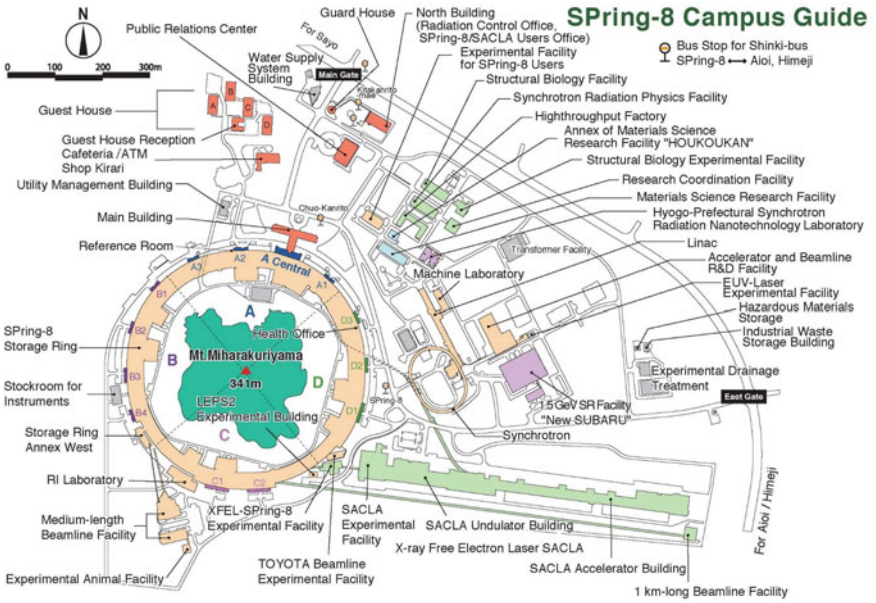

Fig. 4.33 Entire structure of SPring-8 (provided by Riken) [37]

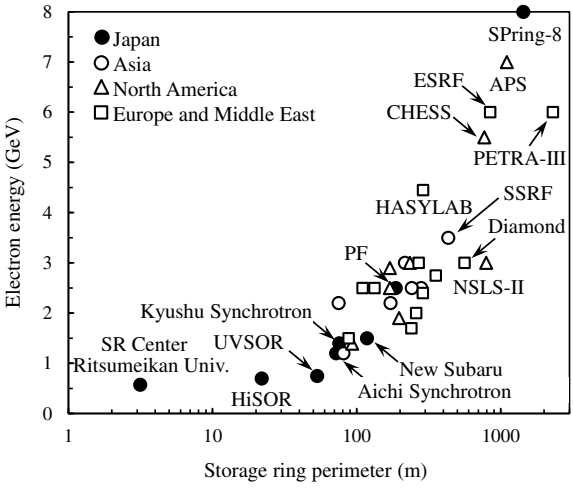

Fig. 4.34 Storage ring size (perimeter) and storage electron energy of various international synchrotron radiation facilities

of 9 synchrotron radiation facilities present in the country. Considering only the storage ring circumference, SPring-8 is no longer the world's largest facility after the construction of PETRA-III in Germany in July 2009. Considering global trends, there have been a number of smaller 3 GeV-class, high-brilliance/moderate-scale radiation facilities, with emittance values lower than 4 nm/rad, built since 2000. These include

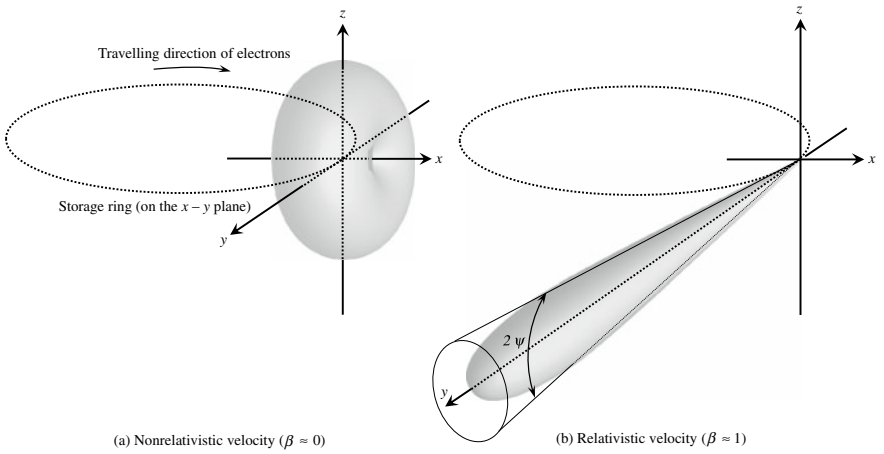

Fig. 4.35 Schematic showing the influence of electron acceleration in the horizontal direction (x-direction) on patterns of synchrotron radiation due to the bending magnet

SOLEIL in France, Diamond in the U.K., SSRF in China/Shanghai, and ALBA in Spain. It is anticipated that there will be more high-brilliance/moderate-scale radiation facilities with an emittance of 1 nm/rad or lower in the future.

As shown in Fig. 4.35a, electric *dipole radiation* is generated when applying acceleration by using bending magnets perpendicular to the direction of travel of the electron. In this case, acceleration is in the y-direction of the figure. Figure 4.35a shows the case in which β ($= v/c$), where the electron drift speed v is normalized by the speed of light c, is sufficiently small. The radiation, in this case, is 0 in the direction in which acceleration is applied and the opposite direction, and maximum in the plane perpendicular to those directions. Meanwhile, when looking at synchrotron radiation emitted from electrons at relativistic speeds ($\beta \approx 1$) from laboratory systems, radiation becomes concentrated in a narrow area referred to as the radiation cone as shown in Fig. 4.35b. When the diverging angle, in this case, is set as $2\ \psi$, the following equation is obtained:

$$\psi \approx \frac{mc^2}{E_e} \tag{4.19}$$

Here, E_e is the storage electron energy of the storage ring. Incidentally, $\beta = 0.999999998$ in the case of SPring-8 and 0.999999869 when storage electron energy is 1 GeV, effectively equal to the speed of light. If calculated using the range of E_e currently capable in synchrotron radiation facilities, the synchrotron radiation divergence is in the order of [mrad], as shown in Fig. 4.36. Based on this, synchrotron radiation can be said to have high directionality, wherein extremely high fluxes are sharply concentrated in a small area. In the case of bending magnets, electrons orbit a trajectory while generating synchrotron radiation in the direction tangent to it,

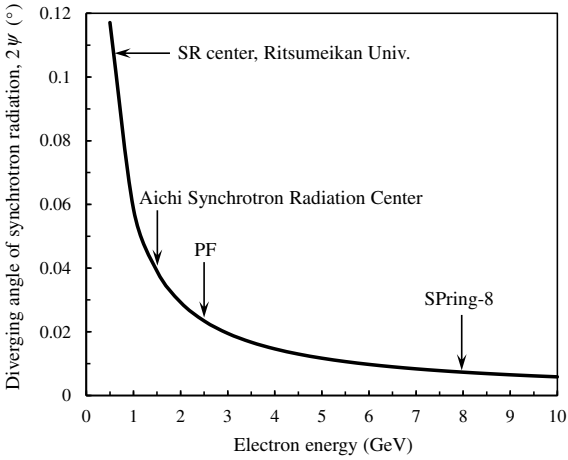

Fig. 4.36 Relationship between diverging angle of the synchrotron radiation emitted from the bending magnet and the storage electron energy of the storage ring

so synchrotron radiation diverges in the horizontal plane that includes the storage ring. This process is shown in Fig. 4.37. The divergence angle φ_B is dependent on the length of the bending magnet and is equal to 4.04° in the case of the bending magnets in SPring-8 [37]. Meanwhile, the *collimation* set by Eq. (4.19) is mostly

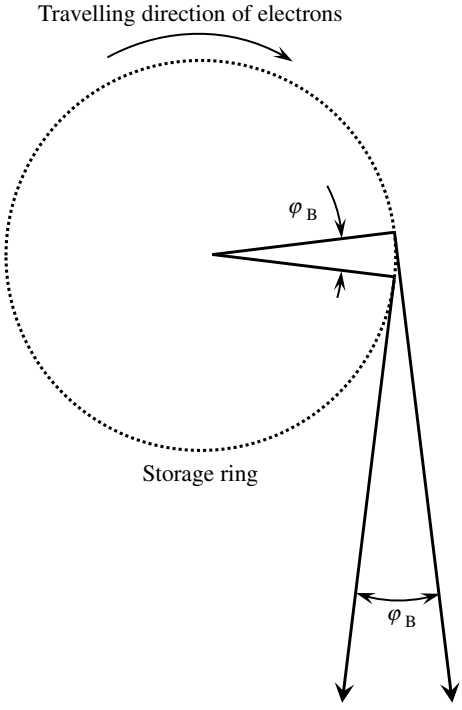

Fig. 4.37 Schematic showing the electromagnetic wave superposition and divergence in the horizontal direction of the synchrotron radiation due to the bending magnet

maintained in the direction perpendicular to the electron trajectory. The diverging angle of synchrotron radiation is 0.0036° for a 28.9 keV energy X-ray in the case of bending magnets in SPring-8 [37].

Incidentally, integrating the instantaneous *radiation power* P_e of synchrotron radiation emitted by a single electron orbiting a circular trajectory across all angles and wavelengths results in the following, where the radius of trajectory curvature (not the radius of the storage ring) is set as R [44].

$$P_e = \frac{e^2 c E_e^4}{6\pi\varepsilon_0 (mc^2)^4 R^2} \tag{4.20}$$

The total power of the synchrotron radiation is strongly dependent on the storage electron energy. Furthermore, integrating the amount of energy lost by a single electron as it circles a storage ring a single time (energy loss per turn) for the entire turn around the storage ring results in the following equation [44]:

$$\Delta E_e = \frac{e^2 E_e^4}{3\varepsilon_0 (mc^2)^4 R} \tag{4.21}$$

Table 4.6 shows the calculated ΔE_e values for the storage rings of major synchrotron radiation facilities. When E_e and R are expressed in units of [GeV] and [m], ΔE_e [keV] can be calculated as $\Delta E_e = 88.5\ E_e^4/R$. The storage electron energy in large-scale radiation facilities is high, therefore, energy loss is also extremely significant. Conversely, this amount of energy must be supplemented during that turn. For this reason, cavity spaces for conducting the high-frequency acceleration

Table 4.6 Energy loss, total radiation power, and critical energy of storage rings in representative synchrotron radiation facilities that can conduct X-ray microtomography, calculated by Eqs. (4.21), (4.22), and (4.24) [37–40]

	E_e (GeV)	R (m)	I_{sc} (mA)	ΔE_e (keV)	P_{SR} (kW)	E_c (keV)
SPring-8	8.0	39.27	100	9230	923	28.9
Aichi Synchrotron Radiation Center	1.2	2.7	300	68.0	2.04	1.4
Photon Factory	2.5	8.66	300	399	120	4.0
Kyushu Synchrotron Light Research Center	1.4	3.2	300	106	31.8	1.9
New Subaru	1.5	3.2168	300	139	41.7	2.3
ESRF	6.0	23.4	200	4900	980	20.5
APS	7.0	38.9611	200	5450	1090	19.6
ALS	1.5	4.89	400	91.6	36.6	1.5
PETRA-III	6.0	22.92	100	4660	351	20.907

of the electron and bending magnets, which curve the electron trajectory, are placed alternative in the storage ring.

In actual practice, the average stored current value (also shown in Table 4.6) should be set as I_{sc}, the electron number should be multiplied by Eq. (4.21), and this should be understood as the *total radiation power* P_{SR} from the storage ring [44].

$$P_{SR} = \Delta E_e \frac{I_{sc}}{e} \tag{4.22}$$

The P_{SR} values of representative synchrotron radiation facilities are summarized in Table 4.6. Third-generation large-scale radiation facilities like SPring-8 and ESRF are known to have a total radiation power of approximately 1 MW. Meanwhile, using Eq. (4.3) and calculating the radiation power from the various X-ray tubes from Table 4.3 shows that those from synchrotron radiation facilities have values higher by up to 8 orders of magnitude.

The *flux density* of synchrotron radiation can be determined from the following equation [45]:

$$\frac{d^3N}{dtd\Omega d\lambda/\lambda} = 3.46 \times 10^3 \gamma^2 \left(\frac{\lambda_c}{\lambda}\right)^2 \left\{1 + (\gamma\Psi)^2\right\} \left\{ K_{2/3}^2(\xi) \frac{+(\gamma\Psi)^2}{1 + (\gamma\Psi)^2} K_{1/3}^2(\xi) \right\} \tag{4.23}$$

Here, N is the photon number, λ is the wavelength of the X-ray, λ_c is the critical wavelength of the X-ray, Ω is the solid angle of radiation from the light source, $\frac{1}{\gamma} = \sqrt{1-\beta^2}$, and $\xi = \lambda_c \left\{1 + (\gamma\Psi)^2\right\}^{2/3}$. $K_{2/3}$ and $K_{1/3}$ are the modified Bessel functions; there is a useful graph regarding these functions in Wiedemann [46]. The first and second terms within the second set of parentheses on the right edge in Eq. (4.23) express the polarized components parallel and perpendicular to the trajectory plane, respectively. Furthermore, λ_c is obtained from the following equation and defined so that the total radiation power is divided into two at λ_c [45]. The critical frequency ω_c is expressed as follows.

$$\omega_c = \frac{3}{2} \frac{\gamma^3 c}{R} \tag{4.24}$$

It is clear from Eq. (4.23) that synchrotron radiation is a continuous spectrum across a wide range of wavelengths; in other words, X-rays obtained from bending magnets are white if they do not undergo spectral diffraction with a monochromator. This is depicted as a graph in Fig. 4.38, which shows that electromagnetic waves across a wide wavelength range from infrared to hard X-rays are emitted. The position of critical energy E_c, corresponding to the critical wavelength, is also illustrated in the figure. Furthermore, the critical energy values in representative synchrotron radiation facilities are shown in Table 4.6. When using X-rays, a higher storage electron energy has minor influence on the low-energy side, whereas the energy range in the high-energy side greatly increases. It is clear that large-scale synchrotron

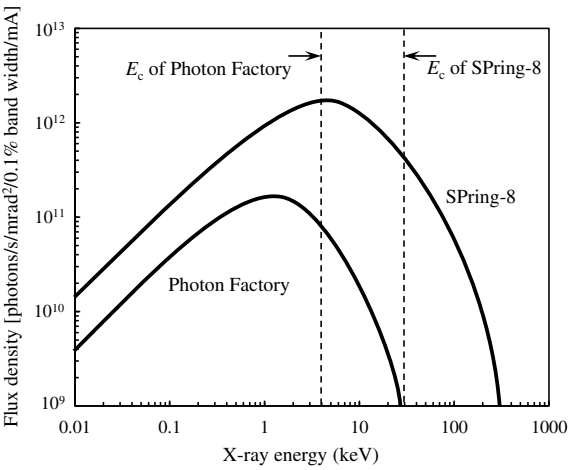

Fig. 4.38 Schematic comparing the flux density and critical energy of synchrotron radiation emitted from bending magnets in storage rings at SPring-8 and the Photon Factory

radiation facilities with high storage electron energies at a SPring-8 level are required when considering X-ray imaging of metallic materials.

Incidentally, the units of Eq. (4.23) are [photons/s/mrad^2/0.1% band width/mA], which are the number of photons emitted for a unit period of time, unit relative bandwidth, divergence angle in both the horizontal and vertical directions, and a storage current of 1 mA. Meanwhile, integrating by angle yields the *flux*. Furthermore, brilliance is dividing the flux density by the effective light source size in both the horizontal and vertical directions, and converting it to a unit surface area. The brilliance of synchrotron radiation is an important index that determines the success or failure of many experiments. Radiation facilities with low emittance are advantageous for obtaining high brilliance. Furthermore, the maximum flux value $F_{\max}$ is obtained when $\lambda = 3.4\,\lambda_c$ and can be approximated using the following equation [47]:

$$F_{max} \approx 1.29 \times 10^7 \gamma \tag{4.25}$$

Next, Fig. 4.39 shows a schematic of a basic storage ring structure. The role of the storage ring is to store electrons on a pseudo-circular trajectory for long periods while retaining a fixed amount of energy. Multiple bending magnets are set up on the trajectory to achieve this. As there is no need to increase the electron energy in storage rings, direct current is used in bending magnets. With the example of SPring-8, a total of 88 bending magnets with 0.68 T (Tesla) are set up (Fig. 4.40a) and the radius of curvature due to the bending magnet is set as 39.27 m [37]. These bending magnets are dipoles, however, as in the schematic in Fig. 4.39, there are also quadrupole (Fig. 4.40b) and six-pole (Fig. 4.40c) magnets set up on the trajectory; the former is for the convergence of the electron beam and the latter for correcting the deviations in the closed orbit or focal spot location. Furthermore, there are forty 7-m linear sections and four 30-m linear sections set up for a single orbit in SPring-8 [37]. High-frequency accelerator cavities for supplementing the radiation loss shown

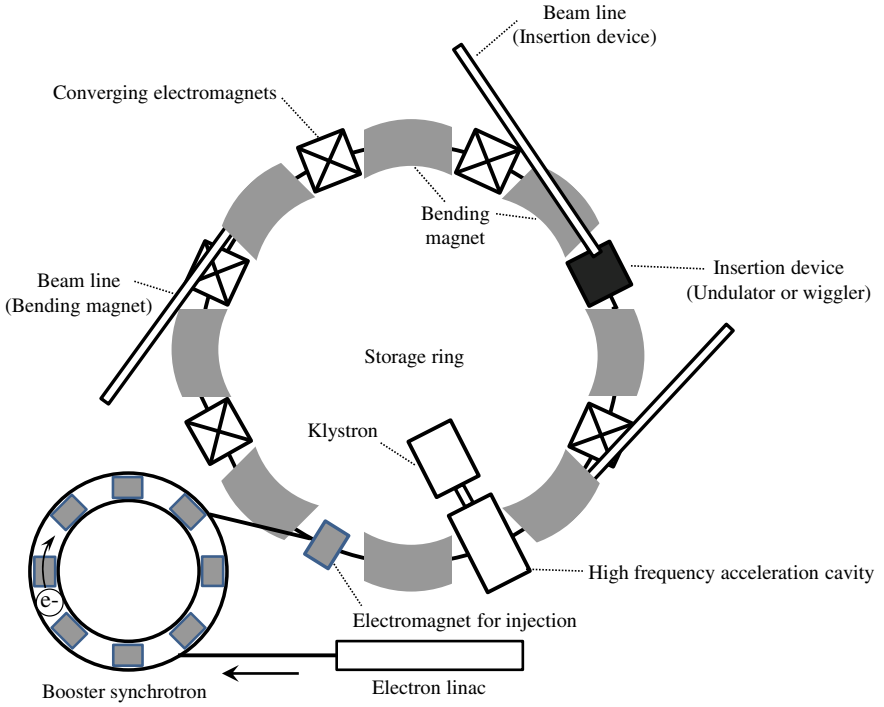

Fig. 4.39 Simplified schematic showing a basic structure of a storage ring in a synchrotron radiation facility

in Eq. (4.21) are connected to klystrons through waveguides and set up in the linear section. This basic principle is the same as a linac. Furthermore, the insertion device discussed in (4) is also set up in the linear section. The electron beam itself propagates through the vacuum chamber with an elliptical cross-section, as shown in Fig. 4.40d. The origin of the elliptical shape was made to resemble the cross-sectional shape of the electron beam. Furthermore, an extremely high vacuum of 10^{-8}–10^{-6} Pa is maintained in the chamber interior in the case of SPring-8 [37]. The vacuum chamber is made of an aluminum alloy extrusion that is non-magnetic and has favorable vacuum characteristics, as well as limited radioactivation.

Incidentally, top-up operations have been conducted at SPring-8 since 2004. Typically, the storage current gradually decreases due to the scattering by residual gas in the vacuum chamber or scattering among electrons within bunches [48]. To address this, top-up operations involve systematically yet frequently repeating electron beam injections from the injector to macroscopically maintain the storage current. As shown in Fig. 4.41, past methods have involved increasing the storage current value to around 100 mA through electron beam injections from the electron synchrotron twice a day and subsequently decreasing it to 75 mA over the course of half a day [37]. In response, image quality obtained with X-ray imaging varied considerably

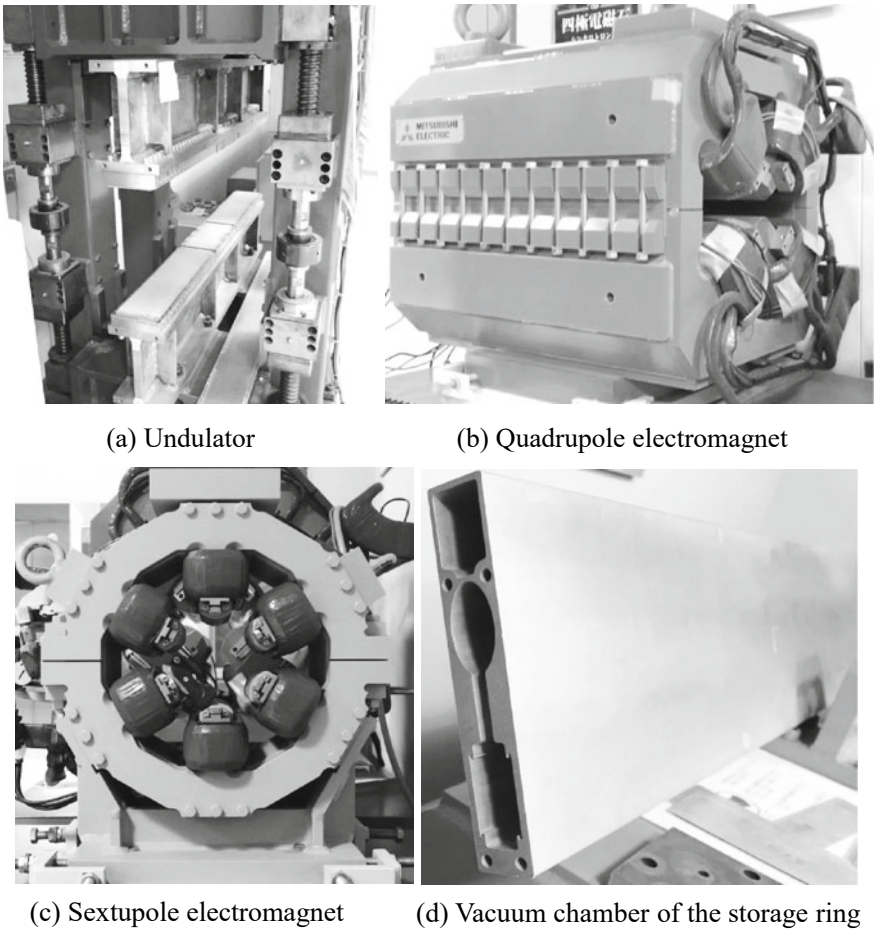

(a) Undulator (b) Quadrupole electromagnet

(c) Sextupole electromagnet (d) Vacuum chamber of the storage ring

Fig. 4.40 Constituent machines of the storage ring in SPring-8; photographs of SPring-8 displays are shown

before and after injection; currently, 1 to 3 injections every 1 to 5 min for a 100-mA storage current around 100 mA [37] control variations in the storage current to less than 0.1% [48]. For this reason, it can be guaranteed that there will be no changes in image quality or spatial resolution due to variations in storage current across the course of a single day of beam time when conducting X-ray imaging. Currently, top-up operations are a global standard used in the operation of high-brilliance light sources [48].

(4) Insertion Device

An *insertion device* (ID) is a device that is inserted in the linear portion between bending magnets to obtain higher quality synchrotron radiation than that from

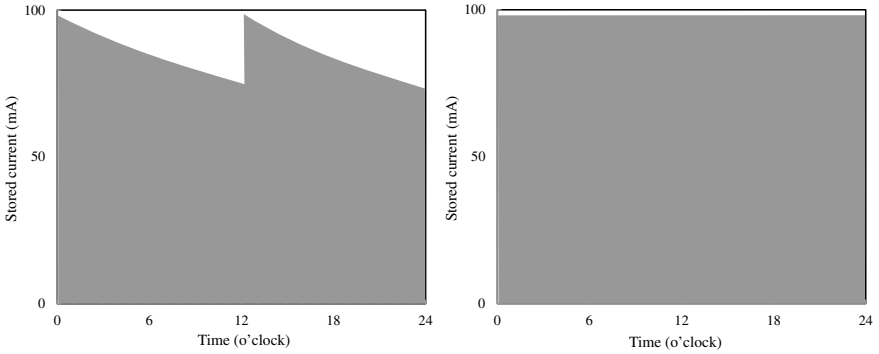

Fig. 4.41 Schematic showing the storage current value changes of the storage ring when top-up operations are and are not conducted [37]

bending magnets in terms of brilliance or directionality. There are two types of insertion devices: an *undulator* and a *wiggler*. Third-generation radiation facilities like the SPring-8 often use undulators in particular. For beamlines in SPring-8, such as BL20B2, the "B" that comes after the beamline number refers to the bending magnet, the "XU" in beamlines such as BL20XU refers to undulators, and the "W" in beamlines such as BL08W refers to wigglers. An undulator displayed in SPring-8 is shown as an example of an insertion device in Fig. 4.42. A schematic of an insertion device is also shown in Fig. 4.43. A periodic magnetic field as in Fig. 4.43 can be created by alternating the N- and S-poles of multiple permanent magnets as well as placing them above and below the electron trajectory. Electrons flying through this environment will follow a meandering path. The radiation generated at each

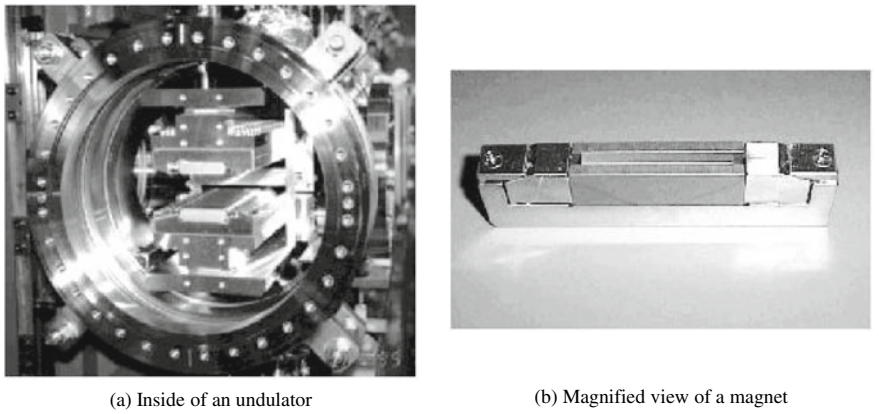
(a) Inside of an undulator

(b) Magnified view of a magnet

Fig. 4.42 Undulator of a storage ring in SPring-8 (courtesy of Yoshio Suzuki, formerly of SPring-8)

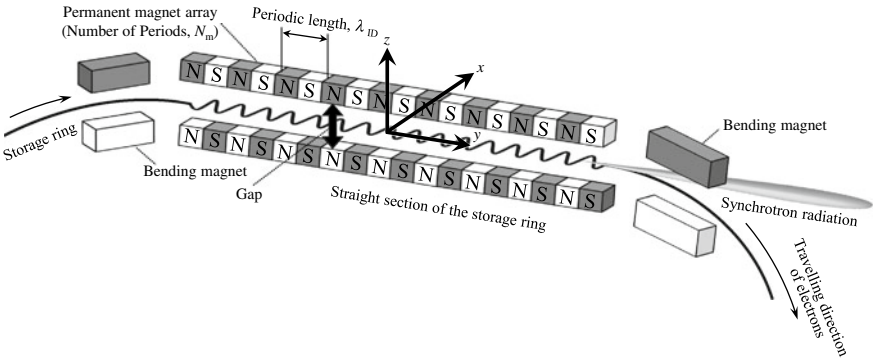

Fig. 4.43 Schematic showing radiation generation from an insertion device placed within a storage ring in a synchrotron radiation facility

magnet will be superimposed due to this, greatly increasing intensity and directionality. Changing the *gaps* of the magnets above and below the trajectory alters the magnetic field intensity as well as the energy of the synchrotron radiation. Permanent magnets are generally used to reduce the periodic length while creating a strong magnetic field. Neodymium magnets (10-mm gap, 0.78 T maximum magnetic field), where neodymium, iron, and boron are sintered together as the primary compositions, are used at SPring-8. Magnets need to be placed and coordinated to fulfill the following condition to ensure the electron beam does not deflect as a result of placing an insertion device:

$$\int B_z dy = 0 \tag{4.26}$$

The deflection angle of the electron trajectory from the y-axis in Fig. 4.43 is expressed using the constant K parameter, as shown below:

$$\Phi_{max} = \frac{K}{\gamma} \tag{4.27}$$

Here, K is expressed as follows:

$$K = \frac{eB_0\lambda_{ID}}{2\pi mc} \tag{4.28}$$

λ_{ID} is the periodic length of the insertion device magnet (see Fig. 4.43 for reference) and B_0 is the maximum value of the magnetic field. General rules-of-thumb for undulators and wigglers are $K \leqq 1$ and $K \gg 1$, respectively. However, undulators with $K > 1$ are also used, therefore, in actual practice, the distinction between the two is based on the coherency of the obtained X-rays. Synchrotron radiation characteristics from undulators and wigglers are entirely different. We can see from Eq. (4.28)

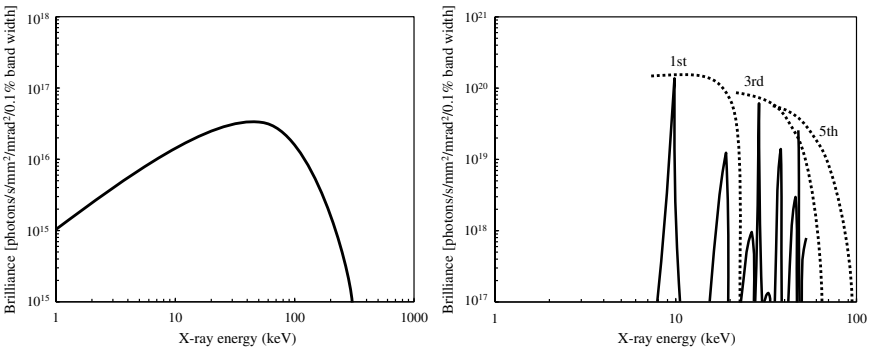

(a) Wiggler (BL08W) (b) Undulator (BL20XU)

Fig. 4.44 Schematic comparing the performances of an undulator and wiggler in a SPring-8 storage ring [37]

that the $K \gg 1$ condition is satisfied when the magnetic field is relatively strong. The spectral shape is as shown in Fig. 4.44a in the case of the wiggler and is similar to the bending magnet in Fig. 4.38 [37]. However, bending magnets have higher brilliance and are shifted to the high-energy side. This is because with wigglers, there is insufficient interference from the radiation emitted from each magnet, and they are simply added based on photon numbers. For this reason, the brilliance becomes greater by a factor of $2N_\mathrm{m}$ when $2N_\mathrm{m}$ magnets are arranged. In contrast, this value is the sum of amplitudes as discussed later in undulators, so the intensity becomes proportional to ${N_\mathrm{m}}^2$ under conditions where it is mutually strengthened through interference. Furthermore, the critical energy, in the case of the wiggler, becomes considerably higher than was the case with bending magnets. Meanwhile, the peak can be shifted to the low-energy side if the magnetic field is weakened. For this reason, the wiggler is also referred to as a *wavelength shifter*. Incidentally, the BL08W at SPring-8, which is a beamline with a wiggler installed, has values of periodic length λ_ID of 12 cm, periodicity N_m of 37, a minimum gap of 30 mm, and a maximum K-value of 9.89.

Meanwhile, the undulator magnet interval is shorter than a wiggler and its magnetic field is also weak. In the case of an undulator, the obtained synchrotron radiation becomes a *quasi-monochromatic beam* (*pink beam*), as shown in Fig. 4.44b [37]. The wavelength bandwidth, in this case, is shown in the following equation:

$$\frac{\Delta\lambda}{\lambda} = \frac{1}{nN_m} \tag{4.29}$$

For example, the BL20XU at SPring-8, which is a high-resolution imaging beamline with a vacuum-sealed undulator, has values of $\lambda_\mathrm{ID} = 2.6$ cm, periodicity $N_\mathrm{m} = 173$, a minimum gap of 7 mm, and a maximum K value of 2.12. Thus, $\Delta\lambda/\lambda$ is below 5.8×10^{-3}. However, this is an ideal scenario, where the electron energy, position,

and direction are entirely uniform. Current storage rings have a limit of $\Delta\lambda/\lambda \lesssim 10^{-2}$ depending on the electron energy distribution. As in Eq. (4.29) and Fig. 4.44b, the bandwidth becomes even narrower with *harmonics* (X-rays that have an integral multiple of energy of the fundamental wave). Figure 4.44b has a spectrum in which the fundamental wave and multiple harmonics, which have higher energy (generally, higher-order waves at an odd order), are superimposed. The wavelength λ_n of the n-order harmonics is expressed with the following equation:

$$\lambda_n = \frac{\lambda_{ID}}{2n\gamma^2}\left(1 + \frac{K^2}{2} + \gamma^2\theta^2\right) \tag{4.30}$$

Here, θ is the angle between the y-axis (beam direction) and the observation axis of Fig. 4.43; the wavelength becomes shortest in the y-axis and that the wavelength increases with increased θ. Although the fundamental wave is strongest, higher-order harmonics also strengthen with $K > 1$. The undulator, in which $K > 1$ is referred to as a strong magnetic field undulator, promotes the generation of harmonics [49].

Incidentally, as λ_n is proportional to K^2, λ_n can be controlled by Eq. (4.28) through magnetic field adjustment. Undulators mainly use permanent magnets, so this refers to the adjustment of the gaps between the rows of overlying and underlying magnets. Permanent magnets are vacuum-sealed (degree of vacuum 3×10^{-8} Pa [37]) inside chambers at SPring-8 and the minimum gap can be reduced to 8 mm. For this reason, an X-ray energy range of 5–80 keV can be covered by using the 1st- through 5th-order waves of the undulator [37]. Meanwhile, there is no point in adjusting the gaps in wigglers that have a wide bandwidth.

In the case of the undulator, the brilliance becomes larger by a factor of N_{m}^2 when $2N_{\mathrm{m}}$ magnets are arranged. This is because the radiation generated by each magnet strengthens each other through interference; in other words, radiation that is brighter than bending magnets or wigglers by orders of magnitude can be generated. Furthermore, the directionality of the obtained synchrotron radiation also becomes significantly higher. The diverging angle φ_u of the synchrotron radiation is as expressed below:

$$\varphi_u \approx \sqrt{\frac{\lambda}{N_m \lambda_{ID}}} = \frac{1}{\gamma}\sqrt{\frac{1 + K^2/2}{2nN_m}} \tag{4.31}$$

$N_m \lambda_{ID}$ is the length of the row of magnets; for example, φ_{u} is approximately 3.7 μ rad for the leftmost peak in Fig. 4.44b. Furthermore, the diverging angle becomes approximately $1/\sqrt{N_m}$ compared to bending magnets when considering the fundamental waves of undulators. The reason why brilliance is high in undulators can be attributed to the perfectly mutually strengthened synchrotron radiation from each magnet due to interference in the optical axis only for a specific wavelength. However, the total radiation power even in undulators is approximately the same as that in bending magnets. In actuality, and as shown in Fig. 4.29, only X-rays that are weaker than

those from wigglers or bending magnets can be observed at wavelengths removed from the undulator peaks.

Finally, if we assume that the spatial coherence discussed in Sect. 2.2.2 (3) can be approximated with a Gaussian function, the beam size σ of synchrotron radiation emitted from an undulator can be expressed as follows. However, the Gaussian function, in this case, cannot be considered a good approximation, so care must be taken to note that the following equation does not accurately reflect the effective beam size.

$$\sigma = \frac{\sqrt{\lambda N_m \lambda_{ID}}}{4\pi} \tag{4.32}$$

Meanwhile, the temporal coherence similarly discussed in Sect. 2.2.2 (3) is expressed as follows for an undulator:

$$l_t = \frac{\lambda^2}{2\Delta\lambda} = \frac{N_m \lambda_{ID}\left(1 + K^2/2\right)}{4\gamma^2} \tag{4.33}$$

In this manner, temporal coherence is improved by increasing the length of the row of magnets in the undulator. This effect is proportional to the length of the row of magnets. Spatial coherence is not dependent on undulator length in the case of a completely coherent light source.

(5) Beamline

Using SPring-8 as an example, there are a total of 57 beamlines (62 are installable), as shown in Fig. 4.45 [37]. Of these, the BL20XU, BL20B2, BL47XU, BL37XU, and BL19B2 are used for X-ray imaging. Beamlines are composed of a *front end* (*FE*), *optics hutch*, and *experimental hutch*. In SPring-8, the distance from the X-ray source to the entrance of the front end is 10–20 m and the distance from there to the front-end terminal is another 10–20 m, with a total distance from the X-ray source when considering the experimental hall terminal of approximately 80 m (Fig. 4.46a [37]). The beamlines BL20XU and BL20B2 extend out of the experimental hall, with a total extension of 250 m (Fig. 4.46b [37]). A detector and sample rotation stage (discussed later), are set up in the experimental hutch.

Synchrotron radiation generated at the storage ring is introduced in the front end, composed of a gate valve for vacuum shielding, *main beam shutter* (*MBS*), *slit*, and a *beryllium window* (refer to Fig. 4.47 [50]). The front end is maintained in an ultra-high vacuum with an ion pump and titanium getter pump. Furthermore, this is stored in what is referred to as a storage unit and general users are not permitted to enter. This storage unit is covered by a thick concrete shielding wall to ensure that gamma rays, neutrons, and excess synchrotron radiation generated at the storage ring does not enter the experimental hall. The function of the front end is to guide only high-quality synchrotron radiation near the optical axis (y-axis of Fig. 4.43) of the undulator, shielding synchrotron radiation. Unneeded synchrotron radiation, which is distant from the optical axis and removed by slits, is cut by XY slits and released

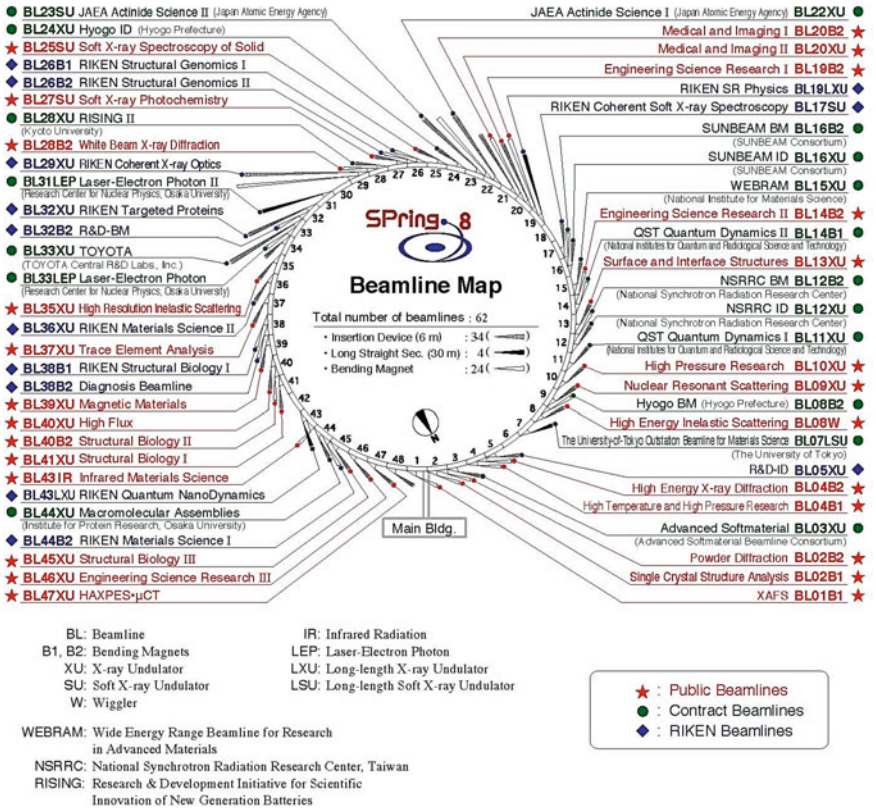

Fig. 4.45 Examples of beamlines in synchrotron radiation facilities (SPring-8 beamline map provided by Riken. Current as of April 1st, 2017) [37]

as heat. Therefore, it is important to ensure that the front end is properly treated for high heat loads; for example, the total power for BL20XU in SPring-8 would be 13.83 kW when the minimum gap is 7 mm [51]. Most of this enters the front end slit and the output is approximately 290 W when the slit opening is 0.5 mm (vertical) × 0.8 mm (horizontal) [51]. This difference of approximately 13.5 kW is processed as heat. The main beam shutter is the general term for the *absorber* that shields the heat component and the *beam shutter* that shields the radiation component; both work together during operation [52]. For example, closing the main beam shutter involves first closing the absorber and then automatically closing the beam shutter [52]. This prevents heat loads on the beam shutter, which is not cooled. In the case of SPring-8, a 38-cm-thick tungsten block is used for the beam shutter and a water-cooled copper block with high heat conduction is used for the absorber. Both are raised and lowered using a compressed-air cylinder [52].

Figure 4.48 shows the workstation display of an experimental hutch beamline where a front end is controlled. Some of the machinery for a front end can be easily

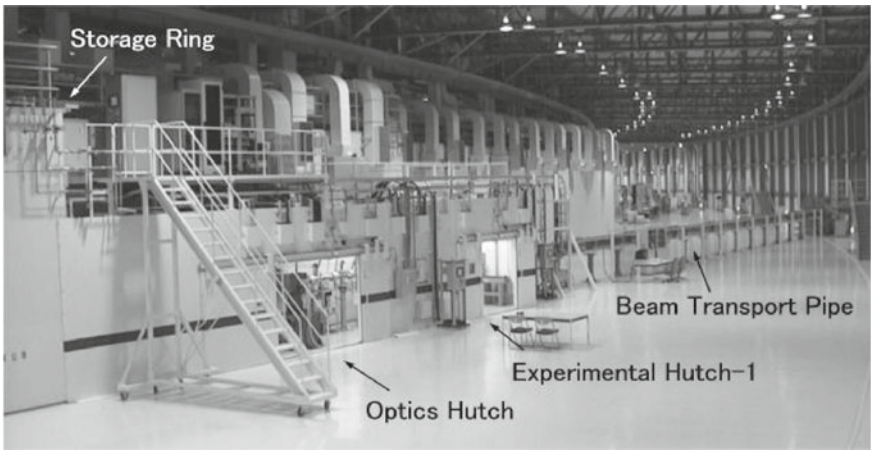

(a) Appearance of beam lines in the experimental hall

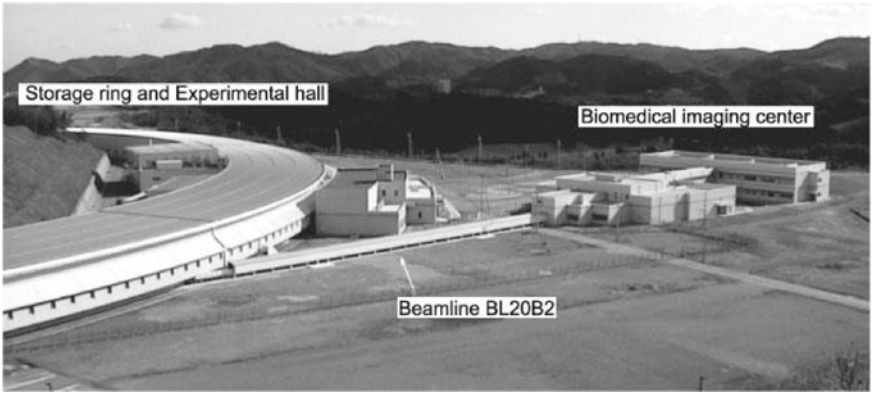

(b) Appearance of beam lines outside the experimental hall

Fig. 4.46 Photograph of beamlines in synchrotron radiation facilities (courtesy of Kentaro Uesugi from SPring-8 for BL20B2 at SPring-8) [37]

controlled by a general user from the experimental hutch. However, troubles with the front-end machinery can damage the monochromator of the beamline in use and can at times have serious effects on other beamline experiments through a beam abort; hence, sufficient care must be taken. Please refer to specialized texts for further detail on this [52].

The beryllium window is an important component with regard to the front end when the user conducts X-ray imaging. As shown in Fig. 4.49, the beryllium window shields both the ultra-high front end vacuum (10^{-8}–10^{-7} Pa) and the high optics hutch vacuum (10^{-6}–10^{-3} Pa), as well as enabling the transmission of only hard X-rays above approximately 3 keV [52]. The beryllium window of SPring-8 is comprised of a high-purity beryllium foil affixed on a water-cooled copper mask and a structure to withstand heat loads due to the white X-ray. For example, there are two beryllium

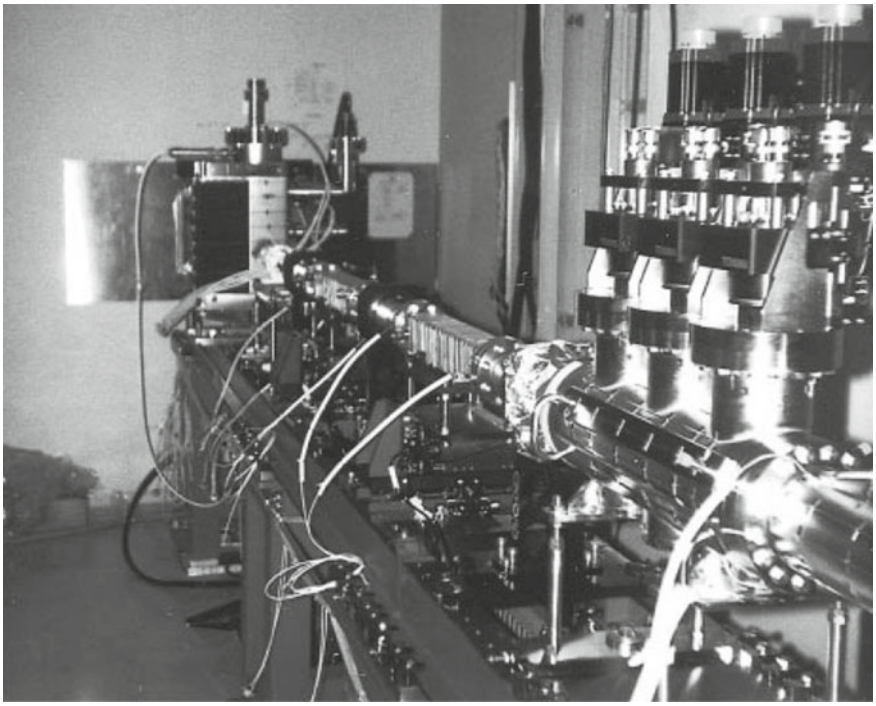

Fig. 4.47 Example of a beamline in a synchrotron radiation (courtesy of Yoshiharu Sakurai of SPring-8 for BL47XU at SPring-8) [50]

windows with thicknesses of 250 μm in the upstream side of the optics hutch of BL20XU of SPring-8. The downstream side of the optics hutch is shared with the experimental hutch and there are two PVD-based beryllium windows with a 60 μm thickness (two 30 μm -thick windows affixed together). The surface roughness of the beryllium foil, inclusion particles due to trace impurities, and material defects like pores all produce fringe patterns or intensity irregularities referred to as *speckle noise* in the image obtained with X-ray imaging, therefore, care must be taken.

As can be observed in Fig. 4.50 [37], the X-ray coming out of the front end is not immediately released into the atmosphere, instead, passing through a vacuum pipe where both ends are sealed with beryllium and guided into a *monochromator*. The monochromators for BL20XU and BL20B2 in SPring-8 are set up 46 and 36.8 m, respectively, from the beam source. There are two experimental hutches in BL20XU, with the first experimental hutch placed 80 m from the beam source and capable of using a beam size of 0.7 mm (vertical) × 1.4 mm (horizontal). The second experimental hutch is placed 245 m from the beam source and is capable of using a beam size of approximately 2 mm (vertical) × 4 mm (horizontal) [37]. A flux of 10^{13} [photons/s/mm^2] can be obtained when a Si (111) plane is used on the monochromator in the first experimental hutch [37]. Meanwhile, BL20B2 has three experimental

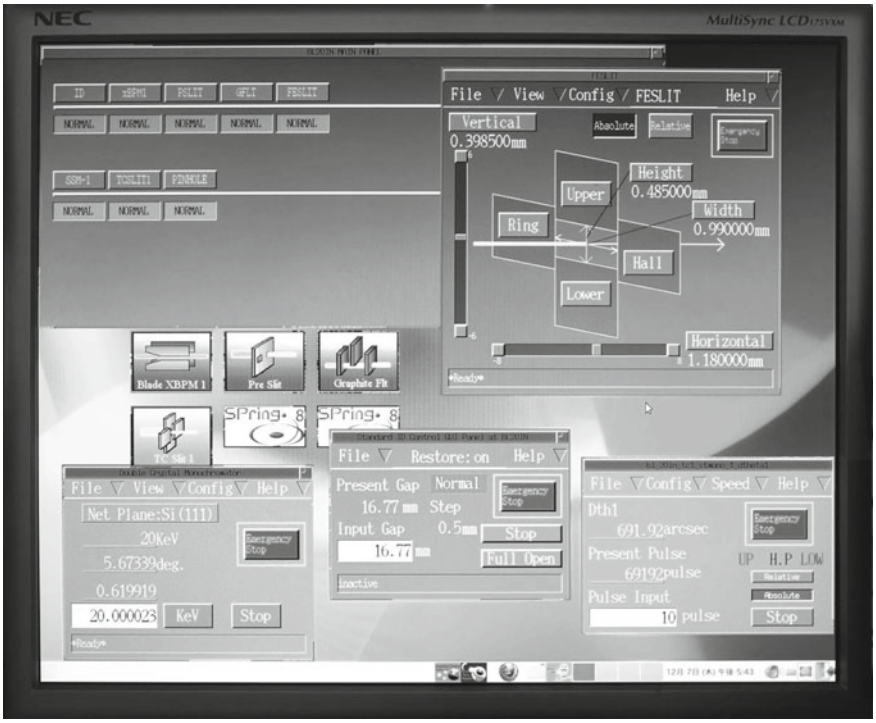

Fig. 4.48 Workstation display of the front-end slit and monochromatorcontrolling beamline in the experimental hutch of the synchrotron radiation facility (BL20XU at SPring-8)

hutches, with the first experimental hutch being located 42 m from the light source. The useable beam size is 75 mm (vertical) × 5 mm (horizontal). The second and third experimental hutches are located 200 m and 206 m, respectively, from the beam source and are capable of using a beam size of approximately 300 mm (vertical) × 20 mm (horizontal) [37]. A flux of 6.5×10^9 [photons/s/mm^2] can be obtained when a Si (111) plane is used in the monochromator in the first experimental hutch [51].

Monochromators include *diffraction grating-*, *multilayer-*, and *perfect crystal-*types. The diffraction grating-type has multiple grooves etched at equal intervals and parallel on a substrate. They are used for soft X-rays. The multilayer-type has both light and heavy thin films periodically layered on top of each other. The beam becomes approximately monochromatic with an *energy resolution* $\Delta E/E$ of around 10^{-2}, whereas the *bandwidth* expands about 100 times more than that in a perfect crystal-type. These specifications are considered to be sufficient for small-angle scattering or X-ray imaging based on absorption contrast, which does not have any issues with regard to quantitative characteristics. Multilayer monochromators are used at approximately half of the beamlines in ESRF. Meanwhile, perfect crystal-type monochromators can achieve an energy resolution of around 10^{-4}. For example, X-rays with an energy of 20 keV have a wavelength of 0.062 nm and wavelength

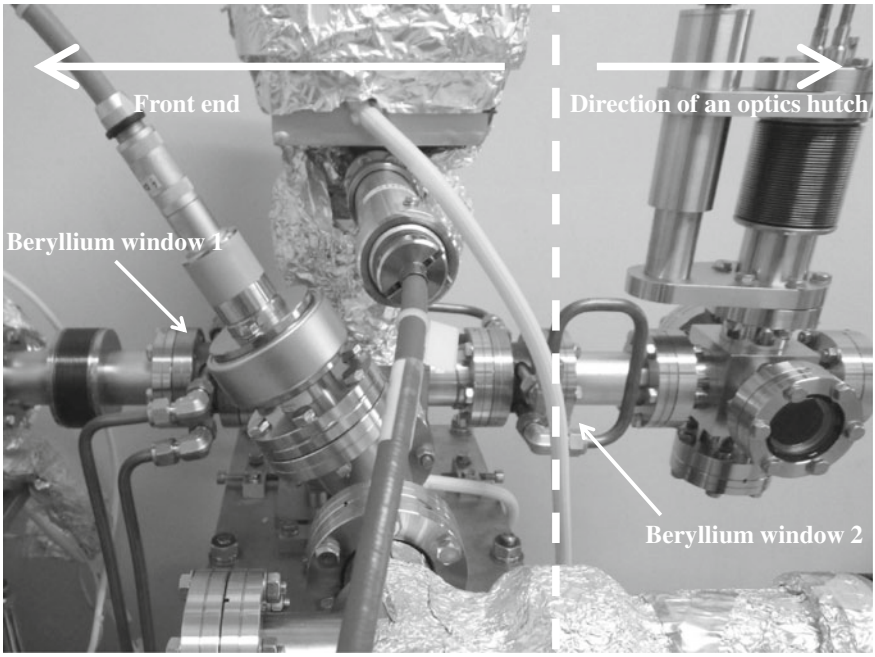

Fig. 4.49 Beryllium window in a beamline in a synchrotron radiation facility (courtesy of Kentaro Uesugi of SPring-8 for BL20XU at SPring-8)

dispersion of around 0.000006 nm. Except for soft X-ray beamlines, almost all of the beamlines in SPring-8 use *double crystal monochromators*, which use perfect crystals. Double crystal monochromators are briefly discussed below.

The Bragg condition shown below is the basis for X-ray spectroscopy using a monochromator (Fig. 4.51a):

$$2dsin\theta_B = n\lambda \tag{4.34}$$

Here, d is the lattice spacing and θ_B is the Bragg angle. However, the X-ray beam leaves the beamline axis in diffraction based on a single crystal (Fig. 4.51b), so double crystal monochromators use two crystals to guide X-ray beams parallel to the incident beam and in the direction of the experimental hutch. As seen in Fig. 4.51c, translating/rotating stepping motors are attached to each crystal and the first crystal translates up and down as well as front to back to maintain a constant outputted beam position even if the energy is changed and the Bragg angle alters. The user has to make fine adjustments in the energy and first crystal angle ($\Delta\theta_1$) from the experimental hutch shown in the display in Fig. 4.48, ensuring that both crystals are parallel and the beam hits the sample.

Other than the fundamental wave, n-order waves with a wavelength of $1/n$ transmit through the monochromator with the Bragg condition using the same set up. This

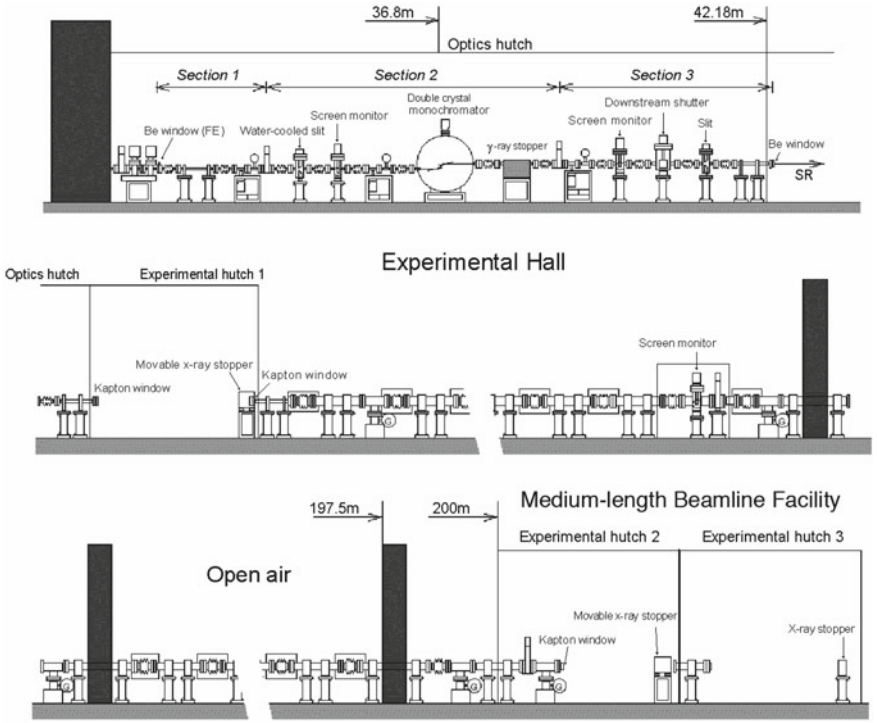

Fig. 4.50 Example of a beamline in a synchrotron radiation facility (courtesy of Kentaro Uesugi of SPring-8 for BL20B2 at SPring-8)

has the possibility of inducing errors in the quantitative analyses conducted using monochromaticity or by creating artifacts. The X-ray diffraction angle range due to a plate crystal such as in Fig. 4.51b can be assessed with the *Darwin width* ω; in other words, the monochromator can diffract X-rays by an angle equivalent to the Darwin width, with the Bragg angle at the center [53].

$$\omega = \frac{2.12}{sin2\theta_B}\frac{r_e\lambda^2}{\pi V}C|F_{hr}|e^{-B\left(\frac{sin\theta_B}{\lambda}\right)^2} \tag{4.35}$$

Here, $r_e = e^2/(m_e\ c^{\ 2})$ is the classical electron radius, V is the volume of the monochromator material per unit lattice, C is the polarization factor, F_{hr} is the crystal structure factor determined from the real part of the atomic scattering factor, and $e^{-B\left(\frac{sin\theta_B}{\lambda}\right)^2}$ is the Debye-Waller factor [53]; F_{hr} and $e^{-B\left(\frac{sin\theta_B}{\lambda}\right)^2}$ are shown in reference [53]. The Darwin width when the X-ray energy is 10 keV is 5.9" and 1.4" for Si (111) and Si (333), respectively, being roughly proportional to $1/n$. At an energy of 100 keV, they each become approximately 1/10 at 10 keV [53]. Meanwhile, higher-order harmonics are proportional to $(1/n)^2$ and n-order harmonics can be cut without

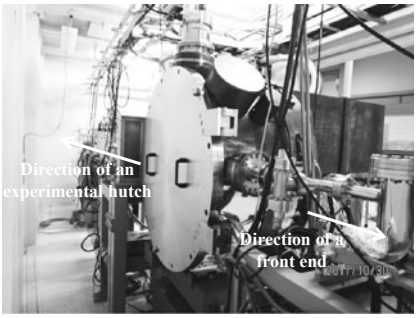

(a) Appearance of a monochromator (BL20XU)

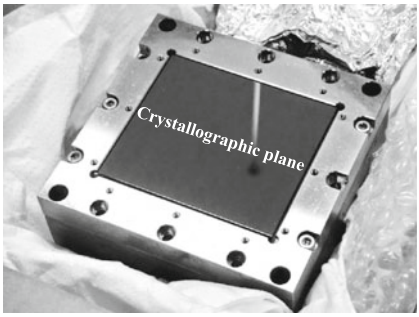

(b) Silicon crystal with its holder (BL20B2)

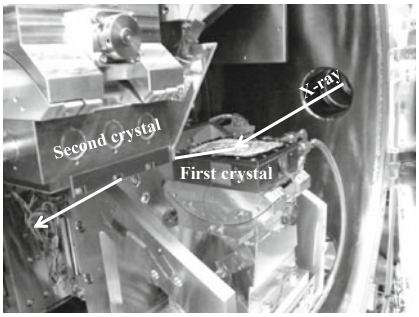

(c) Inside of a monochromator (BL20B2)

Fig. 4.51 Photograph of a monochromator set up in a beamline of a synchrotron radiation facility (courtesy of Kentaro Uesugi of SPring-8 for BL20XU and BL20B2 at SPring-8) [37]

utilizing a harmonic cutting mirror using this and shifting it by an angle equivalent to the Darwin width of the *n*-order harmonic from the Bragg angle. Taking Si (111) reflection as an example, shifting the angle so that the fundamental wave intensity is 90–80% of the peak as a result, orders higher than (333) can be cut without losing much of the fundamental wave intensity ((222) reflection is prohibited and thus does not exist). This type of diffraction angle adjustment is referred to as *detuning*.

Silicon is primarily used as the crystal for diffraction. Other X-ray spectroscopy crystals include indium antimonide (InSb), crystallized quartz (SiO_2), diamonds (C), alumina (Al_2O_3), beryl, and yttrium boride (YB_{66}). The lattice constants of each are greater than silicon and are suited for low energies such as soft X-rays.

Incidentally, the lattice spacing of silicon crystals needs to be made completely homogenous to prevent X-ray intensity variations in synchrotron radiation facilities that use X-rays in areas between several m to 200 m away from the monochromator. Polycrystal silicon is not suited for this and lattice defects or impurity atoms in the solution must be removed insofar as possible even in single crystals. For this reason, SPring-8 uses artificial silicon grown unidirectionally using the floating zone melting method, which has a purity of 99.999999999% [52]. Furthermore, any strains introduced due to crystal cutting are removed beforehand using machine polishing and etching [52]. Crystals whose Si (111) plane has shown in its surface can be

exchanged with those whose Si (220) plane has shown in its surface for the analyzer crystals in SPring-8 BL20XU [37]. These two crystals can enable the use of X-rays with energies of 7.62–37.7 keV and 37.7–61 keV, respectively [37]. Both are cooled using an indirect cooling method based on liquid nitrogen [37]. The energy values at BL20B2 are as follows: Si (111), 5.0–37.5 keV; Si (311), 8.4–72.5 keV; and Si (511), 13.5–113.3 keV [37]. The lattice spacing $2d(h\ k\ l)$ in the $(h\ k\ l)$ plane can be determined using the following equation:

$$2d(hkl) = \frac{2a}{\sqrt{h^2 + k^2 + l^2}} \tag{4.36}$$

Here, a is the lattice constant and equal to 5.4310623 Å (25 °C) for silicon. The energy range covered by each crystal can be calculated if we assume an incidence angle of 3–27°. However, care must be taken as Si (311) has a flux that is smaller than Si (111) by several factors; Si (511) has a flux that is even smaller by several more factors. In contrast, the energy resolution is expressed as shown in the following equation with the incident beam angle divergence φ and ω being determined from the beam source emission angle and slit:

$$\frac{\Delta\lambda}{\lambda} = \sqrt{\varphi^2 + \omega^2} cot\theta_B \tag{4.37}$$

Thus, energy resolution increases when a higher-index plane is used.
A *gamma-ray stopper* is set up behind the monochromator, as shown in Fig. 4.52.

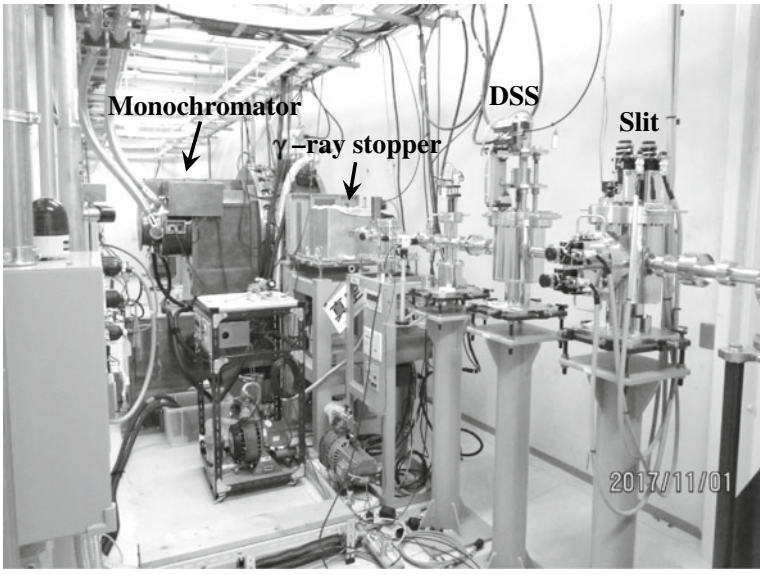

Fig. 4.52 Optics hutch of a beamline in a synchrotron radiation facility (courtesy of Kentaro Uesugi of SPring-8 for BL20XU at SPring-8)

Gamma rays at a level of several GeV are produced from *bremsstrahlung* when the electron beam passes through trace amounts of residual gas in the storage ring; the gamma-ray stopper is set up to stop these gamma rays. Gamma-ray generation is the same *bremsstrahlung* from X-ray tubes but with a frontward directionality due to its extremely high electron energy similar to synchrotron radiation. For this reason, only a narrow area near the optical axis must be shielded. Lead blocks with 30- to 35-cm thickness are used in SPring-8 [52] and monochromatic X-rays pass through a pathway that is offset by approximately 30 mm. Behind this is the *downstream shutter* (*DSS*), as shown in Fig. 4.52. This is for shielding the monochromatic X-rays after spectral diffraction. Closing the DSS enables synchrotron radiation to irradiate the monochromator even when the user is working at the experimental hutch, hence, the thermal stability of the monochromator can be assured. Typically, a sealed lead block with a 10-cm thickness is brought up and down using an air cylinder. A 9.4 cm-thick lead block is used as a DSS in SPring-8 [52]. There is also a slit downstream of the monochromator (transport channel slit, TC slit); however, with the exception of special experiments, only the front-end slit is used.

4.2 Filter

A filter is used for the absorption of endogenous X-rays generated in the window material or target of X-ray tubes, as well as for the systematic lowering of incident X-ray intensity and selective attenuation of low-energy components in incident X-rays by inserting thin metal plates between an X-ray source and sample. They are a particularly important component in industrial X-ray CT scanners and, with regard to the latter, they are used for reducing artifacts referred to as *beam hardening*, discussed later in Sect. 7.6. The filter can be adjusted to the imaging conditions corresponding to the sample and scanner by changing the inserted metal type and plate thickness. Industrial X-ray CT scanners include those with multiple filters installed, while some automatically select the optimal filter out of several. An example of a filter changer in commercially-available X-ray CT scanners for industrial use is shown in Fig. 4.53.

Figure 4.54 shows a schematic of the effects of filter insertion. X-ray intensity in the low-energy side greatly decreases with the insertion of a filter and the X-ray energy peak shifts to higher energies. The latter is referred to as beam hardening, where this becomes an artifact that appears in the sample. For this reason, removing low-energy components beforehand with a filter is a useful strategy for preventing artifacts. Filter 2 in the figure has elements with an absorption edge at an energy lower than K_α X-rays, where virtually all high-energy components above the absorption edge have been cut. This is used in X-ray diffraction, for example, by combining a tube with a copper target and a nickel filter, K_β X-rays and continuous X-rays in the short-wavelength side are eliminated, and almost all of the spectrum is composed of close to monochromatic X-rays derived from K_α X-rays. This is because the nickel absorption edge is located between the K_α and K_β X-rays. The absorption edge effect in Fig. 4.54 is considered problematic when conducting 3D imaging. For this reason,

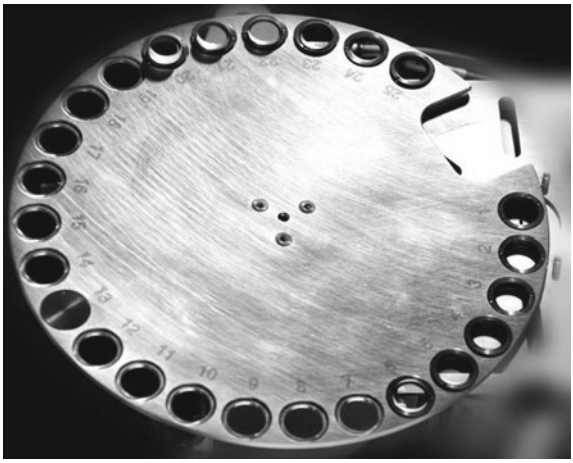

Fig. 4.53 Example of a filter changer used in an X-ray CT scanner. A filter changer was incorporated in a Karl Zeiss AG ZEISS Xradia 520 Versa (Fig. 6.18) (courtesy of Nobuhiro Hayamizu of Karl Zeiss AG)

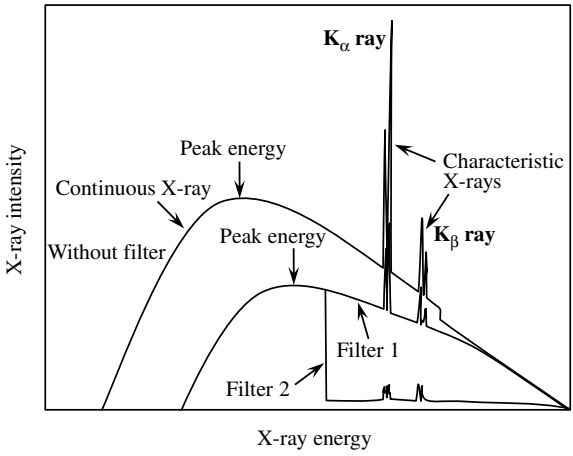

Fig. 4.54 Schematic showing the effect of a filter on X-ray intensity when using an X-ray tube. The figure shows the effects of Filter 1, composed of an element that has no absorption edge in the X-ray energy shown in the figure and Filter 2, composed of elements where the absorption edge is virtually in the center of the horizontal axis

elements like silver or tin, which have an atomic number of approximately 40 or above and an absorption edge at an X-ray energy of several dozens of keV, are not suitable as a filter, depending on the experimental conditions.

As shown in Figs. 4.2 and 4.18, X-ray tubes have characteristic X-ray spectra depending on the target material, tube voltage, and target angle. The filter material and

thickness are selected by considering the energy range of the X-rays to be attenuated. For example, suppose that aluminum, titanium, copper, and niobium were four metal types used as a filter. Their atomic numbers vary widely from 13 to 41 and, as seen in Chap. 2, their X-ray attenuation behavior can vary widely. Nickoloff et al. reported that when tungsten was used as a target at an 80-kV tube voltage (target angle was 12°) and when the filter thickness was adjusted so that these all took the same peak X-ray energy (48.0 keV), the thickness values were 4.1, 0.50, 0.11, and 0.05 mm, respectively [54]. Assessments on beam intensities in these cases showed results of 58.0, 65.6, 66.8, and 65.3% of the non-filtered cases, respectively [54]. Virtually identical X-ray spectra were obtained regardless of the filter when these were adjusted with tube current [54].

An optimal filter thickness can be calculated for medical-use X-ray CT scanners when considering patient exposure (particularly X-ray absorption near the skin) and tube load by considering the X-ray spectra obtained in this way [54]. However, sample exposure is typically not an issue with industrial-use CT scanners, so these types of discussions are not applicable. Thus, for cases where the X-ray tube spectra used in the X-ray CT scanners are determined by the user and the sample cross-section morphology is simple, filters can be selected simply by considering the X-ray energy dependencies of the linear absorption coefficients, as shown in Chap. 2. Figure 4.55 shows the X-ray spectra adjusted by X-ray tube voltage and the filter so that a polymer, aluminum, and steel disk sample with 1-mm diameter can be effectively imaged using a commercially available microfocus tube. Suitable filters are often selected by actually imaging a sample and confirming the quality of 3D images in cases where the X-ray spectra specifications are unknown for the X-ray CT scanner used.

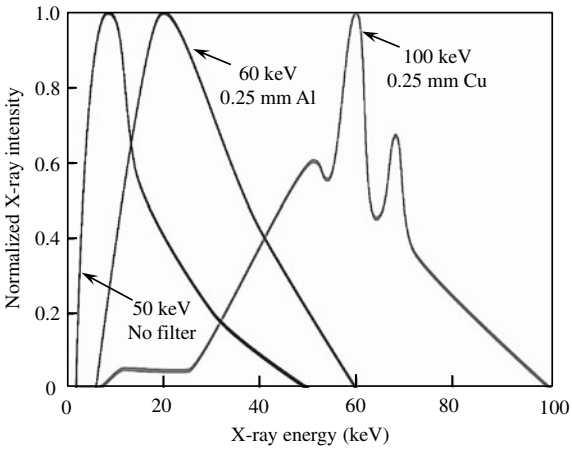

Fig. 4.55 Schematic of X-ray spectra where a single microfocus tube was used and where adjustments in the tube voltage and filter were made to adjust to the X-ray spectra matching a polymer, aluminum alloy, and steel. The vertical axis shows normalized X-ray intensity

4.3 Positioning Stage

At the very least, an X-ray CT scanner must fundamentally have its X-ray source, sample rotation stage, and detector perfectly aligned in the vertical and horizontal directions. Furthermore, when using various slits, zone plates, condenser plates, phase plates, etc., these must be accurately positioned with the detector and sample rotation stage as well. To achieve this, a sample rotation stage, *XY linear stage*, *slider module*, and a *goniometric stage* must be used as required. Examples of these are shown in Fig. 4.56. Synchrotron radiation X-ray tomography in particular requires many combinations of these due to the multiple uses of the experimental hutch and diversity of user experiment. Of these, the sample rotation stage directly affects the spatial resolution of the obtained 3D images and is related to artifact generation.

As discussed later in Eqs. (5.29) and (7.30), among the various factors in X-ray tomography—the effective focal spot size of the radiation source, the Nyquist frequency stipulated by the rotation step and the pixel size of the detector, the positional accuracy of the sample rotation stage, sample drift, and the detector—the single factor with the lowest accuracy acts as the rate-determining step that stipulates the spatial resolution. Of these, Sect. 4.1 discusses the X-ray source and Chap. 7

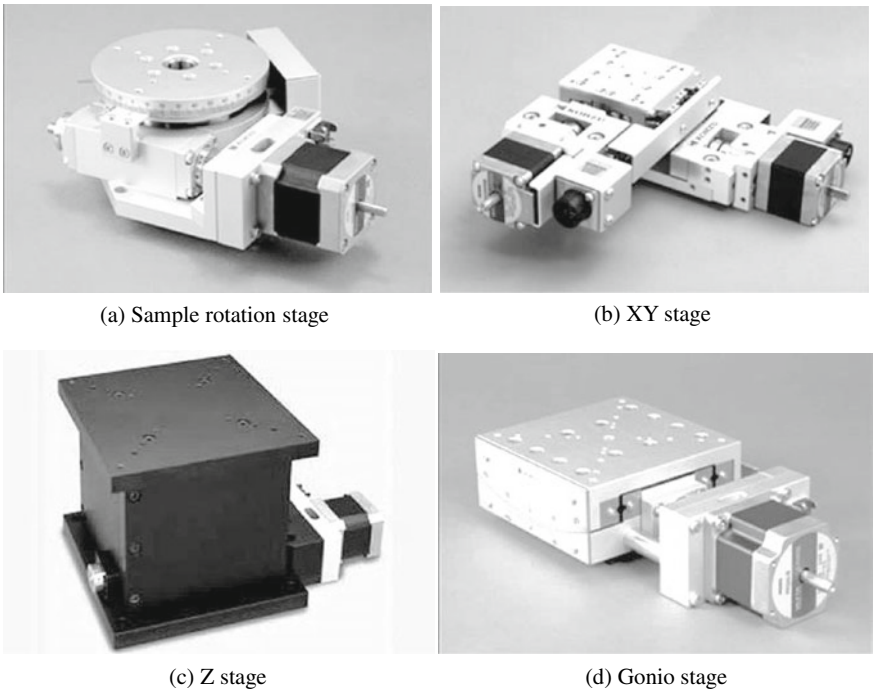

(a) Sample rotation stage (b) XY stage

(c) Z stage (d) Gonio stage

Fig. 4.56 Various stages used in X-ray CT scanners (courtesy of Masamichi Kojima of Kohzu Precision Co., Ltd.)

discusses the Nyquist frequency. The remaining factors of positional accuracy of the sample rotation stage and sample drift are particularly important for high-resolution imaging and synchrotron radiation X-ray tomography. Furthermore, sample rotation stage accuracy is presumed to lower the spatial resolution even in the case of standard industrial X-ray CT scanners if the spatial resolution measured in 3D images cannot be explained by the effective focal spot size of the X-ray source or the Nyquist frequency.

4.3.1 Sample Rotation Stage

Although there are components without which an X-ray CT scanner cannot function, it is perhaps the sample rotation stage whose importance remains most unrecognized. An X-ray CT scanner requires a *thrust bearing* that can rotate a sample while withstanding the sample weight; *ball bearings* are primarily used. *Air bearings* and *slide guides*, the latter of which operates on a sliding bearing, may be used depending on the desired accuracy if a higher spatial resolution is desired. Figure 4.57 shows a schematic of each mechanism.

A general-use rotation stage with a ball bearing is typically used for industrial X-ray CT scanners, even for microtomography setups. These cases usually use a 5-cm diameter sample rotation stage with a *load capacity* of 2–3 kgf, *eccentricity* of 5 μm, and *surface runout* of approximately 20 μm; alternatively using a 20-cm diameter sample rotation stage with a load capacity of 30 kgf, eccentricity of 10 μm, and surface runout of approximately 20 μm. Furthermore, diameters of 7–10 cm are presumed to yield the highest accuracies, where eccentricities of up to 0.5 μm can be used. From Table 6.1 shown later, commercially-available high-resolution X-ray CT scanners use rotation stages with a load capacity of 2–12 kgf. Discussions with the manufacturer are particularly important for high-precision sample rotation stages, as performance varies for each individual rotation stage. Here, eccentricity is the runout in the rotation radius direction and surface runout is the angle runout in the plane normal to the rotation axis. Photographs depicting the actual measurement of eccentricity and surface runout are shown in Fig. 4.58. Methods stipulated by JIS involve contact- or non-contact-type measurement methods where a true sphere is placed on the stage. The measured rotation errors such as for eccentricity and surface runout are the result of superpositions of displacements in the radius direction and axial direction (i.e. vertical direction), shifts in centering, and angle fluctuations in the rotation axis due to the *motion of precession*. What is important for X-ray tomography is not the upper surface of the stage but the vertical and horizontal fluctuations at sample positions located several dozen cm at maximum in the vertical direction from the upper stage surface. Thus, care must be taken so that effects on spatial resolution cannot be directly determined simply from the specifications of sample rotation stages like those shown above. Furthermore, accuracy is thought to further worsen in cases of laminography where the rotation stage is inclined.

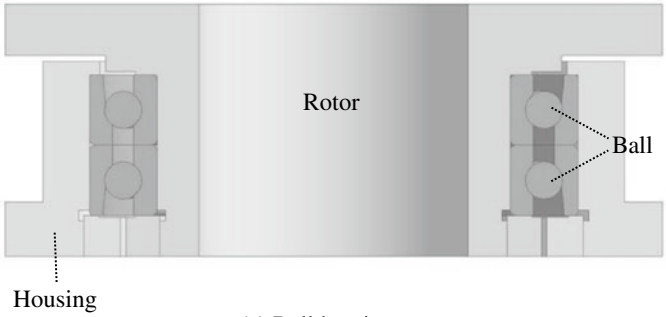

(a) Ball bearing type

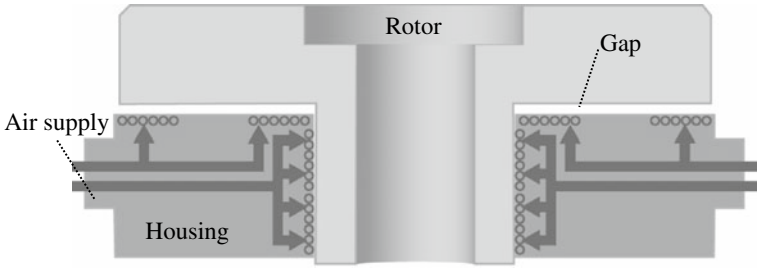

(b) Sliding bearing type (Air bearing)

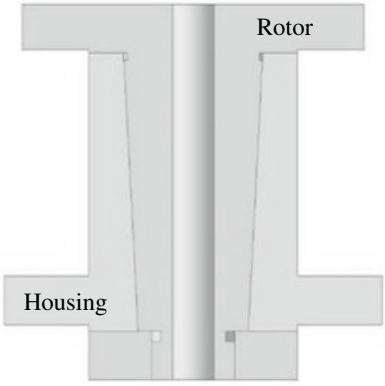

(c) Sliding bearing type (Slide guide)

Fig. 4.57 Various rotation stages used in X-ray CT scanners (courtesy of Masamichi Kojima of Kohzu Precision Co., Ltd.)

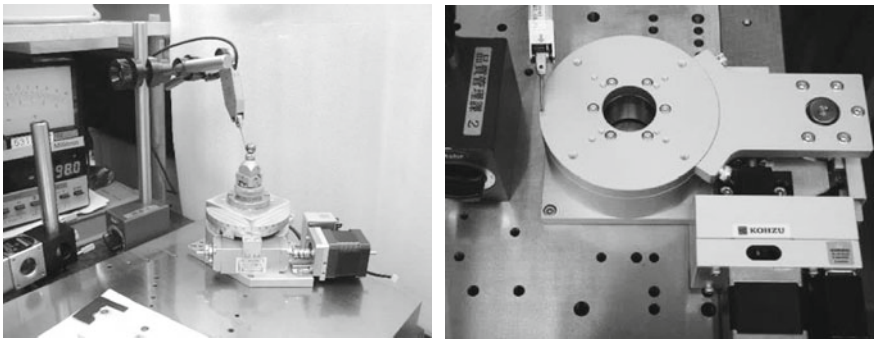

(a) Eccentricity (b) Surface runout

Fig. 4.58 Measurement examples of eccentricity and surface runout of the rotation stage used in the X-ray CT scanner (courtesy of Masamichi Kojima of Kohzu Precision Co., Ltd.)

A stage rotation speed of 0.2 rotations/s is considered the limit for a standard *worm-gear type* (combination of a worm shaft and worm gear) shown in Fig. 4.59a. A sample rotation stage may at times need to be rotated at faster speeds in cases of fast tomography using synchrotron radiation. For these types of cases, rotation speeds of 2 rotations/s and 5 rotations/s can be achieved with a *belt-drive type* (Fig. 4.59b) and *direct-drive type* (Fig. 4.59c), respectively. Equipment selection alone is insufficient for high-accuracy rapid rotation and ensuring that the sample's center of gravity is accurately placed on the rotational axis.

The eccentricity can be controlled to 100–200 nm when the sample rotation stage is an air-bearing type (referred to as an *air spindle* when seen as a rotation unit) such as shown in Fig. 4.57b, with a maximum load capacity of approximately 10 kg and a maximum diameter of approximately 20 cm. Generally, when using fluid lubrication (e.g. sliding bearing), the fluid viscosity is proportional to the friction coefficient. The air viscosity is three orders of magnitude smaller than the lubricant oil, so the air bearing type has less friction loss and heat generation, making it suitable for faster speeds. It also has the advantage of working well in clean environments or high temperatures. Meanwhile, a clean dry air must be stably supplied at a fixed pressure of approximately 0.5 MPa. Care must be taken, as the actual eccentricity accuracy of the air spindle is strongly dependent on the stability of the supplied air pressure and temperature. Meanwhile, a slide guide type as shown in Fig. 4.57c has its load capacity-controlled to approximately 2 kgf (20 cm in diameter) but a relatively low-cost and compact yet high-accuracy sample rotation can be obtained as a result. A maximum eccentricity of approximately 70 nm (up to 200 nm) can be achieved. However, it is essential that lubricant oil enters the gaps and forms an oil film. The rotation stage will be scorched without a gap, so maintenance is necessary to ensure that the lubricant oil does not run out. Care must be taken particularly in synchrotron radiation experiments where non-use periods are extensive.

Active eccentricity/surface runout control techniques are necessary when further rotation accuracy is needed; for example, when a sub-micron spatial accuracy is

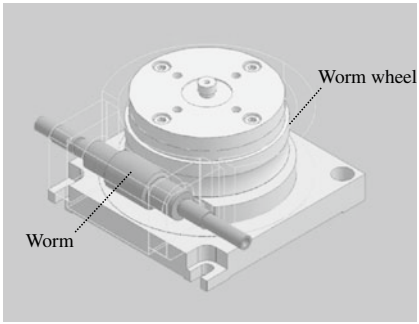

(a) Worm gear type

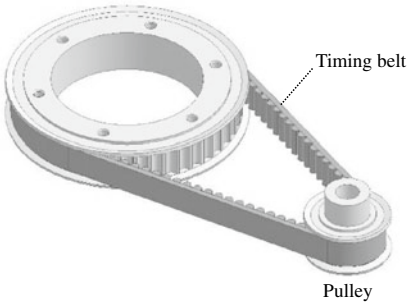

(b) Belt drive type

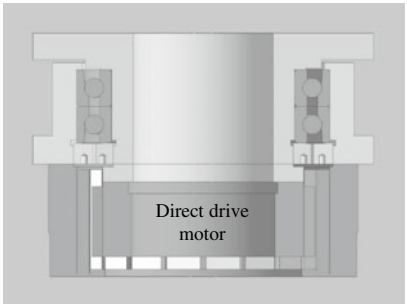

(c) Direct drive type

Fig. 4.59 Various rotation mechanisms used in X-ray CT scanner (courtesy of Masamichi Kojima of Kohzu Precision Co., Ltd.)

needed for synchrotron radiation X-ray tomography [55]. For example, there are application reports at the synchrotron radiation facility SOLEIL, near the suburbs of Paris, in France [56]. Here, the eccentricity and surface runout characteristics unique to the sample rotation stage used were measured beforehand to conduct corrections with feed-forward controls with an XY stage. Interferometers were used during imaging as well to measure eccentricity and surface runout and additional corrections were conducted using feedback controls [55].

The helical-scan type X-ray CT scanners of the sixth-generation CT introduced in Chap. 3 has a *slip ring* mechanism installed, which allows for continuous rotation in a single direction by supplying power and transferring data to the X-ray tube and detector attached to the gantry. A slip ring is also used for high-speed tomography discussed in Sect. 5.3, because the rotation stage is continuously rotated multiple times while keeping its test rigs for in situ observation (discussed later in Sect. 4.5) and heating furnace on the rotation stage. Conducting metal disks made of copper are stacked and fixed by the number of necessary channels in the slip ring, so each disk is in constant contact with separate brushes even during rotation. This can be used to conduct power voltage and data signal exchange without connecting the top and bottom of the rotation stage with cables.

4.3.2 Other Positioning Stages

The number of strokes is the only issue when using an XY-stage as shown in Fig. 4.56b or *Z-stage* as shown in Fig. 4.56c for industrial X-ray CT scanners. However, the main rotation stage body rotates at an inclined position relative to the incident X-ray in laminography, so care must be taken to ensure that the XY-stage is not detached. Magnets are occasionally used to keep this fixed. The sample is sometimes removed from the field-of-view and an I_0 image (Eqs. (2.2) and (3.1)) is acquired in synchrotron radiation X-ray tomography. An issue that arises in these cases is the reproducibility of the positioning when the XY stage returns. This has been stipulated by JIS as repeated positioning accuracy and its specifications are indicated in their catalog. Reproducibility is primarily influenced by the heat generation of the motor. For this reason, countermeasures such as including heat insulation in the rotation stage or sufficiently moving it beforehand and using it when temperature fluctuations are low, have been used.

A gonio stage, as shown in Fig. 4.56d, must be used to carefully adjust the alignment of the detector and rotation axis of the sample rotation stage when conducting synchrotron radiation X-ray tomography, where the detector is frequently taken on and off. The gonio stage can conduct micro-adjustments in the tilt angle of the detector in a range of around $\pm 10°$ by moving the upper gonio stage surface along an arc in which the center of rotation is a point well above the stage. The detector shifts significantly in the vertical and horizontal directions simultaneously with this adjustment, so coordination with the XY stage is essential.

4.4 Detector

Within the history of X-ray tomography, detectors have shown more rapid progress than the introduced X-ray sources and positioning stages, with many existing variations. With this in mind, an overview will be presented on a limited number of detectors that are in frequent use today. For example, *imaging plates*, which use ion crystals that exhibit photostimulated luminescence, have been omitted from the following discussion. Figure 4.60 shows the types of detectors used in the primary commercially-available industrial X-ray CT scanners and their relationship with maximum tube voltage. Detectors can be classified between a *charge-coupled device* (*CCD*), *flat panel detector* (*FPD*), *image intensifier* (*II*), and *line sensor camera*. Except for line sensor cameras, all of these are two-dimensional detectors that can directly capture two-dimensional information as is shown in Fig. 3.4. Meanwhile, the line sensor camera is a linear or curved one-dimensional detector similar to those shown in Figs. 3.1 or 3.2c. As shown in Fig. 4.60, line sensors are frequently used when the tube voltage is over 450 kV. Furthermore, the FPD or image intensifier is used up to a tube voltage of approximately 300 kV. Furthermore, a CCD camera is

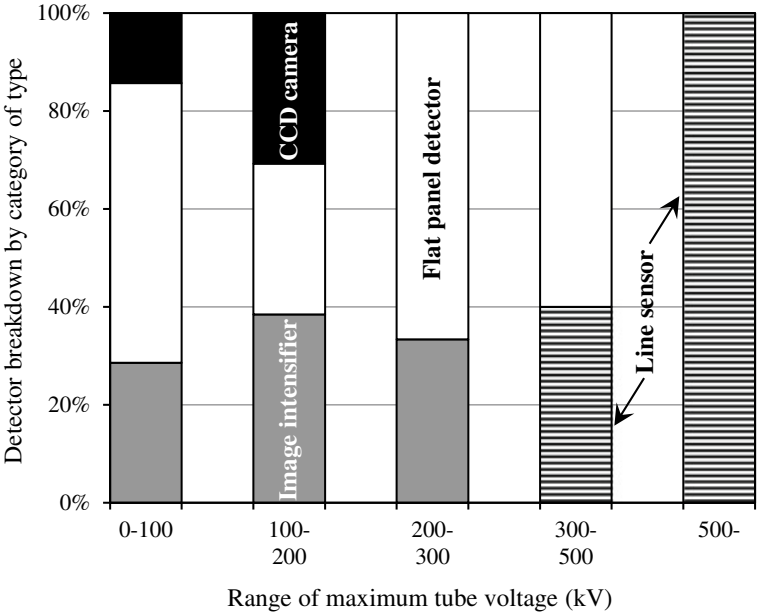

Fig. 4.60 Maximum tube voltage and type of detector used in commercially available industrial-use X-ray CT scanners as of the fall 2017

used when observing small samples with a low tube voltage. *Complementary metal-oxide-semiconductor* (*CMOS*) cameras have recently been used in place of CCD cameras in synchrotron radiation facilities. The use of CMOS cameras, in industrial X-ray CT scanners and elsewhere, is expected to increase in the future.

This section first provides an overview of the important indicators required for assessing the performance of each detector, after which each detector is investigated in further detail.

4.4.1 Characteristic Assessment of Detectors

X-ray intensity measurements involve factors like *gain*, *quantum efficiency* (*QE*), *noise*, *dynamic range*, and *linearity*. The detectable X-ray energy range is then determined from combinations with a scintillator, which determines the overall efficiency of the detector system. This is described in the scintillator section. Furthermore, the pixel number and size of the detector influence the sample size that can be covered by X-ray imaging and the achievable effective spatial resolution through a combination with the glass fibers and the optical lens, which magnify or demagnify the image after converting it to visible light. Meanwhile, *temporal resolution* is determined from the *frame rate* of the detector and the *decay time* of the scintillator.

(1) Gain

Gain is also referred to as the *conversion ratio* or *sensitivity*. The photons, which enter the detector are accumulated within the detector after being converted to a charge, are further converted to voltage levels through the readout pathway and ultimately outputted after AD conversion. The detector gain is stipulated by the ratio between the charge number per pixel and the pixel output signal, expressed by the *digital number* (*DN*) or *analog-to-digital unit* (*ADU*). A single photon corresponds to a single charge in the former for standard CCD cameras, with the exception of EM-CCD cameras. The latter is in units of count number. Both have a linear relationship and multiplying the gain to ADU yields the measured photon number. The gain is dependent on both the quantum efficiency of the element and the electron-to-voltage conversion efficiency. The latter is dependent on the capacitance and gain of the output amplifier. A higher gain generally increases the dynamic range as well as noise, so the gain must be set to balance the two.

Gain heterogeneity is referred to as *shading*, with areas where the image brightness is not uniform and dark areas appear across wide ranges. This can be corrected using calibration data prepared in advance.

(2) Quantum Efficiency

Quantum efficiency is defined as the number of photon charges accumulated at the detector divided by incident photons. This naturally takes a value less than one and values closer to one are considered superior. Quantum efficiency can be estimated by considering the material used for detection, but this cannot be directly measured for individual detectors. Furthermore, quantum efficiency does not consider image information deterioration such as increased noise based on signal processing within the detector interior. Figure 4.61 shows the quantum efficiency of two CCD cameras: the Hamamatsu Photonics C4880-41S camera (4000 × 2624 pixels, pixel size 5.9 μm, back-side illuminated type) and the ESRF FreLoN 2000 camera [57]. The former has a maximum quantum efficiency of approximately 50% when the incident ray is 460 nm (blue) and over 40% when between 420–550 nm. The latter has high quantum efficiency in the 500–800-nm range (green–red). In this manner, the quantum efficiency of the detector has a visible light wavelength dependency and the scintillator is selected with this in mind. Quantum efficiency in front-side illuminated type CCD cameras decreases when the transparent electron acts as an optical filter, whereas a back-side illuminated type exhibits high quantum efficiency across a wide wavelength range. The detector mechanism thus affects quantum efficiency in this manner.

Incidentally, a *detective quantum efficiency* (*DQE*) is used as a practical indicator for assessing the differences in image quality for each detector, which is expressed through directly measurable quantities. The DQE is expressed as follows [58]:

$$DQE = \frac{(SNR_{\text{out}})^2}{(SNR_{\text{in}})^2} \tag{4.38}$$

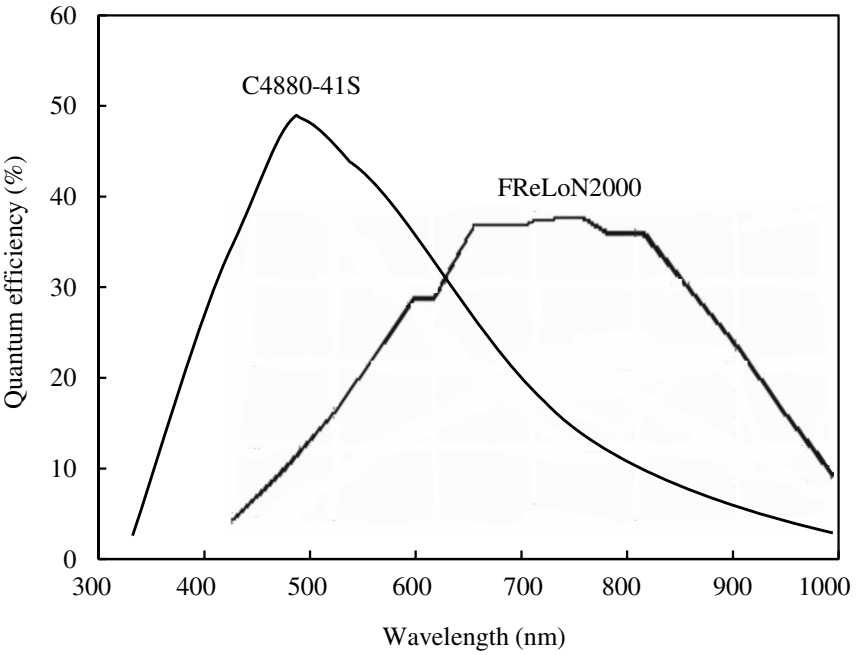

Fig. 4.61 Example of quantum efficiencies in a CCD camera [57]

Here, SNR_{in} and SNR_{out} refer to the S/N ratios of the input and output image, respectively. Setting the input/output signals as S_{in} and S_{out} and input/output noise as N_{in} and N_{out} yields $SNR_{\text{in}} = S_{\text{in}}/N_{\text{in}}$ and $SNR_{\text{out}} = S_{\text{out}}/N_{\text{out}}$. The DQE, in an ideal detector without any noise, is equal to the quantum efficiency. SNR_{in}^2 increases linearly with incident photon flux. The input noise relating to this is the *photon noise* (also referred to as *quantum noise* or *shot noise*). This is due to the random fluctuations centering on the average value seen in the photon flux. SNR_{in} can be improved by adjusting the imaging conditions, such as increasing the exposure time. However, N_{in} cannot be eliminated; in other words, photon noise is an unavoidable form of noise. In general, X-ray intensity fluctuations follow *Poisson statistics*. The square root of the average parameter value is equal to the standard deviation when a given data set follows Poisson statistics. For this reason, the photon noise corresponding to the standard deviation of image signals can be expressed as proportional to the square root of the X-ray photon number.

$$\sqrt{S_{in}} = N_{in} \tag{4.39}$$

Figure 4.62 shows the relationship between the input signal and photon noise. *Secondary quantum noise*, which is generated through a fluorescence emission process, and *excess noise*, which is produced through scattering in X-ray photon absorption processes, similarly satisfy Eq. (4.39) in addition to photon noise.

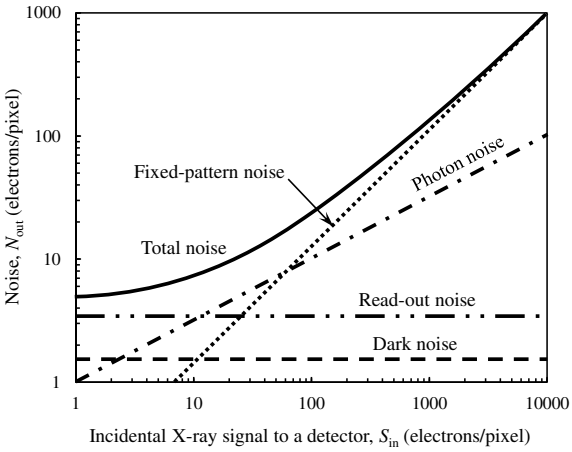

Fig. 4.62 Schematic showing the relationship between different types of noise and the intensity of an X-ray incident to the detector

If gain is defined as $G = S_{out}/S_{in}$, Eq. (4.38) can be re-written as follows [59]:

$$DQE = \frac{GS_{out}}{(N_{out})^2} \tag{4.40}$$

The right-hand side of Eq. (4.39) is the output signal, output image noise, and detector gain, where each is a measurable amount. These can be used to quantitatively compare the performance of detectors of otherwise different types. The ideal detector is $DQE = 1$.

(3) Full Well Capacity and Dynamic Range

Full well capacity is the amount of charge that saturates each pixel. Dynamic range is defined as the ratio between the maximum image signal level where linearity can be maintained without saturation and the minimum detectable signal level; the former is stipulated by the full well capacity and the latter is substantially defined by background noise levels. The dynamic range is generally expressed in units of bits. For example, a dynamic range of 10,000 is expressed as $\log_2(10{,}000) = 13.3$ (bits).

The full well capacity varies according to detector pixel size or operating voltage. A saturated charge in a pixel results in a loss of linearity and quantitative characteristics, as well as a phenomenon referred to as *blooming*, where the charge leaks out into adjacent pixels and influences the measured values in those pixels. A larger pixel size reduces spatial resolution but also increases full well capacity and dynamic range. Even extremely large differences in local X-ray absorption within a sample can be effectively distinguished when using a high-dynamic-range detector. Furthermore, quantitative measurements can be assured. As such, dynamic range is an important detector characteristic alongside sensitivity and spatial resolution.

Using a CCD camera as an example, converting X-rays into visible light and emitting them toward a camera is more effective in obtaining a high dynamic range than

directly emitting X-rays to the CCD camera. An X-ray with an energy of 10 keV generates approximately 3000 electron-hole pairs when X-rays are directly incident to the CCD camera. The dynamic range is approximately 30–300, based on the capacity of the *electron-hole pairs*, which can be accumulated in each pixel (100,000–1,000,000) [60]. Converting these to visible light and then emitting them to the CCD camera produces several electron-hole pairs for each X-ray photon and a dynamic range that encompasses 4–5 orders of magnitude can be obtained if a suitable scintillator and transfer system are selected [60]. For this reason, images should generally be formed in a CCD camera using fiber optic taper for demagnification or an optical lens after using a scintillator to convert X-rays to visible light [60].

(4) Noise

Photon noise is the only form of noise that affects the S/N ratio on the input side. However, other noise types in the image output from the detector include *readout noise*, *dark noise*, and *fixed-pattern noise*.

Fixed-pattern noise is caused by the scintillator microstructure, microdefects or thickness irregularities, variations in transmission capability of each optical fiber, and sensitivity irregularities in each pixel. The extent of fixed-pattern noise is presumed to be proportional to the input signal level, as shown in Fig. 4.62. Fixed-pattern noise has a spatial distribution but no temporal variability, therefore, it can be removed with *flat-field image correction*. In this case, a high-accuracy pixel-based correction is possible by taking multiple images based on homogeneous incident radiation without the sample and averaging these images.

Furthermore, *calculation noise*, described earlier in Sect. 3.3.4 (1), also occurs during the reconstruction process. Furthermore, *aliasing noise*, which occurs in images with frequency components exceeding the Nyquist frequency that stipulates the sampling theorem described in Chap. 7, can be an issue under certain conditions. These types of noise appear after the data output from the camera is reconstructed.

Incidentally, N_r and N_d are each defined as the readout noise and dark noise, F (photons/pixel/s) as the photon flux, τ (s) as the exposure time, η_q as the quantum efficiency of the detector, and i_d as the *dark current*. The photon number N is expressed as $F_{\tau\eta_\mathrm{q}}$. The total noise N_t is expressed by Eq. (4.41) [57].

$$N_t = \sqrt{N + N_d^2 + N_r^2} = \sqrt{F\eta_q\tau + i_d\tau + N_r^2} \tag{4.41}$$

From Eq. (4.41), contributions of the readout noise become relatively large under insufficient quantities of light. This is clear even with the relationship between noise and signal, shown in Fig. 4.62. Furthermore, the S/N ratio of the image is expressed with Eq. (4.42) [57].

$$SNR_{out} = \frac{F\eta\tau}{\sqrt{F\eta_q\tau + i_d\tau + N_r^2}} \tag{4.42}$$

The S/N ratio greatly decreases with larger readout noise under insufficient quantities of light. Equation (4.42) demonstrates that increases in photon flux and exposure time in these cases can have an equivalent effect. Detectors with superior S/N ratios have low readout noise and dark current.

The readout noise is electric noise generated by signal transmission, amplifier circuits, and electronic circuits such as switches. This is observed even under short exposure times where dark noise is not prominent. For this reason, its influence is particularly large under low-exposure conditions. This amount varies depending on the detector output type. Furthermore, although this does not vary with exposure amount, as in Fig. 4.62, there is a frequency dependency. With a CCD camera, for example, a higher readout frequency results in rapidly increased readout noise.

Meanwhile, dark noise occurs when valence band electrons are thermally excited within the interior of materials with a narrow energy band gap such as silicon. The abundance of dark currents is heterogeneous and induces fixed pattern noise. Furthermore, they can appear as random noise due to temporal variations. Dark noise is proportional to the square root of dark current. Furthermore, dark current is dependent on temperature as shown in the following equation:

$$i_d = CT^{3/2}e^{-E_g/2kT} \tag{4.43}$$

Here, C is a constant relating to the light-receiving area of the pixel and E_g is the energy band gap. We can see from this equation that the dark current decreases by approximately 1/2 for every 7° drop in temperature. For this reason, elements are sometimes cooled with a *Peltier device* to reduce the dark current. In practice, the Hamamatsu Photonics C4880-41S camera used in SPring-8 and shown in Fig. 4.61 controls its dark noise to approximately 1 e^-/s by cooling it to approximately −50 °C with a Peltier device. However, condensation countermeasures are also necessary for detector cooling. Although this is also dependent on exposure time, dark noise at about room temperature is typically predominant with regard to the minimum detectable signal level, which stipulates the lower limit of dynamic range. Readout noise becomes predominant when the element is cooled to a point where dark noise is negligible.

Figure 4.63 shows a noisy image undergoing *averaging* across 20 continuous images. This is a transmission image of an aluminum alloy microstructure that was obtained with a deliberately poor image quality by reducing the exposure time to a level considerably below normal. The specimen thickness and X-ray energy, in this case, were 600 μm and 20 keV, respectively. Averaging a noisy image can significantly improve the image quality from the perspective of the noise's statistical nature.

Incidentally, *binning treatment* (additive treatment of multiple pixels) can improve the photon count per pixel and sensitivity. At the same time, it can also decrease the readout frequency, which decreases the readout noise and improves the frame rate. This treatment is commonly expressed by labels such as 2 × 2; this indicates the addition of four pixels in the horizontal and vertical directions.

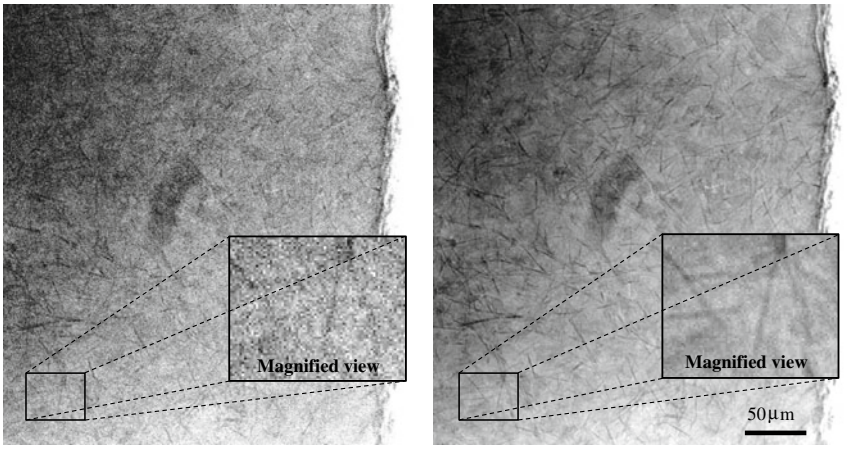

(a) Projection image (b) After averaging 20 projection images

Fig. 4.63 Transmission image of an Al-7% Si cast alloy obtained at SPring-8. The exposure time was minimized, and an image with a deliberately poor S/N ratio is shown in (**a**). This was imaged 20 consecutive times and the averaged result is shown in (**b**). The silicon and intermetallic compounds including iron are clearly visualized in (**b**)

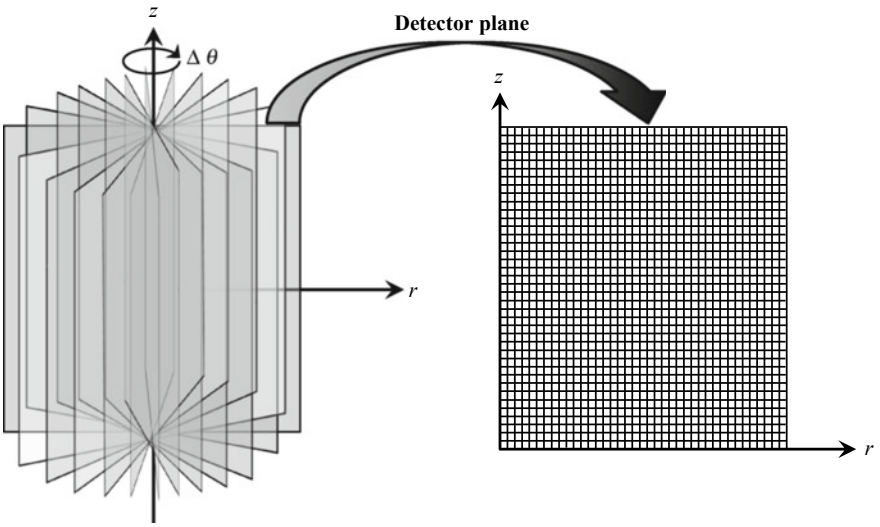

Fig. 4.64 Single set of projection data obtained by using a parallel beam, rotating the sample 180º and displaying it in Radon space

(5) Pixel

As shown in Fig. 4.64, the vertical and horizontal pixel sizes within a detector plane when a two-dimensional detector is used stipulate the sampling pitch, which in turn

determines the spatial resolution. The images obtained from two-dimensional detectors are 3D, hence, the last remaining direction is determined from the *rotation pitch* ($\Delta\theta$) of the rotation stage. The effective element size is determined by multiplying the pixel size with the *pixel number*. The detector combines glass fibers and an optical lens, which magnify or demagnify an image after visible light conversion; hence, the field of view in the detection system considers the magnification or demagnification.

Meanwhile, as shown in Fig. 4.65, the percentage of effective-use area, where areas for charge readout wires in the light-receiving area are removed, in a single-pixel area is referred to as the *fill factor*. Even in CMOS cameras, the fill factor can go as high as 90%. Although CCD cameras vary widely according to their mechanism, those with a 100% fill factor are commercially available. The fill factor is important as it determines X-ray detection efficiency.

(6) Frame Rate and Dead Time

As shown in Fig. 4.66, the frame rate is the inverse of a single cycle time T_c, which includes the *exposure time* T_e, read out time T_r, and *dead time*. Naturally, the single

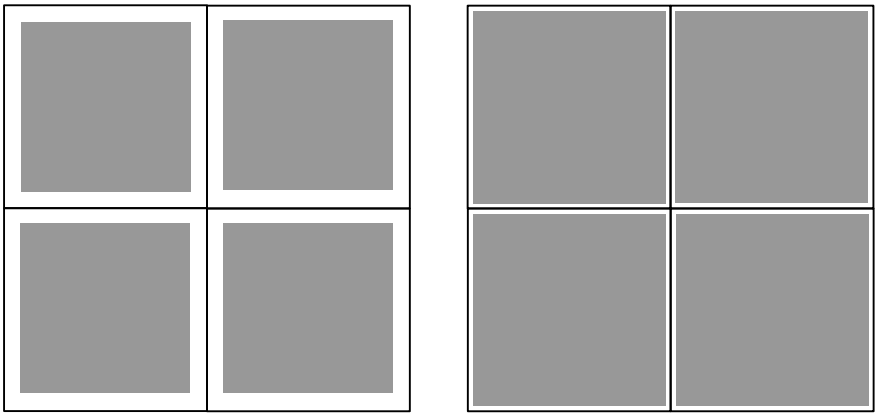

(a) Detector of 70% fill factor (b) Detector of 90% fill factor

Fig. 4.65 Fill factors of detectors

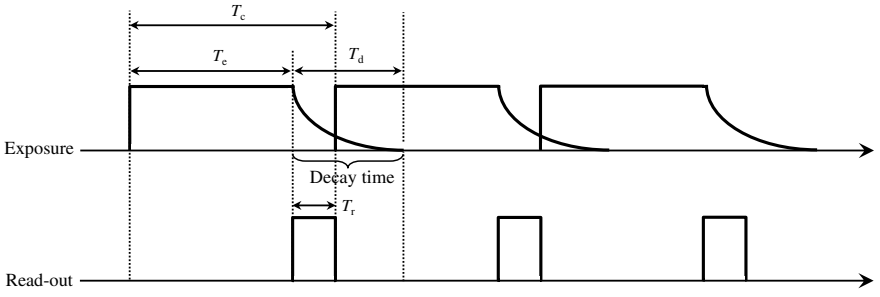

Fig. 4.66 Cycle time and frame rate of the detector

cycle time is not a simple addition in cases where the exposure and readout can be conducted in parallel. The frame rate is expressed in units of frames per second (fps). Furthermore, the T_d in the figure is the decay time of the scintillator. Other than this, a single cycle time in actual practice depends on the detector used but also includes the time required for clearing the accumulated charge, as well as the time required for opening and closing the shutter. It also significantly depends on the imaging mode, such as with binning treatment or imaging regions of interest. The frame rate, which is the specification of the detector, is the value under standard exposure conditions and care must be taken for the frame rate value when the exposure time is zero as it may at times be used.

4.4.2 Various Detectors

(1) Line Sensor Camera

The line sensor camera is an important detector, which has supported the development of medical-use X-ray CT scanners. Even today, it is widely used in non-destructive observations and the detection of foreign objects (e.g. detection of foreign bodies in food products, medical products, and electronic components transported on a belt conveyor, as well as hand-luggage detection at airports). Figure 4.67 shows an example of a commercially-available line sensor camera.

As shown in Fig. 4.68, combinations of scintillators (e.g. GOS:Tb, CsI:Tl, CWO), and *photodiodes* (Fig. 4.68a) or semiconducting detectors (Fig. 4.68b) have been used as line sensor cameras. Visible light generated in the scintillator of the former is radiated in all directions. For this reason, even if the visible light was effectively guided with light-reflective materials or *structured scintillators*, only a tiny portion of the generated light would be detected at the photodiode. Silicon, with high sensitivity

Fig. 4.67 Examples of commercially available line sensors; **a** Hamamatsu Photonics C9750 series (courtesy of Hamamatsu Photonics) and **b** X-SCAN XIH8800 (courtesy of Mr. Tsuchiya from Ad Science)

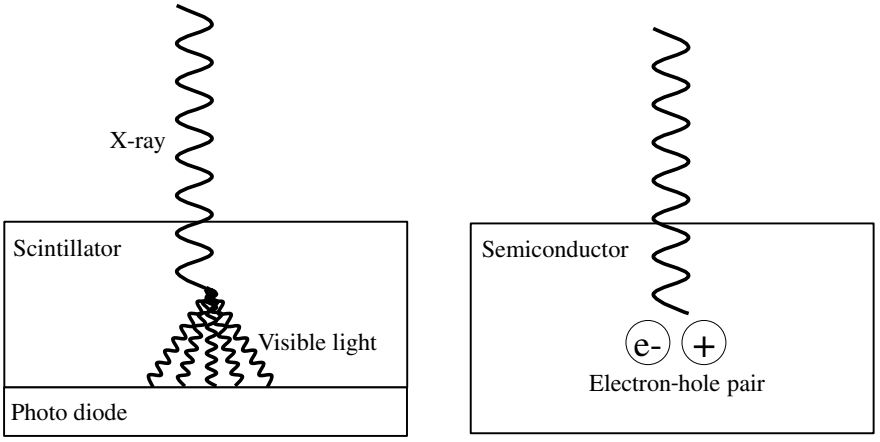

(a) Scintillator type (b) Semiconductor type

Fig. 4.68 Line sensor camera unit. A line sensor camera is composed of these units arranged in a linear fashion

for high-energy X-rays, has been used for the latter. CdTe and CdZnTe have also been used in recent years for *photon counting* purposes (discussed later). Approximately 500 to 1000 detection units such as those in Fig. 4.68 are generally arranged one-dimensionally at a fixed interval in line sensor cameras. Two-dimensional images must be obtained from one-dimensional images taken continuously while moving the sample in the rotational axis direction of the sample rotation stage to obtain 3D images with a line sensor camera. The X-ray is narrowed into a fan-beam shape using a collimator as shown in Fig. 4.69b to make it incident to the sample such that the field-of-view alone of the line sensor camera is incident to the sample. As shown in Fig. 4.69a, scattered X-rays are incident to the pixels in the detector from all locations on the sample because of forward-scattering of high-energy X-rays in the case of a parallel or cone beam. This can be limited to scattering from the width direction in the case of a fan beam in Fig. 4.69b. As a result, forward-scattering-induced decreases in both contrast and spatial resolution can be effectively prevented.

Time delay integration- (*TDI*) and *dual energy*-types exist as variations of X-ray line sensor cameras. There are multiple (typically 128) rows unlike the single detector element row for the former. Arithmetic means from multiple rows enable images to be obtained with a high S/N ratio [61]. Detector elements are in two stages in the X-ray propagation direction for the latter, with the first and second stages detecting X-rays with low and high energies, respectively [61]. The constituent elements of materials can be identified with this type.

(2) Image Intensifier

An image intensifier has high sensitivity due to its electron multiplication mechanism. It was historically developed for military purposes with regard to night vision under

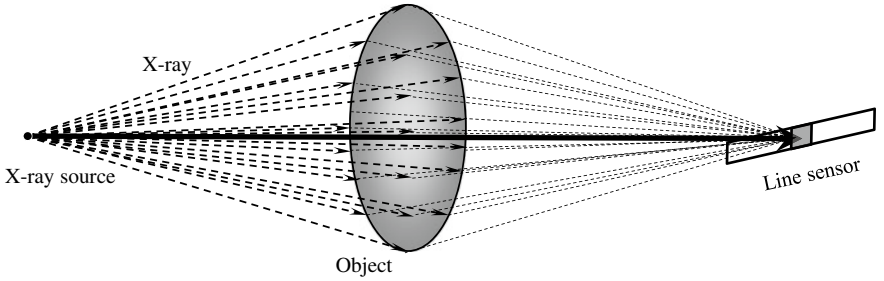

(a) Cone beam

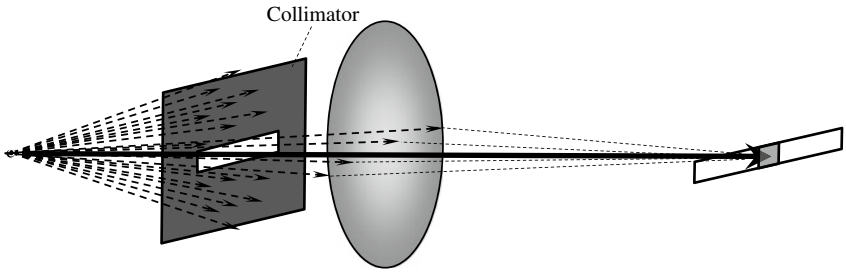

(b) Fan beam

Fig. 4.69 Schematic comparing the extent of forward-scattering due to high-energy X-rays when imaging with a line sensor and either a cone beam or fan beam. The number of scattered X-rays incident to specific pixels of the line sensor is evident

starlight or moonlight. It is typically classified between first–third generation devices, depending on its structure or the material used.

First-generation image intensifiers are a *photomultiplier tube*-type, which has a structure as is shown in Fig. 4.70a. In order from the input side, they are composed of an incidence window, a fluorescent screen on the input side, a *photocathode*, a focusing electrode, anode, a fluorescent screen on the output side, a coupling lens, and a visible light detector (a CCD camera is primarily used). Materials like aluminum are used for casing and its interior is maintained in a vacuum. X-rays are first converted to visible light with fluorescent screens made of CsI columnar crystals, which exhibit an optical fiber-like structure. Next, the visible light is converted to electrons with a *photoelectric surface* (e.g. Sb_2Cs_3) in the vacuum side. The spectra of the generated visible light, in this case, must be matched with the *spectral sensitivity* (the relationship between quantum efficiency and wavelength) of the photoelectric surface. The electron is focused and accelerated through an electron lens due to an electric field generated by voltage differences of several dozens of kV; the electron then collides with a thin and fine fluorescent screen (e.g. ZnCdS:Ag or ZnS:Cu,Al) on the output side. The accelerated electron generates multiple photons as a result. The material on the incident window is aluminum, but a beryllium window is preferred instead when a low-energy X-ray is used.

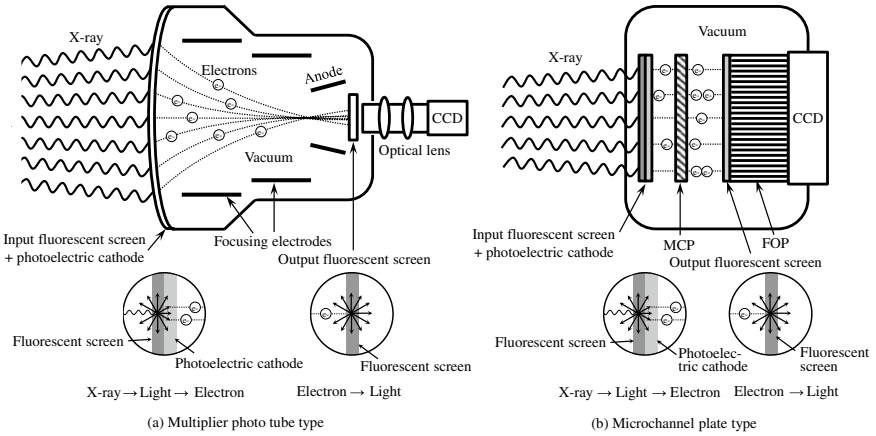

Fig. 4.70 Schematic showing a representative image intensifier structure

The incident window is spherical as the interior is in a vacuum, which results in shading wherein the center is bright and the periphery is dark [61]. Additional disadvantages include image distortion with a closer distance to the outer edge and *halation* caused by charge saturation of the CCD camera [61]. Flat-panel sensitivity has increased in recent years, and devices with larger diameters can be used; therefore, flat panel detectors have been exchanged with image intensifiers.

The gain of first-generation image intensifiers is determined from the *flux gain* due to electron acceleration and *minification gain* due to focusing. The former is defined as the number of photons generated in a fluorescent screen on the output side per unit photon generated in the fluorescent screen on the input side. This has a typical value of approximately 100. The latter is expressed as the percentage of input surface area to output surface area. As such, the gain can be reduced if the applied voltage is reduced. For example, an image intensifier with an incident window size of 25 cm and an output window size of 2.5 cm has a minification gain of approximately 100. The total gain, in this case, is 10,000, which is the product of the flux gain and minification gain. An incident window size of 10–40 cm can be used. Image intensifiers with a wide field-of-view have a larger gain due to minification gain but are also more likely to generate image distortion.

Second-generation image intensifiers use a *microchannel plate* (*MCP*) instead of an electron lens due to electron multiplication, as shown in Fig. 4.70b. An MCP has a structure comprised of multiple glass pipes with a diameter of 10 μm and length of 1 mm clustered together in a slight inclination. This acts as an electron multiplier by having electrons repeatedly collide into channel walls due to the voltages applied on both ends, which in turn emit secondary electrons each time this occurs. The photocathode, MCP, and output fluorescent screen are placed immediately adjacent to one another; the MCP interior is as shown in Fig. 4.71. Moreover, accelerating an electron in each channel interior increases these numbers and MCPs are used

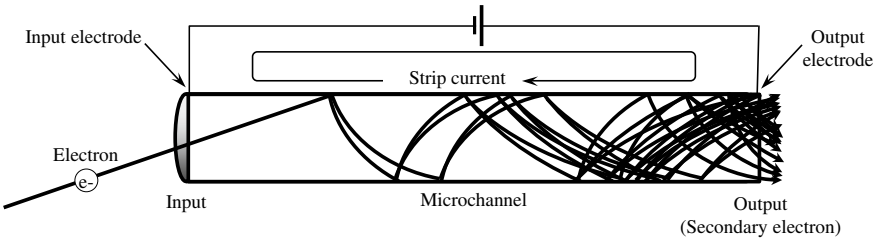

Fig. 4.71 Schematic showing the structure and operations of a microchannel plate

in stacks when high sensitivity is required. A cathode voltage is applied between a photocathode and MCP and a screen voltage is applied between the MCP and fluorescent screen. The electron is then accelerated and guided to the CCD camera with the *fiber optic plate* (*FOP*) after being converted to visible light on the output side.

Similarly to the second-generation image intensifiers, third-generation image intensifiers use an MCP but also increase their sensitivity by using semiconducting crystals such as gallium arsenide (GaAs) or gallium arsenide phosphide (GaAsP) on the photoelectric surface.

Others in use include color image intensifiers, which use fluorescent screens emitting multiple colors to conduct imaging with a color camera and high-speed image intensifiers, which use high-speed response fluorescent screens to image with high frame rate cameras. Aluminum is used as the material in the incident window but beryllium can also be used. This enables imaging with low-energy X-rays.

Finally, representative image intensifier products that are currently commercially available are shown in Fig. 4.72.

(3) CCD Camera

Fig. 4.72 Example of a commercially available image intensifier; **a** Hamamatsu Photonics V10709P (courtesy of Hamamatsu Photonics) and **b** Canon Electron Tubes & Devices E5877J-P1K (courtesy of Hitoshi Chiyoma of Canon Electron Tubes & Devices)

The CCD camera primarily involves conducting impurity doping or surface treatment (e.g. oxide film production) on a silicon wafer, creating a chip by transcribing a detailed pattern like an IC on the wafer. The voltage from CCD image signals forms a row of square waves whose amplitude is proportional to the photon number detected at each pixel. Commercially-available products with pixel sizes as low as 5 μm and pixel numbers at a maximum of 4,096 × 4,096 can be used. As shown in Sect. 4.4.1 (4), dark noise is reduced for scientific measurements by placing the CCD on a Peltier device and cooling the element to approximately −30–100 °C. The Peltier device is a semiconducting element in which passing an electric current in the dissimilar metal joint induces the Peltier effect, generating heat on one side and cooling on the other. Furthermore, there are CCD cameras that use liquid nitrogen for cooling. Condensation and frost can form when temperature differences between the exterior and the element are large, so the camera head is placed in a vacuum container and sealed to prevent these effects.

The fundamental imaging principles of a CCD camera are based on the *internal photoelectric effect*; where electrons in a valence band jump over a forbidden band and are excited into the conduction band when light is irradiated on a semiconductor, resulting in the increase of conduction electrons within the material interior. The basic operation of the CCD camera is to accumulate the generated signal charge within the semiconductor, transferring and reading them out to necessary locations as required.

CCD cameras mainly use photodiode or photo-*metal oxide semiconductor* (*MOS*) elements. Figure 4.73 shows a schematic of a *MOS capacitor*. An insulating layer made of silica is distributed on top of a p-type semiconducting substrate and either a thin metallic electrode (e.g. polysilicon film) or transparent electrode made of an indium tin oxide (ITO) is placed on top of this. The initials of these three layers comprise the abbreviation "MOS." Applying a positive voltage to a given electrode

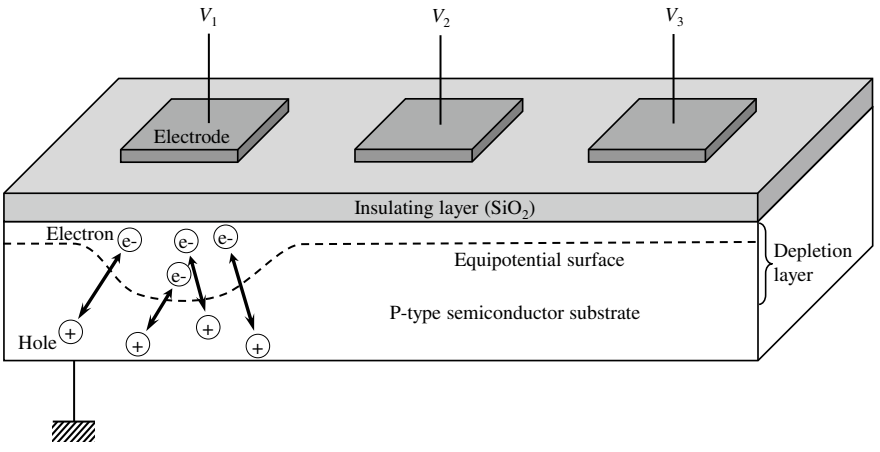

Fig. 4.73 Schematic of the basic structure of a CCD with a MOS capacitor

results in the positive hole within the p-type semiconductor moving away from the electrode, creating a *depletion layer* immediately below the electrode. The p-type semiconductor near the electrode takes a high potential and a *potential well*, which is surrounded by ground potential areas, is formed. Meanwhile, an n-type semiconductor is implanted within a p-type semiconductor at the photodiode, thereby generating a diode. Applying a reverse bias to this, results in the separation of the photoelectron from the positive hole and its accumulation in the n-type semiconducting layer. Figure 4.73 shows that the silicon crystals at the interface between the silicon and insulating layers are truncated and that *dangling bonds* of the silicon atoms are present. Photoelectrons are captured by having high-density localized levels existing in the forbidden bands, where noise is also more easily generated. An embedded channel structure, wherein the potential well is created slightly away from the interface by placing an n-type silicon layer between the silicon and insulating layers, is used.

The basic principles of charge transfer are shown in Fig. 4.74. Applying a positive 10 V electric potential on the central electrode after applying a positive 10 V electric potential on the left electrode results in the electrons distributed across the vicinities of both electrodes. Subsequently reducing the electric potential of the left electrode to 2 V results in the accumulation of electrons near the central electrode. Furthermore, sequential repetitions of this operation on the right electrode results in the charge being transferred to the right side of the figure along the semiconducting surface. In this manner, the charge can be transferred with the electrode as a single unit. There are three mechanisms by which electrons are transferred: *self-induced drift*, in which electron drift occurs due to electric potential gradients generated from the localization of charges; *thermal diffusion*; and *fringing-field drift*, due to electric potential gradients generated by applied voltages.

However, as in Figs. 4.75 and 4.76, it is often the case in actual practice that 2 to 4 electrodes are wired for a single pixel and charge transfers are conducted through a 4-phase clock pulse, where the same voltage is applied in connected electrodes in the same group. Figures 4.75 and 4.76 show a *4-phase drive*, where every four electrodes are connected. This method is widely used. At time t_1, a signal charge is present at electrode groups C and D. At time t_2, the charge spreads to electrode group B and the amount at electrode group D conversely decreases. At time t_3, the transfer of a single electrode's worth is completed compared to time t_1.

A 2-phase drive has the doping of impurities on the semiconductor immediately below the electrode and its concentration gradients are used to generate electric potential gradients. The electrodes in these cases are divided between storage electrodes and transfer electrodes. The amount of charges that can be handled is limited but this is suited for high-speed operations as a simple structure and operations at high-clock frequency are possible; 3-phase and 4-phase drives do not require doping. Furthermore, there is no distinction between storage electrodes and transfer electrodes. Transfer is determined through clock timing sequences shown in Fig. 4.75. Although the number of electrodes and wires per pixel increases, a 4-phase drive has the advantage of an increased number of charges that can be handled as this

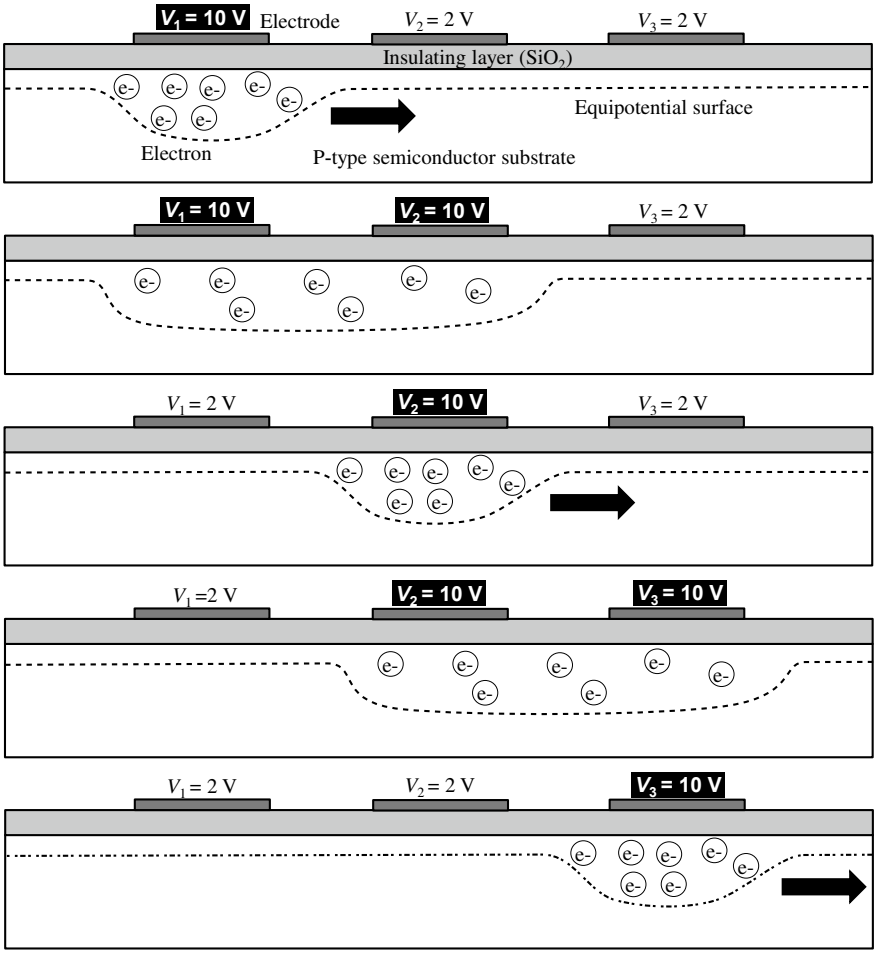

Fig. 4.74 Schematic showing charge transfer between electrodes in a CCD made from a MOS capacitor

corresponds to about half of the overall surface area. Furthermore, transfer in both directions becomes possible.

Figure 4.77 shows four representative electron transfer systems when looking at the overall CCD camera. The *interline transfer* (*IT*) system in Fig. 4.77a has a relatively complex structure in which the light-receiving section and transfer section are independent of each other. The light-receiving element and the light-shielded vertical transfer CCD comprises a single pixel, whose fill factor is relatively small. The signal charge of each pixel following exposure is promptly transferred to the adjacent vertical transfer CCD through the transfer gate. This transfer is instantaneously conducted for all pixels. Afterward, this is transferred row by row to the horizontal transfer CCD and output after converting from a charge to a voltage in the

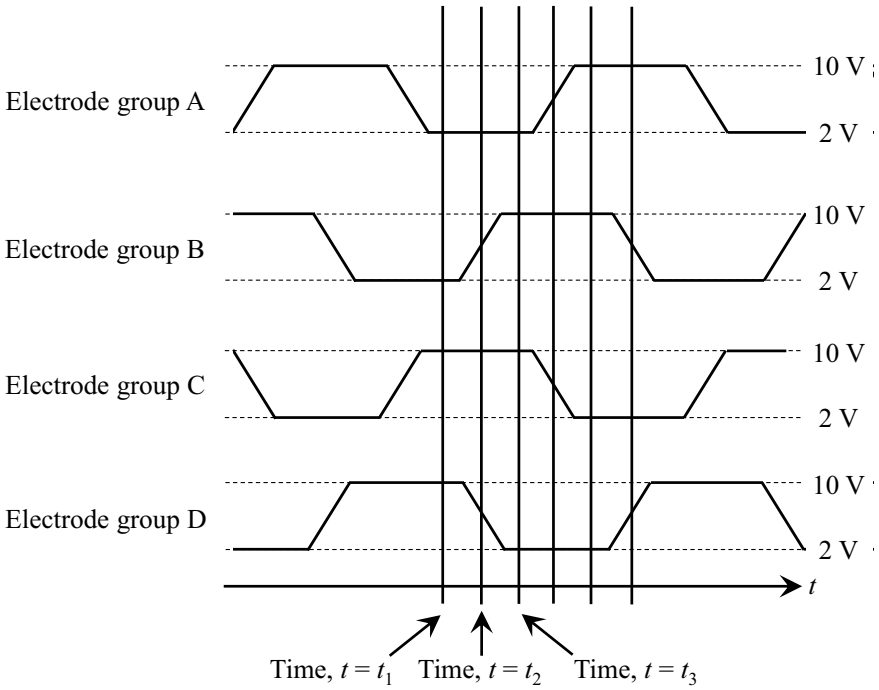

Fig. 4.75 Chart of charge transfer timing between electrodes in a 4-phase drive CCD camera, corresponding to the schematic in Fig. 4.76

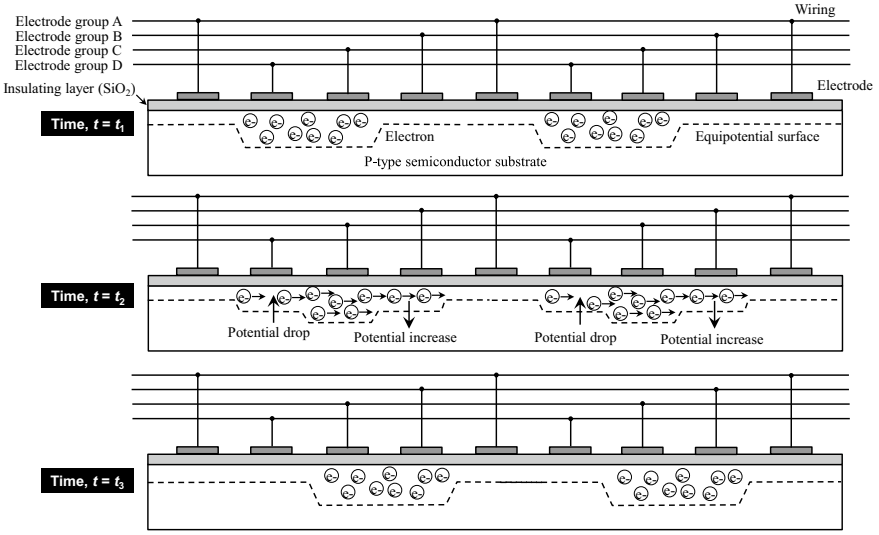

Fig. 4.76 Schematic showing the charge transfer between electrodes in a 4-phase drive CCD camera; time corresponds to the timing chart in Fig. 4.75

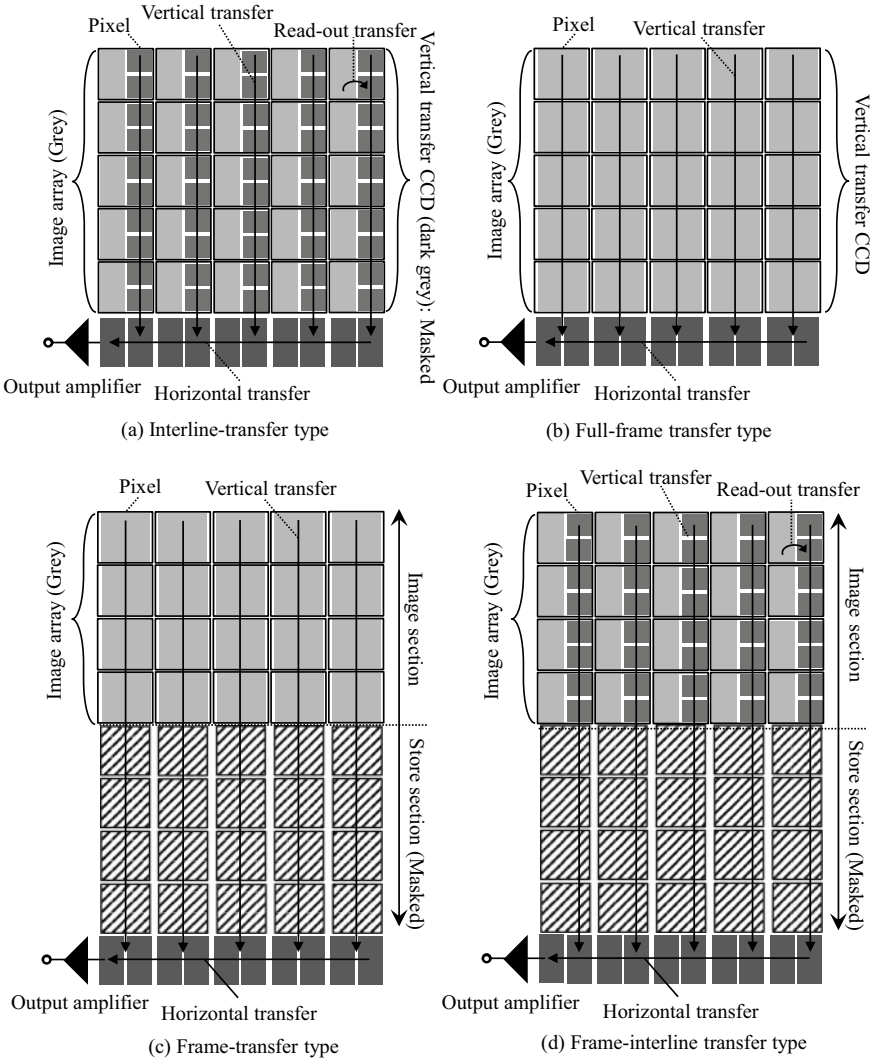

Fig. 4.77 Schematic showing the representative charge transfers in a CCD camera

output circuit. This transfer is conducted during the next exposure, so a shutter is not required. The size can be reduced as an accumulation section is not required, such as in a frame transfer method. IT-CCD cameras with minimal dead time specialize in continuous exposure and are also used in video and digital cameras. They have the disadvantage of generating *smear* due to charge leaking into the vertical transfer CCD. Smear refers to white thread-like artifacts in the vertical direction, which are generated due to signal charges caused by strong incident light entering adjacent pixels or the CCD transfer region and blurring the image. Furthermore, a micro-lens

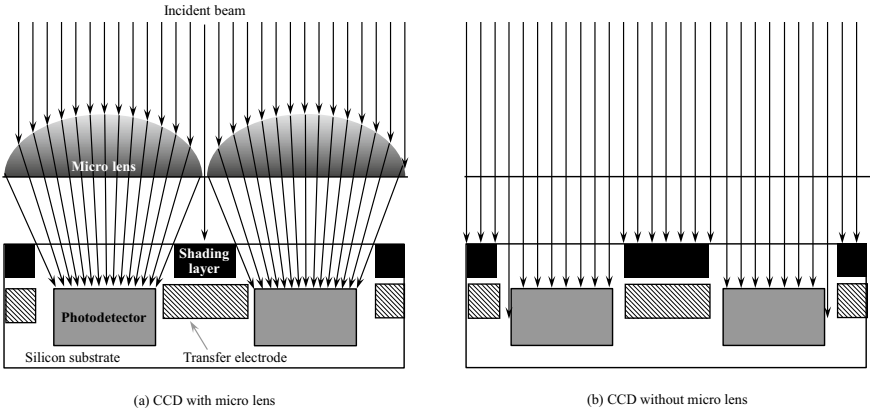

Fig. 4.78 Schematic showing the focusing effects of a micro lens

as shown in Fig. 4.78 is installed as the shielded region in an IT-CCD camera is wide and sensitivity is improved by focusing the light incident to the shielded section and guiding it to the light-receiving section.

The basic principles of the output circuit are to convert the charge Q into a voltage change ΔV_{out} between both ends of the condenser with a capacity C_{C}.

$$\Delta V_{out} = \frac{Q}{C_c} \tag{4.44}$$

Conversions using a condenser with a small capacity are beneficial as they can obtain a high voltage. Generally, an amplifier referred to as a *floating diffusion amplifier* (*FDA*) is used in CCD cameras. As previously mentioned, the read-out noise becomes predominant when the element is cooled to an extent where the dark noise can be ignored. The read-out noise from the CCD camera is mainly *thermal noise* due to channel resistance of MOSFET, which primarily comprises the FDA. Moreover, there is also *reset noise* and *1/*f *noise*; the former is generated when the capacitance of the FDA is reset and is due to fluctuations in reset electric potential due to the mixing-in of thermal noise induced by channel resistance. As can be observed in the following equation, the reset noise is proportional to the absolute temperature and condenser capacity [62] and is also referred to as *kTC noise*:

$$Q_{kTC} = \sqrt{kTC_C} \tag{4.45}$$

Here, Q_{kTC} is the amount of electric charge of noise due to the reset noise and k is the Boltzmann constant; in other words, a lower condenser capacity results in a further suppressed amount of electric charge of noise and conversely increased noise voltage. The electric charge is completely transferred in the case of a CCD

camera and the kTC noise is generally not generated in the scanning region. CCD cameras can endogenously be considered to have low noise compared to CMOS cameras. Furthermore, the reset noise is removed by an external circuit referred to as a *correlated double sampling (CDS) circuit*, which takes advantage of the fact that the reset noise is present in the signals of both the reset and data sections, utilizing the difference between the sections. Meanwhile, the $1/f$ noise occurs due to the silicon interface state. As decreases in noise amount are inversely proportional to the frequency f, this noise is particularly problematic in the low-frequency region. This can also be reduced through the CDS circuit.

Incidentally, there is an *electron-multiplying CCD* (*EM-CCD*) camera, which has high sensitivity and an image multiplication functionality due to specialized output registers formed on its chip. The EM-CCD camera was separately developed in 2002 by Texas Instruments and E2V. EM-CCD cameras are not frequently used in X-ray tomography but are suitable for weak light and high-speed imaging applications. In an EM-CCD camera, the electrons in the bottom-most row of the detector are transferred to the multiplication register for each pixel, where the electron can be multiplied by a factor of up to several thousand while still suppressing the read-out noise [63]. This multiplication register is made of several hundred rows of registers. Electron multiplication is conducted through impact ionization caused by a high electric field created by applying a voltage higher than that of a standard horizontal transfer electrode [63]. The read-out noise can be reduced to less than one through electron multiplication [63], but the dark current is amplified alongside the signal. The *clock induced charge (CIC) noise*, generated when the charge drift occurs from the detection element due to electron multiplication, also becomes a new source of noise [63].

The *full-frame transfer (FF)* type in Fig. 4.77b uses virtually all of its surfaces as light-receiving sections. The signal charge is accumulated in the potential well of the light-receiving section during exposure. This is then transferred downward row by row with a vertical transfer CCD and outputted pixel by pixel with a horizontal transfer CCD. Vertical transfer of the next row is conducted once this is complete. The structure is simple, a large number of pixels is possible, and the pixel size can be increased. There is no requirement to set up a transfer region separately from the light-receiving section and the charge-accumulating region can be made wider than in the interline transfer method. For this reason, this technique has the advantages of both high sensitivity and dynamic range and is widely used for scientific measurements. The next exposure cannot be conducted until the output of all pixels is completed, so the read-out time becomes dead time. For this reason, this is not suitable for consecutive exposures like those of a video camera and is instead primarily used for measurements with a low frame rate. Furthermore, a mechanical shutter must be installed to prevent incident light during readout. This results in limits to the control of exposure time, however, which can also result in malfunction.

The *frame transfer* (*FT*) type in Fig. 4.77c has a completely shielded accumulation section with the same pixel number as the light-receiving section. After exposure, the signal charges of all the pixels are simultaneously transferred to the accumulation section and the rows are read out one by one similar to the full-frame transfer type. The

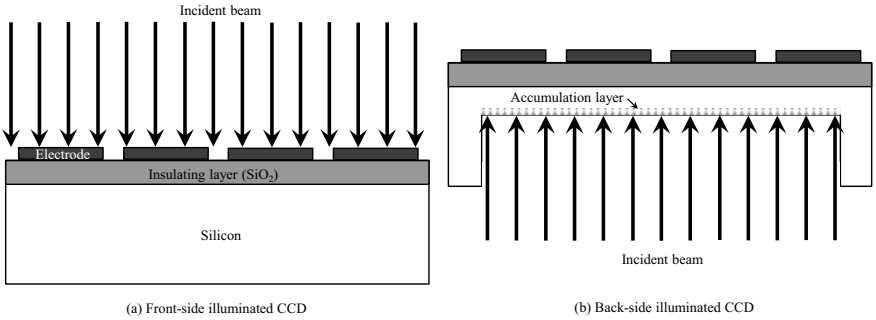

Fig. 4.79 Schematic of front-side and back-side illuminated CCD structures

transfer from the light-receiving section to the accumulation section is conducted at a high speed and the charge production due to light received during transfer is limited. Furthermore, this also has the advantage of allowing for the next exposure during readout from the accumulation section. The total dead time is low and this can also be used for video imaging. Meanwhile, disadvantages include a larger chip size due to the accumulation section and the possibility of smears. The full-frame transfer and frame transfer methods both have a structure that allows for the light transmission of transfer electrodes. There are countermeasures for improving sensitivity that can be implemented, such as using a transparent electrode or a *back-side illuminated* structure.

Figure 4.79 shows a comparison between the front-side and back-side illuminated structures. The incident light in the front-side illuminated CCD camera in Fig. 4.79a is absorbed by the electrode and reflected by the protective screen and oxide screen (e.g. boron phosphor silicate glass (BPSG) on the front-side), greatly reducing its quantum efficiency. Setting up a back-side illuminated structure such as in Fig. 4.79b can greatly increase the quantum efficiency from approximately 40%–90%, as shown in Fig. 4.80 [64]. Furthermore, the back-side illuminated camera can also measure ultraviolet rays (400 nm wavelength and below) and some near-infrared rays (750–1400 nm wavelength), which do not reach the light-receiving element of the front-side illuminated camera. However, another potential well, shown in Fig. 4.81, exists on the back-side of the CCD camera, where the charge cannot be transferred to the front-side electrode [65]. Ion implantation is conducted on the back-side with this in mind and an internal potential, which allows for charge to move from the back-side to the front-side, is generated [65]. The front-side is a p-type semiconducting region with high impurity concentrations referred to as an *accumulation layer*. The substrate thickness is reduced to around 20 μm in back-side illuminated structures to ensure acceptable resolution [65].

The *frame interline transfer* (*FIT*) type in Fig. 4.77d has pixels with the same structure as the interline transfer type and accumulation section as the frame transfer type. Signal charge can be instantaneously transferred to the completely shielded accumulation section through high-speed frame transfer. Furthermore, smear discharge

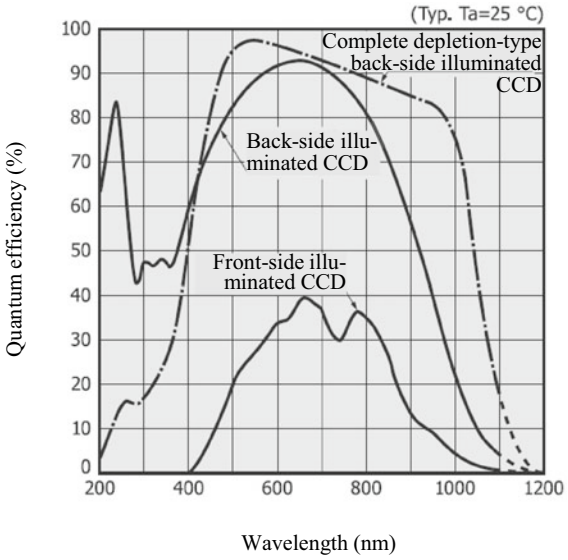

Fig. 4.80 Comparison of the spectral sensitivity characteristics of a backside and front-side illuminated CCD (courtesy of Hamamatsu Photonics)

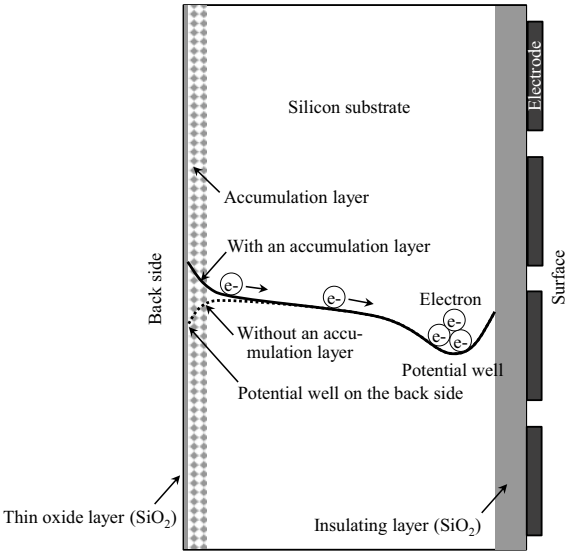

Fig. 4.81 Back-side illuminating CCD structure, internal electric potential, and charge movement

transfer is conducted to remove charges due to the smears generated during vertical transfer before readout transfer. Due to these aspects, this type has the characteristic of generating virtually no smear; its chip size is large and its power consumption is high.

Here, we examine the binning described in Sect. 4.4.1 (4) from the perspective of charge transfer. Figure 4.82 shows a schematic of the basic process when 2×2 binning is conducted on a full-frame transfer-type CCD camera. Transfer is conducted in the vertical direction and two columns' worth of signal charge is accumulated in the horizontal transfer CCD. When horizontal transfer is subsequently conducted, two rows' worth of signal charge is accumulated in the output node, enabling the signal charge in 2×2 pixels to be processed as a sum. Furthermore, the added number can be increased up to 2×2, 4×4, 8×8, etc. The readout is a single session compared to the numerical additions conducted after the readout of each pixel, which has the advantage of controlling the read-out noise. This can be particularly effective when the signal level is low.

Finally, the specifications of the various commercially-available CCD cameras used for scientific measurements are shown as reference in Tables 4.7, 4.8 through 4.9. Here, CCD cameras for direct X-ray detection, EM-CCD cameras, and other cameras in which the element is cooled, are displayed. Furthermore, Fig. 4.83 shows photographs of the external appearance of representative CCD cameras for scientific

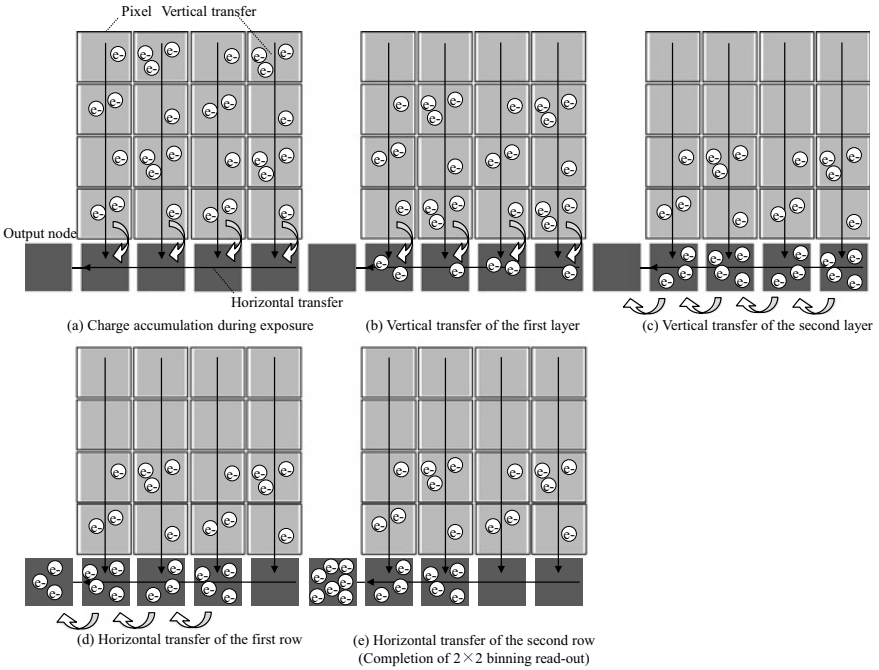

Fig. 4.82 Basic process when conducting 2×2 binning with a full-frame transfer-type CCD camera

Table 4.7 Representative cooled CCD cameras that are commercially available and their specifications

Manufacturer	Roper Technologies			PCO.AG		
Type	PyLoN 2 KB Ex	Blaze 400-LD	Sophia 2048B Ex	pco.dimax HS1	pco.dimax HS4	Pco.dimax CS1
Number of pixels	2048 × 512	1340 × 400	2048 × 2048	1000 × 1000	2000 × 2000	1296 × 1024
Pixel size (μm)	13.5 × 13.5	20 × 20	15 × 15	11 × 11	11 × 11	11 × 11
Back-side/Front-side illumination	Back side	Back side	Back side	Front side	Front side	Front side
Maximum quantum efficiency (%)	97	97	97	50	50	50
Read-out rate (Frames/sec)	3.2	35	3.2	7039	2277	3086
Read-out noise (Electrons-rms)	3.5 @ 50 kHz	2.5 @ 100 kHz	4.5 @ 100 kHz	23	23	22
Cooling system	Liquid nitrogen	Peltier elem. + Air/Water	Peltier elem. + Air/Water	Nil	Nil	Nil.
Minimum cooling temperature (°C)	120	−95/−100	−90/−90	Room temperature	Room temperature	Room temperature
Dark current (Electrons/pixel/sec)	0.1 @ −120 °C	0.0005 @ −100 °C	0.00025 @ −90 °C	530 @ 20 °C	530 @ 20 °C	530 @ 20 °C

(continued)

Table 4.7 (continued)

Manufacturer	Roper Technologies			PCO.AG		
Type	PyLoN 2 KB Ex	Blaze 400-LD	Sophia 2048B Ex	pco.dimax HS1	pco.dimax HS4	Pco.dimax CS1
Full well capacity (Electrons)	800,000	180,000	150,000	36,000	36,000	36,000
Dynamic range (bit)	16	16	16	12	12	12
Hamamatsu Photonics	Thorlabs	BITRAN			ANDOR	
C8000-30	8051 M-USB-TE	BU-51LN	BU-62 M	BQ-83E	DF936N-FB-T2	ZYLA-5.5X-FO
640 × 480	3296 × 2472	1360 × 1024	2048 × 2048	1024 × 1024	2048 × 2048	2560 × 2160
14 × 14	5.5 × 5.5	7.4 × 7.4	7.4 × 7.4	24 × 24	13.5 × 13.5	6.5 × 6.5
Back side	Front side	Front side	Front side	Front side	Front side + FOP	Front side + FOP
90-	51% at 460 nm	60	55	75	97	60
31.4	4.5	17	16	3	0.953	100
150 @ 31.4 Hz	<10 e- at 20 MHz	–	12	13	35 @ 5 MHz	0.9 @ 200 MHz
Peltier elem. + Air cooling	Peltier element	Peltier elem. + Water cooling	Peltier elem. + Water cooling	Peltier elem. + Water cooling	Peltier elem. + Air/Water	Peltier elem. + Air cooling
+ 5	−10 @ Room temperature	−25	−35	−25	−35	0
–	0.1	–	7 @ 40 °C	15.3 @ 25 °C	0.09	0.14
30,000	20,000	16,000	44,000	200,000	100,000	30,000
12	14	16	16/12	16	16	16

Table 4.8 Representative commercially available CCD cameras for direct X-ray detection and their specifications

Manufacturer	Roper Technologies			ANDOR		
Type	PI-MTE In-Vacuum	SOPHIA-XO:2048B	PIXIS-XO:2048B	DO934P	DO936N	iKon XL "SO" 230
Number of pixels	2048 × 2048	2048 × 2048	2048 × 2048	1024 × 1024	2048 × 2048	4096 (H) × 4112 (V)
Pixel size (μm)	13.5 × 13.5	15 × 15	13.5 × 13.5	13 × 13	13.5 × 13.5	15 × 15
Energy range (keV)	1.2–30000	1.2–30000	1.2–30000	–	–	–
Maximum quantum efficiency (%)	96	96	96	–	–	95
Read-out rate (Frames/s)	0.42	3.2	0.44	4.4	0.953	>0.5
Read-out noise (Electrons-rms)	3 @ 50 kHz	4.5 @ 100 kHz	3.5 @ 100 kHz	18 @ 5 MHz	31.5 @ 5 MHz	23 @ 4 MHz
Cooling system	Peltier elem. + Water	Peltier elem. + Air/Water	Peltier elem. + Air/Water	Peltier elem. + Air/Water	Peltier elem. + Air/Water	Peltier elem. + Air/Water

(continued)

Table 4.8 (continued)

Manufacturer	Roper Technologies			ANDOR		
Minimum cooling temperature (°C)	−55	−90/−90	−70/–70	−100	−100	−75
Dark current (Electrons/pixel/s)	0.02 @ −50 °C	0.00025 @ −90 °C	0.002 @ −60 °C	0.0001 @ −100 °C	0.0001 @ −100 °C	0.0001 @–75 °C
Full well capacity (Electrons)	100,000	150,000	100,000	–	–	150,000
Dynamic range (bit)	16	16	16	16	16	16/18

Hamamatsu Photonics	BITRAN		XiMEA		Photonic Science			Raptor Photonics
C8000-30D	BK-501 X	BK-502 X	MH110XC-KK	MH160XC-KK	PSL FDS 2, 83_M	PSL FDS6, 02_M	PSL X-ray VHR 80	Eagle XO X-Ray
640 × 480	1024 × 1024	1024 × 1024	4008(H) × 2672(V)	4872(H) × 3248(V)	1940(H) × 1460(V)	2750(H) × 2200(V)	4008(H) × 2672(V)	2048 × 2048
14 × 14	13 × 13	13 × 13	9 × 9	7.4 × 7.4	4.54 × 4.54	4.54 × 4.54	16 × 16	13.5 × 13.5
0.02–10	0.1–1	1–10	5–100	5–100	5–100	5–100	5–100	0.0012–20
–	90	90	–	–	–	–	–	90

(continued)

Table 4.8 (continued)

Hamamatsu Photonics	BITRAN		XiMEA		Photonic Science			Raptor Photonics
31.4	0.6	0.6	2.1	1.4	3.7	1.7	1.8	–
100 @ 31.4 Hz	12 @ 1 MHz	12 @ 1 MHz	10	8	5–6 @ 12.5 MHz	5–6 @ 12.5 MHz	14–15 @ 10 MHz	2.3 @ 75 kHz
Peltier elem. + Air	Peltier elem. + Air	Peltier elem. + Water	Peltier elem. + Air	Peltier elem. + Air	Peltier elem. + Air	Peltier elem. + Air	Peltier elem. + Air	Peltier elem. + Air, water or liquid nitrogen
+ 5	−35	−35	+12	+12	−20	−20	−10	−90
–	500 @ 20 °C	−500 @ 20 °C	40 @ 12 °C	18 @ 12 °C	0.05 @ −20 °C	0.05 @ −20 °C	0.5 @ −10 °C	0.0004 @ −75 °C
30,000	100,000	100,000	60,000	30,000	18,000	18,000	45,000	100,000
12	16	16	14	14	14	14	16	16

Table 4.9 Representative commercially available EM-CCD cameras and their specifications

Manufacturer	Hamamatsu Photonics		Roper Technologies		Raptor Photonics
Type	C9100-23B	C9100-24B	Pro-EM-HS: 512BX3	Pro-EM-HS: 1024BX3	Falcon III
Number of pixels	512 × 512	1024 × 1024	512 × 512	1024 × 1024	1024 × 1024
Pixel size (μm)	16 × 16	13 × 13	16 × 16	13 × 13	10 × 10
Maximum EM gain	1,200	1,200	1000	1000	5000
Maximum quantum efficiency (%)	>90	>90	95	95	95
Read-out rate (Frames/s)	1076	314	61	25	34
Read-out noise (Electrons-rms)	<1 (EM gain 1200)	<1 (EM gain 1200)	<1 (EM Gain 1000)	<1 (EM Gain 1000)	0.01
Cooling system	Peltier elem. + Water	Peltier elem. + Water	Peltier elem. + Air/Water	Peltier elem. + Air/Water	Peltier elem. + Air, water or liquid nitrogen
Minimum cooling temperature (°C)	−100	−80	−80/−90	−65/−65	−100
Dark current (Electrons/pixel/s)	0.0005 @ −80 °C	0.0005 @ −80 °C	0.001 @ −70 °C	0.002 @ −55 °C	0.0002
Full well capacity (Electrons)	370,000	400,000	200,000	80,000	35000
Dynamic range (bit)	16	16	16	16	16
ANDOR		BITRAN		Nüvü cameras	
iXon-Ultra 888	iXon-Ultra 897	BU-66EM-VIS	BQ-87EM	CCD55-30	
1024 × 1024	512 × 512	1920 × 1080	512 × 512	1024 × 1024	
13 × 13	16 × 16	5.5 × 5.5	16 × 16	13 × 13	
1000	1000	20	100	5000	
>95	>95	50	90	90	
26	56	55	55	17.5	
<1	<1	1 (EM gain 20)	1 (EM gain 100)	<0.1 @ 20 MHz	
Peltier elem. + Air/Water	Peltier elem. + Air/Water	Peltier elem. + Water cooling	Peltier elem. + Water cooling	Peltier elem. + Water cooling	

(continued)

Table 4.9 (continued)

ANDOR		BITRAN		Nüvü cameras
iXon-Ultra 888	iXon-Ultra 897	BU-66EM-VIS	BQ-87EM	CCD55-30
−95	−100	−35	−50	−85
0.00011 @ −95 °C	0.00015@ −100 °C	6 @ 0 °C	400 @ 20 °C	0.0004@ −85 °C
80,000	180,000	20,000	130,000	800,000
16	16	16	16	16

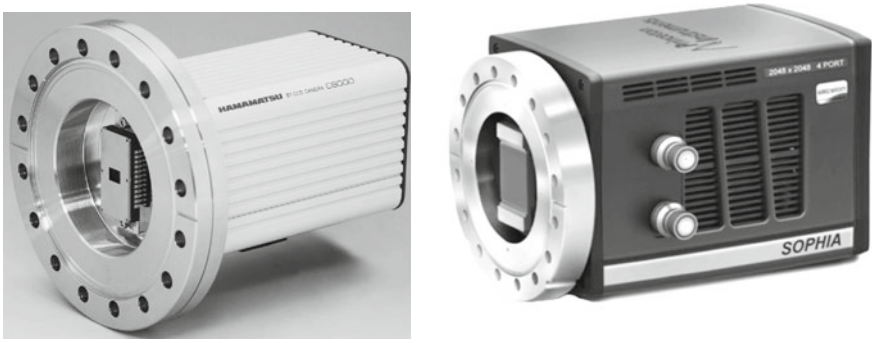

(a) (b)

Fig. 4.83 Example of commercially available CCD cameras for scientific measurements; **a** Hamamatsu Photonics C8000-30D model (cooling CCD camera courtesy of Hamamatsu Photonics) and **b** Roper Technologies PIXIS-XB model (CCD camera for direct X-ray detection courtesy of Kazuyuki Hara of Nippon Roper)

measurements that are currently commercially available. The pixel size in the table is determined by the spatial resolution required by the X-ray CT scanner, sample size, magnification due to the cone beam, and magnification due to the FOP and optical lens (discussed later). Similarly, the number of pixels determines the spatial resolution of the X-ray CT scanner through the sampling theorem discussed below.

(4) CMOS Camera

When comparing CMOS and CCD cameras, there are no differences in the readout and amplification of photoelectric conversion or signal charge. Their difference is in the readout method of the signal charge and the microstructure of the elements, which make that possible. CCD cameras are manufactured through a special process but CMOS cameras are made through a standard CMOS LSI manufacturing process. Figure 4.84 shows the relationship between the Intel CPU release year and the minimum gate length [66]. The minimum gate length has undergone a miniaturization process, wherein its length decreases by a factor of 0.7 and its surface area

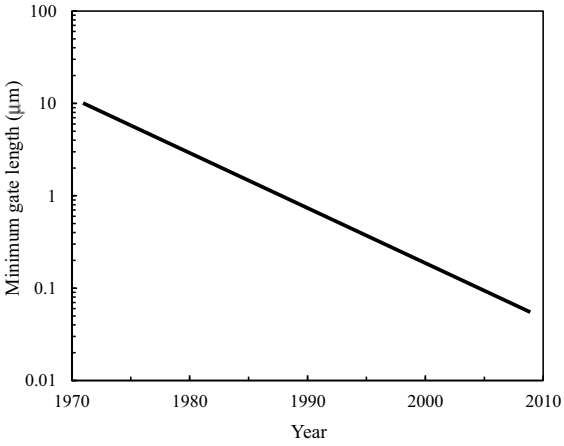

Fig. 4.84 History of miniaturization of the CMOS process [64]

halves every 2 to 3 years [66]. The CMOS camera was put to practical use in the 1990s when semiconducting micro-fabrication techniques were developed and the minimum gate length reached approximately 0.35 μm [67]. High-quality images were obtained due to the development of micro-fabrication techniques, which enabled an amplification a *field-effect transistor* (FET) to be installed in each pixel and where circuits for inhibiting fixed pattern noise were installed. Furthermore, their costs have been reduced by applying existing semiconductor manufacturing processes. For these reasons, the spread of CMOS cameras and its substitution of CCD cameras has rapidly increased in recent years. In this context, Sony announced a complete production suspension of CCD sensors in March 2015. It is anticipated that future transitions from CCD cameras to CMOS cameras will continue.

Signal charges transferred from each pixel to the output section of CCD cameras undergo impedance transformation using the *source-follower amplifier* shown in Fig. 4.85. The source-follower circuit is a basic amplifier circuit, which uses an FET. The gate terminal (G) is the input, the source terminal (S) is the output, and the drain (D) is common to both. As shown in Fig. 4.86, the source follower is referred to as

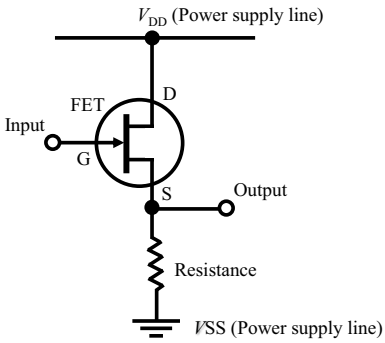

Fig. 4.85 Basic circuit of a source follower that uses an NMOS

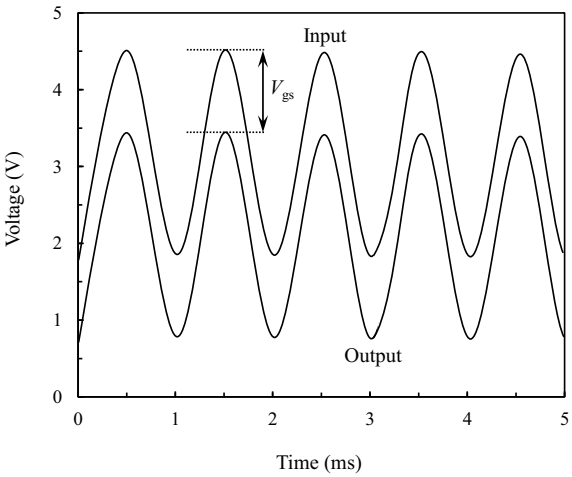

Fig. 4.86 Schematic showing the input/output voltage waveforms of the source follower circuit

such because the output signal moves as if to follow the input signal. Under ideal conditions, the input voltage V_{in} and output voltage V_{out} are equivalent, as in the following equation.

$$V_{out} = V_{in} \tag{4.46}$$

Furthermore, the input impedance is high and the output impedance decreases to a range between $1/g_{\text{m}}$ and several kΩ (g_{m} is the transconductance (basic gain of FET)), hence, the source-follower amplifier can be interpreted as a buffer amplifier. However, the $V_{\text{in}}/V_{\text{out}}$ ratio does not become 1 in practice and is instead expressed by the following equation; here, V_{th} is the threshold voltage of the amplifying FET and G_{V} is the voltage gain of the source follower amplifier [67].

$$V_{out} = (V_{in} - V_{th})G_V \tag{4.47}$$

Here, G_{V} generally takes a value of 0.7–0.9 [67]. Furthermore, the amplification rate of the charge is between 100 to 10,000 times [67]. The signal charge can be amplified within the pixel, so the influence of noise generated in subsequent transfer stages becomes extremely small in comparison, as shown in the following equation:

$$N_t = \sqrt{G_V^2 N_{pixel}^2 + N_{readout}^2} \tag{4.48}$$

Here, N_{pixel} is the noise generated within the pixel and N_{readout} is the noise generated in readout circuits and various signal-processing circuits outside of the pixel. Meanwhile, the V_{th} value varies according to each transistor and fluctuates between the range of 10–100 mV [67]. This implies that the output for each pixel varies widely

for incident light of the same intensity. For this reason, the occurrence of fixed pattern noise is a larger problem in CMOS cameras than in CCD cameras.

The basic structure of a CMOS camera is shown in Fig. 4.87. An external appearance of a commercially-available element is shown in Fig. 4.88. The CMOS camera is an *active pixel sensor* (*APS*) in which each pixel has a source-follower amplifier, in which, unlike the CCD camera, readout is conducted after amplification. This is the same as the DRAM structure, which has dual-address signal lines composed of intersecting bit lines and word lines, with an FET located at each intersection. The signal charges accumulated due to light emission on each pixel are selected in the pixel selection circuit in the column direction, after which the pixel selection circuit in the row direction is used to read out the signal while conducting sequential scanning. The pixel to be read out is indicated with the (x, y) coordinates of the column and row and the post-amplification information can be read out by turning on the applicable MOS switch. Furthermore, limiting the readout to specified areas can increase the frame rate. This is a major point of difference from CCD cameras, which can only read out as indicated by the arrangement. Furthermore, the sequential readout enables this to be driven using a single low-voltage power source, thereby

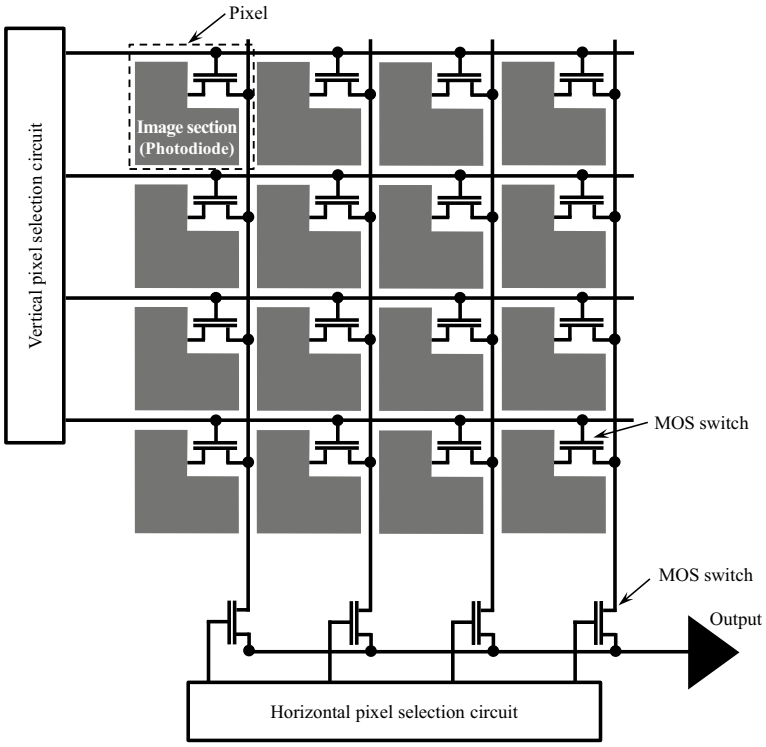

Fig. 4.87 Schematic showing the microstructure of a CMOS camera; each pixel is depicted as a passive pixel sensor without an amplifier for simplicity

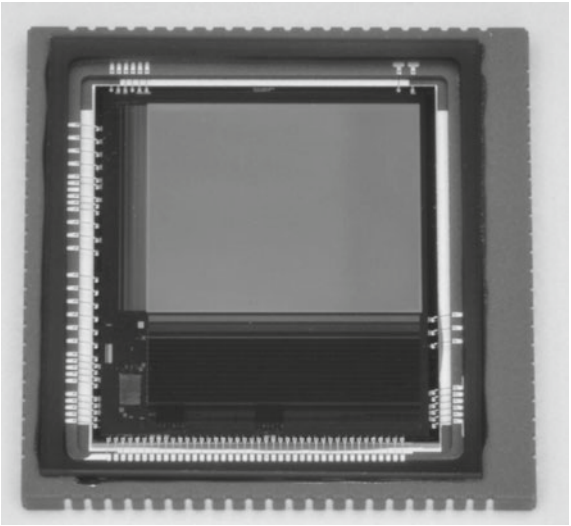

Fig. 4.88 Example of a commercially available CMOS image sensor, Hamamatsu Photonics S13101 model (courtesy of Hamamatsu Photonics)

requiring less power consumption. Incidentally, three power sources are required for the operation of the vertical and horizontal CCD in the CCD camera.

Next, a schematic of the flow process from when a single pixel receives light and obtains a charge to when a pixel signal is outputted is shown in Fig. 4.89 [62]. The photoelectric conversion of the incident light occurs at the photodiode, after which it is input in the source-follower circuit. Other than the photodiode, the pixel

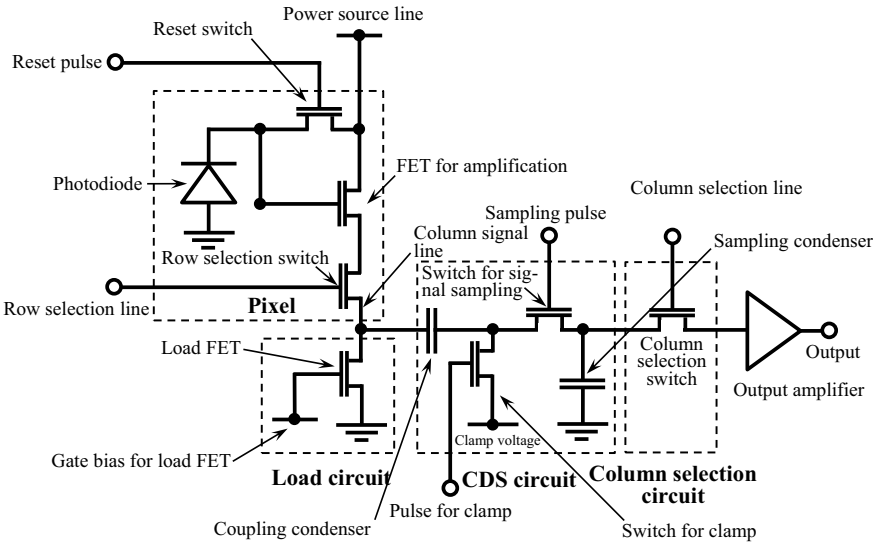

Fig. 4.89 Schematic of a basic circuit of a CMOS camera at the pixel level [65]

comprises the reset FET, which uses a reset pulse to reset the photodiode potential, and a line selection FET, which induces a conduction state between the load FET and amplification FET. After coming out of the source follower circuit, the column CDS type in Fig. 4.89 takes the difference between the signal in the reset section and the signal in the data section at the CDS circuit connected to the column signal line and the fixed pattern noise is removed. A clamp pulse is applied to the clamp FET when the signal voltage is input at the CDS circuit, and the clamp FET is turned off after the voltage at that terminal is set as the clamp voltage [67]. Regarding the second signal charge, the existence of the coupling condenser results in a potential equivalent to the change in both signals appearing in between the terminals. The difference of both signals can be obtained by retaining this potential at the sampling condenser by applying a sampling pulse in the sampling FET [67]. The signal charge retained in the sampling condenser is guided into the output amplifier due to the column selection pulse of the column selection circuit, which is then amplified to become an output image [67]. However, fixed pattern noise cannot be completely removed; the variability of the CDS circuit itself can act as the source of the fixed pattern noise, and load impedance varies depending on operation timing.

A simple structure in which each pixel is composed of three FETs is shown in Fig. 4.89; floating diffusion is set up in the photodiode in actual practice as shown in Fig. 4.90 and a fourth FET for reading out the floating diffusion between both are also frequently set up. In these cases, the reset floating diffusion potential is first outputted, after which the signal charge is transferred there, at which point the potential is outputted a second time. As both include the same reset noise, reset noise as well as fixed pattern noise can be removed from CDS circuits.

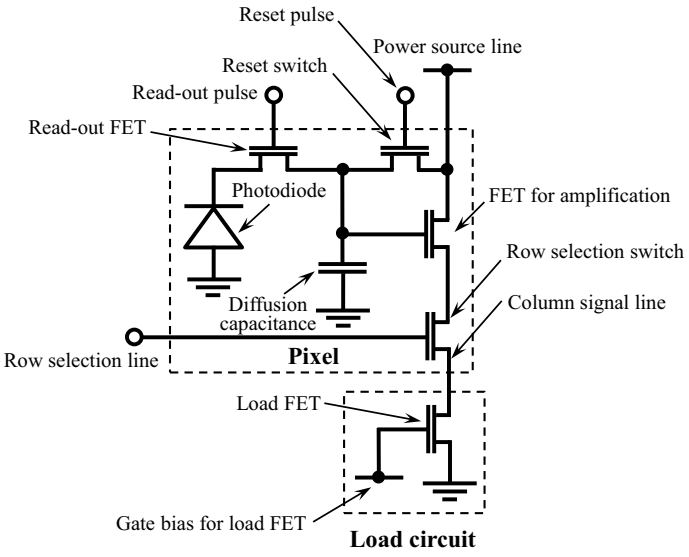

Fig. 4.90 Schematic showing the basic circuit of a CMOS camera with pixels that have 4 FETs

Incidentally, a typical CMOS sensor is a sequential exposure method by each pixel line, so there is a time lag in signal readout within the image screen. For this reason, dynamic distortion occurs when the subject movement is rapid relative to the exposure time. For example, a maximum temporal lag of 0.01 s occurs between pixels for the readout of the same image with a frame rate of 100 fps. Here, a *global shutter* functionality, which exposes all pixels simultaneously, can be realized if analog memory, which accumulates signal charge within the pixel for a duration equivalent to this lag, is prepared. Another FET must be added within the pixel to prepare the global shutter functionality, and either the fill factor of the pixel must be decreased or the size of the individual pixel must be increased. In contrast, those where resetting, accumulation, and readout are conducted for each line, as well as where the photoelectric transformation time is shifted for each line, are referred to as a *rolling-shutter* type. *Scientific CMOS* (*sCMOS*) cameras often use global shutters in addition to rolling shutters.

CMOS cameras are made using a standard CMOS LSI manufacturing process, so an AD converter can be incorporated in its interior. An AD converter can be incorporated in either the pixel, column, or final readout section. Noise is superimposed when an AD converter is inserted in the final readout section. Meanwhile, incorporating the AD converter in each pixel reduces the surface area percentage of the light-receiving area. Furthermore, variations in each pixel induce unevenness in sensitivity. Thus, setting up the AD converter in the column is currently a mainstream procedure. This has the advantage of not superimposing noise after *quantization* (approximating continuous analog data as digital data) with an AD converter. When considering the AD converter with an N_{AD}-bit resolution (*quantization bit rate*), signals below $\frac{V_{FS}}{2^{N_{AD}}}$ become information below one bit when the full voltage scale is set as V_{FS}, resulting in a *quantization error*. The noise generated from a *quantization error* can be considered random noise.

CMOS camera noise is compared with CCD camera noise and summarized in Table 4.10. The amount of dark current generation in photodiodes is also extremely high in a CMOS camera [62]. This is because a pn junction between the source/drain and substrate is used as a photodiode in the standard CMOS LSI manufacturing process; moreover, electron-hole pairs are thermally excited and generated mainly near the interface between the insulating SiO_2 screen and photodiode [62]. An embedded structure is used similar to that in CCD cameras to avoid this phenomenon. This process is thought to reduce the dark current to approximately 1/10 [62]. Of the four to five MOS FETs set up for every pixel, the noise generated by the threshold voltage V_{th} of the amplification FET has already been discussed. Much of the random noise in the pixel circuit is also due to this amplification FET [62]. Noise referred to as *random telegraph signal (RTS) noise* is prominent with decreases in the gate surface area accompanying the miniaturization of the pixel size. This occurs as a result of the entering and exiting of carriers in the silicon interface trap and appears as MOS FET drain potential fluctuations [62]. The reset noise in the CMOS camera mainly appears as the reset noise of a pixel.

Finally, we touch upon the sCMOS camera. The performance of sCMOS cameras has increased in recent years, as they have shown a tendency to replace CCD cameras

Table 4.10 Comparisons of the primary noise types present in CCD cameras and CMOS cameras

Type		CCD camera	CMOS camera
Random noise	kTC noise	Amplifier reset noise	Pixel reset noise
	Amplifier noise	$1/f$ noise	$1/f$ noise
		Thermal noise	Thermal noise
		–	RTS noise
		–	Output amplifier noise
	Dark noise	VCCD	–
		Photosensor	Photosensor
	Photon noise	Incidental to X-ray imaging irrespective of camera type	
Fixed-pattern noise	Dark noise	Photosensor	Photosensor
		VCCD	–
	Uneven sensitivity	Photosensor and others	Photosensor and others
		–	Variation in threshold voltage for Amplifier FET, V_{th}

for various scientific measurement applications. This is because characteristics like a high quantum efficiency, low noise, and high dynamic range have all been realized through various innovations, including an embedded-type photodiode, a micro lens, a column-parallel AD converter, (vacuum) cooling, the combined use of amplifiers with two standard high and low levels, global shutter functionalities, and back-side illumination. Specifications of various sCMOS cameras that are commercially available are summarized in Table 4.11. These should be compared with the CCD cameras and EM-CCD cameras shown in Tables 4.7, 4.8 and 4.9. Furthermore, Fig. 4.91 shows a photograph of the external appearance of a commercially-available sCMOS camera.

(5) Flat Panel Detector

The light-receiving surface size is 8–64 mm on a single size for various CCD cameras and sCMOS cameras in Tables 4.7, 4.8 and 4.9, 4.10 and 4.11. Most sCMOS cameras, in particular, have a size less than 20 mm. In contrast, flat-panel detectors are thin, have high performance and a large surface area. Light surface sections can measure from around 50 mm to up to 430 mm on one side. CCD cameras and sCMOS cameras are used in X-ray tomography at synchrotron radiation facilities, particularly in wiggler or undulator beamlines. In contrast, flat-panel detectors can be considered important detectors when imaging comparatively large samples or when placing the sample near the X-ray source to obtain high magnification. Many commercially-available X-ray CT scanner models have a flat panel detector installed as well, as in Table 6.1 shown later. Furthermore, high-performance flat panel detectors with a large effective light-receiving area size have been used in recent years and have begun

Table 4.11 Representative sCMOS cameras that are commercially available and their specifications

Manufacturer	ANDOR			PCO AG		
Type	Neo5.5	Zyla5.5	Zyla4.2 Plus	Pco.edge5.5	Pco.edge4.2	Pco.edge3.1
Number of pixels	2560 (H) × 2160 (V)	2560 (H) × 2160 (V)	2048 × 2048	2560 (H) × 2160 (V)	2048 × 2048	2048 (H) × 1536 (V)
Pixel size (μm)	6.5 × 6.5	6.5 × 6.5	6.5 × 6.5	6.5 × 6.5	6.5 × 6.5	6.5 × 6.5
Back-side/Front-side illumination	Front side	Front side	Front side	Front side	Front side	Front side
Maximum quantum efficiency (%)	60	60	82	60	82	60
Read-out rate (Frames/s)	100	100	100	100	100	50
Read-out noise (Electrons-rms)	1.3 @ 560 MHz	1.2 @ 560 MHz	1.1 @ 540 MHz	1.5 @ 95.3 MHz	1.4 @ 95.3 MHz	1.5 @ 105 MHz
Cooling system	Peltier elem. + Air/Water	Peltier elem. + Air/Water	Peltier elem. + Air/Water	Peltier elem. + Water	Peltier elem. + Water	Peltier elem. + Water
Minimum cooling temp. (°C)	−40	−10	−10	+5	+5	+5
Dark current (Electrons/pixel/s)	0.007 @ −40 °C	0.019 @ −10 °C	0.019 @ −10 °C	0.5 @ 5 °C	0.5 @ 5 °C	0.5 @ 5 °C
Full well capacity (Electrons)	30,000	30,000	30,000	30,000	30,000	30,000
Dynamic range (bit)	12/16	12/16	12/16	16	16	16
Global shutter function	○	○	×	○	×	○

(continued)

Table 4.11 (continued)

Hamamatsu Photonics	Thorlabs	Nippon Roper	SPOT IMAGING	FLI		
C13440-20CU	Quantalux CS2100M-USB	KURO 1200B	KURO 2048B	RT	KL400	KL2020
2048 × 2048	1920 (H) × 1080 (V)	1200 × 1200	2048 × 2048	2448 (H) × 2048 (V)	2048 × 2048	2048 × 2048
6.5 × 6.5	5.04 × 5.04	11 × 11	11 × 11	3.45 × 3.45	11 × 11	6.5 × 6.5
Front side	Front side	Front side	Back side	Back side	–	–
82	61	95	95	66	94	62
100	50	41	25	36	48	376
1.4 @ 100 Hz	<1 @ 74.25 MHz	1.3 @ 200 MHz	1.3 @ 200 MHz	2.1	1.5	6
Peltier elem. + Water	- (Heat dissipation structure)	Peltier elem. + Air/Water	Peltier elem. + Air/Water	Peltier elem. + Air cooling	Peltier elem. + Water	Peltier elem. + Water
−30	–	−10/−25	−10/−25	−25	−40	−40
0.006 @ −30 °C	20 @ 20 °C	0.7 @ −25 °C	0.7 @ −25 °C	0.18 @ 20 °C	0.4 @ −20 °C	1 @ 0 °C
30,000	23,000	80,000	80,000	11,000	89,000	48,000
16	16	16	16	12	16	15
×	×	×	×	O	×	O

(a) (b)

Fig. 4.91 Examples of commercially available sCMOS cameras. From Table 4.11, **a** Hamamatsu Photonics ORCA-Flash 4.0 V3 model (C13440-20CU) (courtesy of Hamamatsu Photonics) and **b** ANDOR Neo (right) and Zyla (left) (courtesy of Satoshi Hidaka of Andor Technologies, Ltd.)

to replace image intensifiers. Flat-panel detectors have the advantage of minimal image distortion when compared to image intensifiers, which are the same form of detectors with a large surface area. This is currently an important point, considering the increasing importance of the dimensional measurement applications.

The flat panel detector uses a *thin film transistor* (*TFT*) array, which serves as the backbone of the liquid crystal display. TFT is a type of FET. A semiconducting film is created on a glass substrate, into which transistors used for switching elements, gate insulation films, electrodes, or protective insulation films are incorporated. This manufacturing technique has been used for liquid crystal displays and flat-panel TVs and has been well developed. In a liquid crystal display, the liquid crystal layer is placed between the glass substrates, which comprise the TFT-formed glass substrate and the counter electrode, and the TFT functions as a switch that applies voltage on the liquid crystal in each pixel. Meanwhile, the TFT array in the flat panel detector functions as a two-dimensional readout circuit.

Incidentally, the flat panel detector can be broadly classified between a *direct conversion type* and an *indirect conversion type*. Figure 4.92 shows the mechanisms of both types. The read-out mechanisms are explained in the CMOS section (Sect. 4.4.2 (4)). The two types of photoelectric conversion mechanisms and the materials primarily used for this are detailed below.

The direct conversion type shown in Fig. 4.92a directly converts X-rays into signal charges and images them using a *photoconductive film* comprised of a 0.5–1-mm thick *amorphous selenium* (*a–Se*) semiconductor. The TFT, electrode, and signal charge accumulation condenser are arranged in a matrix form in what is referred to as a TFT array (the halftone dot mesh section in Fig. 4.92) and both the X-ray conversion screen and bias electrode are laminated to cover almost the entirety of the TFT array. The charges of the electron-hole pairs excited in correspondence with the intensity of the incident X-rays are moved to the electrodes of each pixel due to the bias voltage applied in the photoelectric conversion film, after which they are accumulated in the signal charge accumulation condenser within the TFT array. Charge transfer is

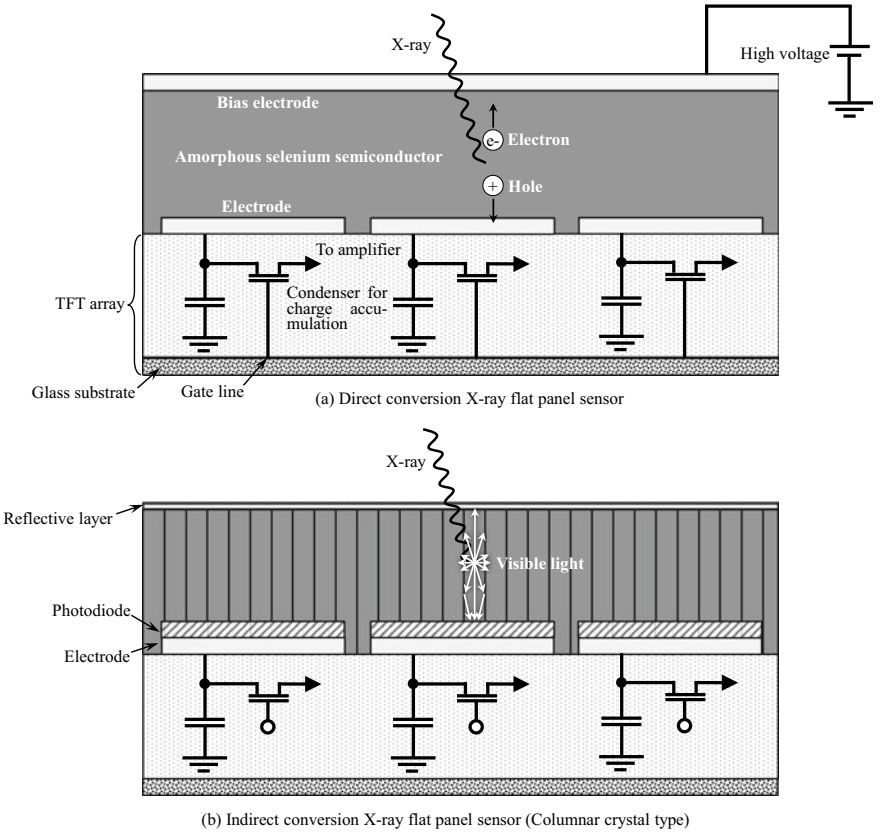

Fig. 4.92 Schematic showing the structures of two representative flat panel detectors

delayed in the direct conversion type due to the presence of energy barriers between each layer and residual images are more likely to appear. However, the structure in which a high voltage is applied, and the charge drawn into the nearest electrode is advantageous in terms of spatial resolution. A two-dimensional X-ray image can be obtained by turning the TFT in each pixel on or off and sequentially reading out the charge voltage of the condenser. This readout is similar to the CMOS camera. The amplification circuit and AD converter are located on the same substrate in the data bus line terminal and the read-out charge information is outputted as digital image information.

The materials used in a photoelectric conversion film are discussed here. *Lead iodide* (PbI_2), *lead oxide* (PbO), and thallium bromide (TlBr) are used as photoelectric conversion materials in addition to amorphous selenium; materials like *cadmium zinc telluride* ($CdZnTe$), *cadmium telluride* ($CdTe$), *cadmium selenide* ($CdSe$), and *mercury iodide* (HgI_2) are also considered promising materials in this regard [68]. Table 4.12 shows the various photoconductors that can be used for large-surface

Table 4.12 Major photoconductors that can be used in flat panel detectors and their specifications [69]

Photoconductor	Decay distance, δ(μm)		E_g (eV)	$W_\pm$ (eV)	$\mu\tau(10^{-5}$ cm^2/V)	
	20 keV	60 keV			Electron	Hole
Amorphous selenium (a-Se)[a]	49	998	2.2	45 (10 V/μm), 20 (30 V/μm)	0.03–1	0.1–6
Polycrystalline silver iodide (HgI_2)	32	252	2.1	5	1–100	0.1–1
Polycrystalline cadmium zinc telluride (Cd0.95Zn0.05Te)[a]	80	250	1.7	5	– 0	– 0.3
Polycrystalline lead iodide (PbI_2)	28	259	2.3	5	0.007	– 0.2
Polycrystalline lead oxide (PbO)[a]	12	218	1.9	8–20	0.05	Small
Polycrystalline Thallium bromide (TlBr)[a]	18	317	2.7	6.5	Small	0.15–0.3

[a]Vacuum deposition; the others: PVD

area applications (e.g. flat panel detectors) and their characteristics [69]. The δ in the table is the *decay distance*, which is the inverse of the linear absorption coefficient. The decay distance corresponds to the depth from the incident surface at which the incident X-ray is 63% attenuated. The quantum efficiency η_q for a photoelectric conversion film of thickness L_p is expressed as follows [69]:

$$\eta_q = 1 - e^{\frac{-L_p}{\delta}} \tag{4.49}$$

Using amorphous selenium with a 1000-μm thickness, for example, Table 4.12 shows that the quantum efficiency at 20 keV becomes 1. Figure 4.93 shows the X-ray energy dependency of the linear absorption coefficients of the various photoconductors shown in Table 4.12 [71]. Considering only quantum efficiency, other photoconductors are superior at X-ray energies below 12 keV. Furthermore, the *stopping power* of lead oxide or thallium bromide is also superior above the K absorption edge of selenium (12.65 keV). Equation (4.49) is as shown below when the X-ray source is not monochromatic [4]:

$$\eta_q = \frac{\int_0^{E_{max}} \Phi(E)\left(1 - e^{\frac{-L_p}{\delta}}\right) dE}{\int_0^{E_{max}} \Phi(E) dE} \tag{4.50}$$

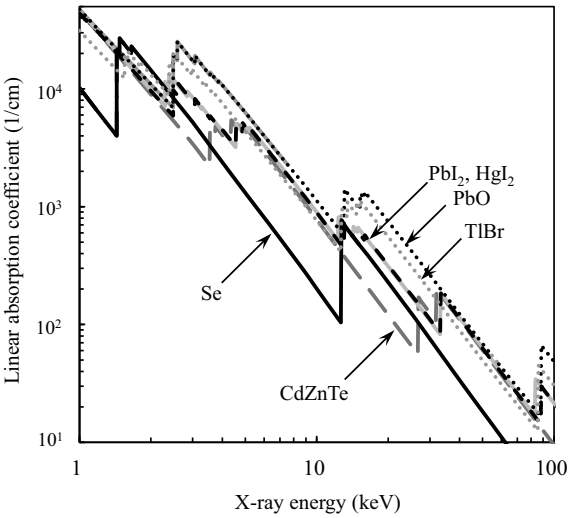

Fig. 4.93 Linear absorption coefficient of various photoconductors, which can be used in applications on large surface areas such as flat panel detectors

Here, $\Phi(E)$ is the X-ray spectrum; in other words, the number of photons entering a detector is not important for a typical X-ray detector but rather the integrated value of X-ray energies entering the detector.

X-ray attenuation is not the only important aspect of photoelectric conversion films. The E_g in Table 4.12 is the band gap. The following relational expression can be established for *electron-hole pair creation energy* $E_{\pm}$ in a polycrystalline material [69]:

$$E_{\pm} = \beta_{lc} E_g \approx 3E_g \tag{4.51}$$

Here, β_{1c} is a constant, typically with a value of 2–3 [72]. The electron–hole pair number $n_{\pm}$ of photoelectric conversion films is equivalent to the incident X-ray energy divided by the electron–hole pair production energy, as shown in Eq. (4.52). For this reason, a narrower band gap is advantageous for quantum efficiency [69].

$$n_{\pm} = \frac{E}{E_{\pm}} \tag{4.52}$$

According to Table 4.12, for example, 1000 electron-hole pairs would be produced for a single X-ray photon of 45 keV in an electric field with strength 10 V/μm.

Meanwhile, as can be observed from Table 4.12, Eq. (4.51) does not hold for amorphous selenium. In this case, the electron-hole pair creation energy is inversely proportional to the electric field F, as shown below [69]:

$$E_{\pm} = E_0 + \frac{B}{F} \tag{4.53}$$

Here, B is a constant that shows a weak dependency on X-ray energy; $B \approx 4.4 \times 10^{8}$ eV·Vm^{-1} and $E_0 \approx 6$ eV in a 20–40 keV range [69]. As such, the electron-hole pair creation energy of amorphous selenium in typically used electric fields (10–20 V/μm) is extremely high, in the order of several dozens of eV. However, high quantum efficiency is obtained owing to the amount of charge produced but also requires that the generated charge does not recombine or become trapped and is efficiently collected at the electrodes. Furthermore, raising the voltage brings this closer to a standard semiconductor. However, an electron avalanche occurs prior to completely returning to normal. In Table 4.12, μ is the drift mobility and τ is the average lifespan of the charge carrier. The term $\mu\tau F$, which multiplies the electric field intensity, is the average mobility distance until the electron carrier is trapped or recombined. The $\mu\tau F$ needs to have a value higher than the photoelectron conversion film thickness for the electrodes to capture most of the generated charge.

Amorphous selenium has the advantages of low-cost, as it can be coated across wide surface areas in a low-temperature process of 60–70 °C and its ability to obtain a homogeneous response [68]. Another major advantage is its low dark current at room temperature and its resistance to radiation damage in experiments. Points of caution are that films need to be somewhat thick against high-energy X-rays given that the atomic number is relatively small ($Z = 34$) and that a high voltage (typically around 10 kV) must be applied [68]. Furthermore, high-purity amorphous selenium is straightforward to crystallize, so a 0.2–0.5% arsenic addition is included [68].

The indirect conversion type in Fig. 4.92b uses a scintillator to convert the X-ray into visible light, and then into a signal charge that corresponds to the intensity of that visible light; that this is stored with the condenser up to readout is the same as with the direct conversion type. With the indirect conversion type, the isotropic generation of visible light with the scintillator results in crosstalk and the potential for reduced spatial resolution. Thicker scintillators, in particular, result in more X-rays being absorbed and worsened spatial resolution. Furthermore, the direct conversion type is advantageous in terms of quantum detection efficiency, as shown in Fig. 4.94 [70].

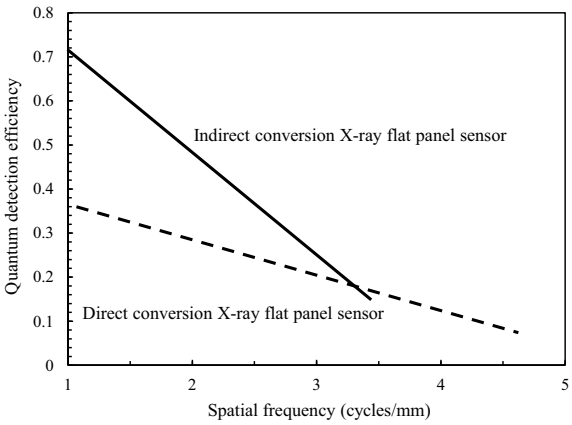

Fig. 4.94 Comparisons of quantum detection efficiency of direct conversion-type and indirect conversion-type flat panel detectors (schematic) [69]

Cesium iodide (*CsI (Tl)*) or *gadolinium oxysulfide* (*GOS*) (Gd_2O_2S *(Tb)*) are used for the scintillator. The powdered form of GOS is referred to as *P43*. Figure 4.95 shows cross-section photographs of these two types of scintillator materials [64]. CsI (Tl) has a primarily columnar crystal structure as seen in Fig. 4.95a) and, depending on the conditions, approximately 83% is reflected within the columnar crystal [68].

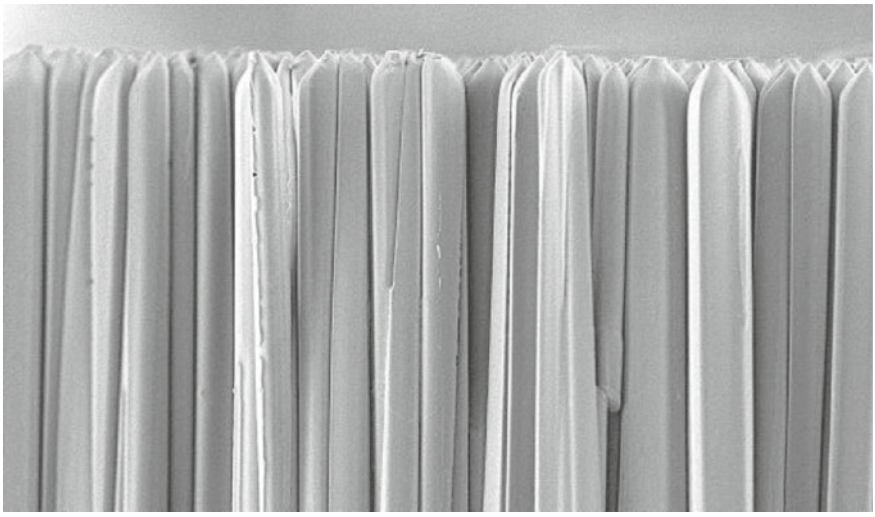

(a) CsI(Tl) scintillator (Columnar crystal)

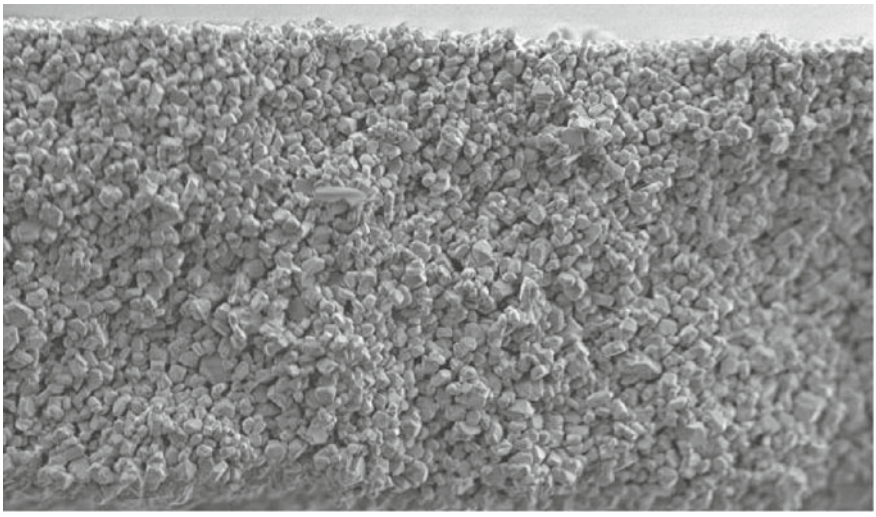

(b) GOS scintillator (Granular crystal)

Fig. 4.95 Cross-section photograph of a scintillator (courtesy of Hamamatsu Photonics) [63]

For this reason, light is guided into the crystal wall and a certain fraction is guided into the photodiode direction. These are referred to as *structured scintillators*. CsI (Tl) scintillator can be deposited on substrates such as glass, which is then flipped and adhered to the photodiode. It can also be deposited directly on the photodiode or deposited on the fiber optic plate (discussed later) [64]. Figure 4.96 shows schematics of their cross-sections and Fig. 4.97 shows examples of commercially available products. Direct deposition suppresses fluorescent scattering and contributes to increased spatial resolution [64]. Furthermore, the columnar CsI (Tl) crystals increase in crystal diameter as the film thickness increases, which can reduce the spatial resolution by coalescence with adjacent crystals. Other points of caution with CsI (Tl) include hygroscopicity, toxicity (particularly the trace thallium iodide (TlI) amounts added as an activator in CsI (Tl)) and its relatively low mechanical strength [68]. Details on scintillation phenomena are discussed later in Sect. 4.4.3.

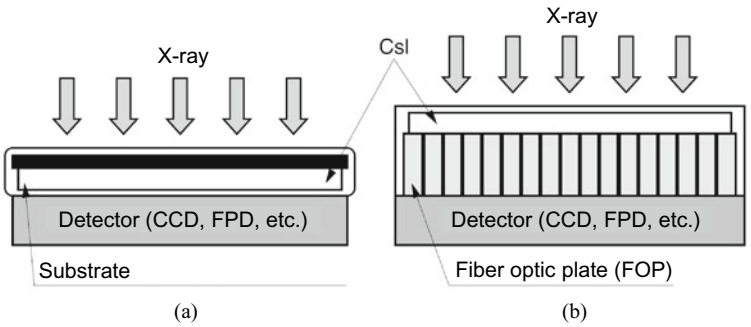

Fig. 4.96 Implementation example when using cesium iodide in a scintillator; **a** is when cesium iodide is deposited on a substrate, after which the substrate is flipped and joined with the detector; **b** is when cesium iodide is deposited on a fiber optic plate which joins the detector and scintillator (courtesy of Hamamatsu Photonics)

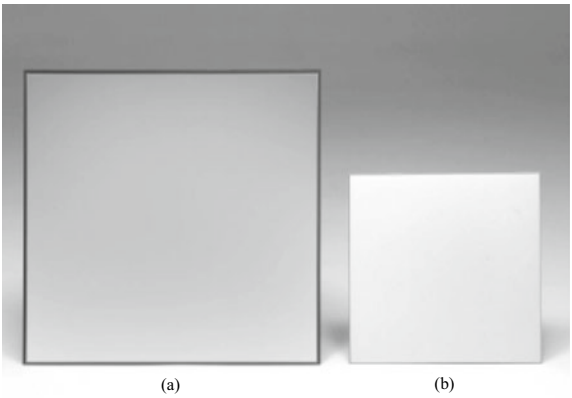

Fig. 4.97 Example of commercially-available cesium iodide scintillator; **a** is when this is deposited on an aluminum or carbon substrate and **b** is when this is deposited on a fiber optic plate (courtesy of Hamamatsu Photonics)

Finally, the specifications of various flat-panel detectors that are commercially available are displayed for reference in Table 4.13. These should be compared with the CCD cameras and EM-CCD cameras in Tables 4.7, 4.8 and 4.9 and the sCMOS

Table 4.13 Representative flat panel detectors that are commercially available and their specifications

Manufacturer	Hamamatsu photonics		Rayence	
Type	C7942CA-22	0505A	1215A	2020A
Number of pixels	2240 × 2344	1176 × 1104	2352 × 2944	1120 × 1120
Pixel size (μm)	50 × 50	49.5	49.5	180
Effective photodetection surface (mm)	112 × 117.2	58 × 54	116.4 × 145.7	201.6 × 201.6
Indirect conversion/direct conversion	Indirect conversion	Indirect conversion	Indirect conversion	Indirect conversion
Photoelectric conversion film/scintillator	Scintillator (CsI)	GOS/CsI	GOS/CsI	GOS/CsI
Read-out rate (Frames/s)	2	30(1 × 1) 90(2 × 2)	8(1 × 1) 32(2 × 2)	30
Read-out noise (Electrons-rms)	1100	<4	<3.4	8
Dark current (Electrons/pixel/sec)	–	403	74	–
Full well capacity (Electrons)	2,200,000	16.384	16.384	32.768
Dynamic range (bit)	–	14	14	16
ANSeeN	Pony industry	Acrorad	Xcounter (Acrorad)	
ANS-FPD4 × 2S01S	SID-A50	FPD4x2	HYDRA FX35	
262,144 pixel	237,568 pixel	237,552 pixel	3584 × 60	
100	100	100 × 100	100 × 100	
51.2 × 51.2	51.2 × 46.4	51.5 × 46.5	360 × 6	
Direct conversion	Direct conversion	Direct conversion	Direct conversion	
CdTe	CdTe	–	–	
200	5–50 (1:1)	50	200 (Frame mode) 10,000 (TDS mode)	
45,000	–	–	–	
250 fA	–	–	–	
20,000,000	–	–	–	
14	12	12	12 (Frame mode) 18 (TDS mode)	

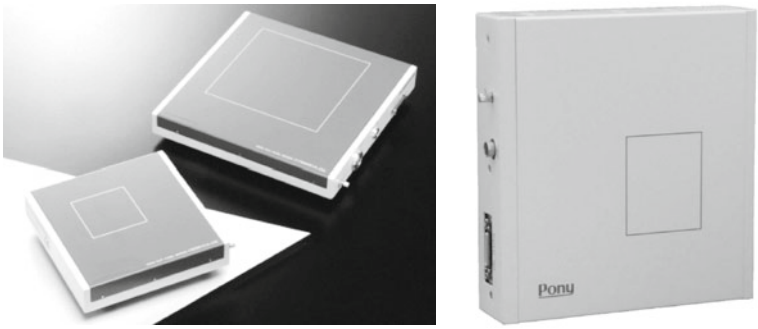

(a) (b)

Fig. 4.98 Example of commercially available flat panel detectors; **a** Hamamatsu Photonics product (courtesy of Hamamatsu Photonics) and **b** Pony Industry SID-A50 model (courtesy of Toshiro Yamazaki of Pony Industry)

cameras in Table 4.11. Furthermore, Fig. 4.98 shows a photograph of the external appearance of a commercially available flat-panel detector.

4.4.3 Scintillator

(1) Emission Mechanism

Scintillators can be organic, plastic, or inorganic. Organic materials include naphthalene ($C_{10}H_8$), anthracene ($C_{14}H_{10}$), and trans-stilbene ($C_{14}H_{12}$). Each of their effective atomic numbers, as well as their densities, are small, measuring at around 1 g/cm^3. Their characteristics include a decay time of several ns, which is shorter than that of inorganic materials (discussed later), and low cost. Furthermore, their light emission is relatively weak compared to scintillators made of inorganic materials and their stopping power is considerably inferior, as shown in Fig. 4.99 [71]. Liquid scintillators are organic scintillators that have been dissolved in a toluene or xylene solvent. Plastic scintillators are organic scintillators that have been dissolved in plastics, such as polystyrene. These are suited for alpha- and beta-ray detection but are not used often for X-ray imaging. With this in mind, a discussion on scintillators made with inorganic materials, which is important when discussing X-ray tomography, is presented below. Generally, light emission is stronger in inorganic materials, stopping power is high as in Fig. 4.99, and linearity with regard to energy is favorable.

Light emission from inorganic materials can be explained using their discrete energy band; Fig. 4.100 shows a schematic of this. When an X-ray is irradiated on the scintillator material, the electron in the *valence band* leaves a hole in that band and is excited to the *conduction band*; a forbidden band is present between the two,

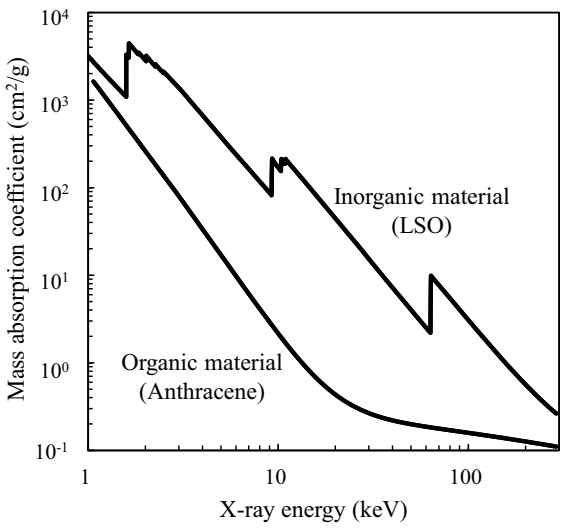

Fig. 4.99 X-ray energy dependencies of mass absorption coefficients in representative organic and inorganic material scintillators [3]; anthracene and LSO are shown as organic and inorganic materials, respectively

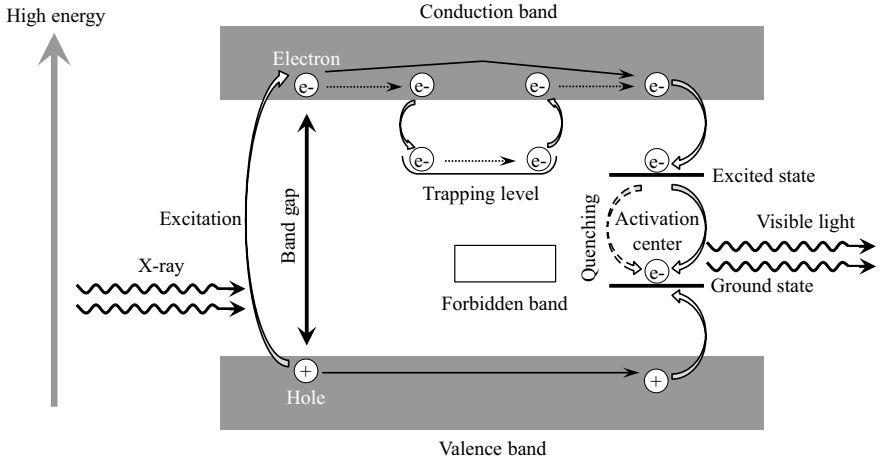

Fig. 4.100 Schematic showing the light emission mechanism in an inorganic material scintillator

where the electrons cannot exist in pure crystals. When the excited electron drops back down to the valence band and rejoins the hole, the excess energy corresponding to the band gap between the valence and conduction bands is radiated through photon discharge.

The maximum wavelength of the emission spectra is generally located in the long-wavelength side (low-energy side) relative to the maximum wavelength of the absorption spectra. This phenomenon where the incident radiation and generated radiation have different energies is referred to as *Stokes shift*. This occurs because

excitation is the transition from the lowest ground state to the excited state, whereas light emission corresponds to the transition from the lowest vibrational state of the first excited state to the ground state. The generated wave can be radiated externally without being absorbed into the scintillator material through the Stokes shift. Furthermore, a larger Stokes shift results in a smaller overlapping of the incident wave and generated wave spectra; the self-absorption of the generated wave due to the scintillator also decreases.

Scintillator materials, which use the light emission from wide band gap materials with no *activator* addition, include *cadmium tungstate* ($CdWO_4$) (CWO), *barium fluoride* (BaF_2), and *bismuth germanium oxide* ($Bi_4Ge_3O_{12}$) (BGO). The light emission efficiency in these cases is generally low and the discharged energy is too large for visible light emission. The light emission mechanism in the slow-decay components of barium fluoride or cesium iodide with no activator additions is from *self-trapped excitons*, which are excitons trapped in crystal lattices that have been strained due to interactions between excitons and the lattice. The fast-decay components of barium fluoride are due to the *core-valence luminescence* (*CVL*) generated when the valence electron transitions into the core level with the lowest binding energy. This light emission has an extremely low lifespan at the ns order and is effective as a light emission mechanism of a high-speed scintillator. Furthermore, the WO_4^{2-} ions in cadmium tungstate are the center of light emission and the *charge transfer* transitions between the 2p orbitals of tungsten and its surrounding O^{2-} oxygen ions.

Scintillators that efficiently emit visible light are those that have activator doping. These types of scintillator materials have rare-earth elements like cerium (Ce), terbium (Tb), and europium (Eu), as well as thallium (Tl) and sodium (Na) ions, which act as *luminescent centers* within the forbidden band. Scintillator materials that have activator additions include CsI (Tl) and *yttrium aluminum garnet* ($Y_3Al_5O_{12}$) (*YAG*: Ce^{3+}). As shown in Fig. 4.100, the electrons in the conduction band arrive at the activation center while being trapped at the trap centers when activators are added. The electron is positioned at the excited level of the activator and holes in the valence band take trapped electrons at the ground level from the activation center, creating a vacancy. Visible light is then emitted by an electron in the excited state transitioning into this vacancy. Figure 4.101 shows the wavelength at which cesium iodide emits light [74]. As pure cesium iodide emits near-ultraviolet light, the emission can then be adjusted to the visible light range by doping with sodium to shift this to a 430 nm range or with thallium to reach a longer wavelength in the 550 nm range. Furthermore, the addition of activators has a large influence on light emission efficiency.

High-efficiency light emission accompanying the allowable 5d–4f transition occurs in trivalent rare-earth ions such as the representative activator cerium and further decays within a short period [75]. There are divalent and trivalent forms of the europium ion and its ratio varies with concentration. The decay time is longer

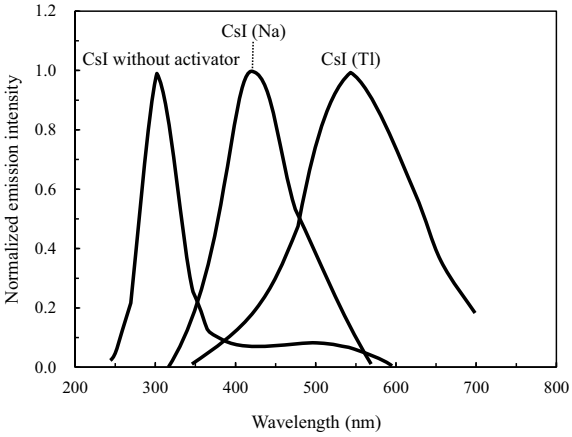

Fig. 4.101 Schematic showing the wavelength spectra of visible light irradiated by scintillators with pure cesium iodide or cesium iodide with sodium or thallium doping [73]

compared to cerium during light emission accompanying 5d–4f transitions in divalent rare-earth ions such as Eu^{2+} [75]. Meanwhile, light emission accompanying 4f–4f transitions in trivalent rare-earth ions such as Eu^{3+} is both a parity-forbidden transition and a spin-forbidden transition and its fluorescence time increases [75]. Furthermore, thallium is classified into light emission accompanying 6s6p–6s transitions [75].

Here, the following equation can be obtained from Eqs. (4.51) and (4.52) by setting the number of generated photons as N_{scin} and the number of electron-hole pairs as $n_{\pm}$ [72]:

$$N_{scin} = n_{\pm}\eta_{lc}\eta_q^{lc} = \frac{E}{E_{\pm}}\eta_{lc}\eta_q^{lc} = \frac{E}{\beta_{lc}E_g}\eta_{lc}\eta_q^{lc} \tag{4.54}$$

η_{1c} and η_q^{1c} are the efficiency of light emission center excitation and quantum efficiency of the light emission center, respectively. η_q^{1c} is dependent on the positional relationship of the energy band of the scintillator material and the light emission center energy level and η_{1c} is dependent on the trapping center [72]. The intensity of the visible light emitted from the scintillator needs to consider the percentage of X-rays, which transmit through the scintillator, and the absorption of the generated visible light by the scintillator itself.

(2) Characteristics Assessment

Representative inorganic scintillators and their various characteristics are summarized in Table 4.14 [76, 77].

(a) Stopping Power

The density and *effective atomic number* in the table are related to the detection efficiency and stopping power. The effective atomic number Z_{eff} is an effective parameter that expresses the attenuation behavior of the X-rays illuminated on compounds. This

Table 4.14 Representative materials for scintillators and their characteristics

Substance	Density (g/cm^3)	Effective atomic number	Refractive index	Emission peak wavelength (nm)	Photon yield (Photons/keV)	Decay time (ns)	Decay distance (μm)	
							20 keV	60 keV
BaF_2[a]	4.89	53	1.56	310	9.5	630	40	125
$Bi_4Ge_3O_{12}$ (BGO)[a]	7.13	75	2.15	480	8.2	300	9	150
$CdWO_4$[a]	7.90	64	2.25	470	13	12	14	137
NaI (Tl)	3.67	50	1.85	415	38	230	56	173
CsI (Tl)	4.51	54	1.80	540	65	1100	37	115
CsI (Na)	4.51	54	1.84	420	39	650	37	115
LiI (Eu)	4.08	52	1.96	470	11	1400	46	139
CaF_2 (Eu)	3.19	13	1.47	435	24	900	193	3024
$LaBr_3$ (Ce)	5.29	46	2.05	380	63	26	19	157
$YAlO_3$ (Ce) (YAP)	5.37	35	1.95	370	18	27	22	382
$Y_3Al_5O_{12}$ (Ce) (YAG, P46[b])	4.56	32	1.82	550	17	70	30	530
Lu_2SiO_5 (Ce) (LSO)	7.40	66	1.82	420	25	47	13	218
Gd_2SiO_5 (Ce) (GSO)	6.71	59	1.85	440	9	60	20	69
$LuAlO_3$ (Ce) (LuAP)	8.34	65	1.94	365	17	17	14	234

(continued)

Table 4.14 (continued)

Substance	Density (g/cm^3)	Effective atomic number	Refractive index	Emission peak wavelength (nm)	Photon yield (Photons/keV)	Decay time (ns)	Decay distance (μm)	
							20 keV	60 keV
$Lu_3Al_5O_{12}$ (Ce) (LuAG)	6.73	63	1.84	550	20	58	18	291
$Gd_3Al_2Ga_3O_{12}$ (Ce) (GAGG)	6.63	52	1.93	520	57	88	21	95
$Gd_3Ga_5O_{12}$ (Eu) (GGG)	7.1	53	1.96	595	44	140000	19	93
Gd_2O_2S (Tb) (P43[b] or Gadox)	7.34	60	2.2	545	60	1500	17	56
$Lu_3Al_5O_{12}$ (Pr) (LuAG)	6.71	63	1.84	310	16	26	18	292

[a]Without activator
[b]Designation for powder

is expressed as follows, where the ratio between the sum of electrons in the compound and the electron number of the *i*th element, which comprises the composite is set as f_i and the atomic number of the *i*th element is set as Z_i.

$$Z_{eff} = \sqrt[\delta]{\sum_i f_i Z_i^{\delta}} \tag{4.55}$$

The coefficient δ in the equation is equal to 2.94 when photoelectric absorption is predominant. Meanwhile, this value is 3–3.5 when the X-ray energies are in the range 100–600 keV where Compton scattering is predominant [78]. For example, water is comprised of hydrogen (atomic number 1) and oxygen (atomic number 8) and its effective atomic number is $\sqrt[2.94]{0.2 \cdot 1^{2.94} + 0.8 \cdot 8^{2.94}} \approx 7.4$. The decay distances for the two standard X-ray energies of 20 keV and 60 keV are shown in Table 4.14. This decay distance becomes an index for stopping power. Detector efficiency decreases when a scintillator with a thickness smaller than the decay distance is used. Furthermore, the spatial resolution of the X-ray CT scanner decreases when a scintillator with a thickness greater than the decay distance is used.

(b) Emission Wavelength

The *emission peak wavelength* and *photon yield* are both quantities relating to the sensitivity of the detection system. The emission peak wavelength of the scintillator generally needs to be matched with the spectral response characteristics of the photoelectric surface on the visible light detector. The efficiency of the detection system can be optimized in this manner. As previously discussed, the emission peak wavelength of the scintillator can be controlled by changing the type of activator used.

(c) Photon Yield

The photon yield L_y, which expresses the sensitivity of the scintillator, is expressed by the amount of emitted light per unit absorption energy as follows using Eq. (4.54). The units are in photon number/keV or photon number/MeV.

$$L_y = \frac{N_{scin}}{E} = \frac{\eta_{lc} \eta_q^{lc}}{\beta_{lc} E_g} \tag{4.56}$$

In other words, the photon yield is superior for materials with narrower band gaps. Band gap energies of pure substances without activator additions generally decrease in the order of fluorides, oxides, chlorides, bromides, and iodides [79]; thus, higher photon yields can be expected with materials further down this list [79]. Equation (4.51) confirms that the electron-hole pair creation energy $E_{\pm}$ in various photoelectric conversion materials satisfies the relationship $E_{\pm} = \beta_{1c} E_g \approx 3E_g$. Reports have indicated that this coefficient β_{1c} is 3 for *sodium iodide* (*NaI*), 5.6 for YAG, and 7 for *calcium tungstate* ($CaWO_4$) [80]. Slight undulations in photon yield are not frequently problematic in standard X-ray microtomography, but in contrast,

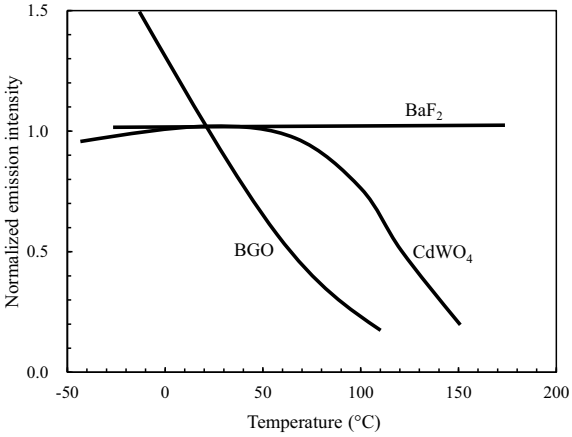

Fig. 4.102 Temperature dependencies of normalized light emission intensities of visible light emitted by scintillators comprising cadmium tungstate ($CdWO_4$), bismuth germanium oxide (BGO), and barium fluoride (each shown in Table 4.14) [80]

the linearity of photon yield to X-ray energies is important. Figure 4.102 shows the temperature dependencies of photon yield for several scintillators [81]. There are many scintillators whose light emission intensity decreases with increases in temperature, while there are some such as BGO in the figure, which vary widely, even near room temperature. Furthermore, there are those that peak within a range of approximately 80 °C from room temperature (in the case of sodium-activated cesium iodide [79]).

(d) Refractive Index

The refractive index is a necessary material characteristic when there are mismatches in scintillator material/detector junctions, which may be made of glass fibers or others. For example, as discussed later, if the refractive index n_2 of core fiber material is approximately 1.8, the refractive index of the scintillator should also be set to approximately 1.8 to prevent loss at the junction surface.

(e) Rise Time and Decay Time

The decay time τ_d expresses the time necessary for the decay of light emission intensity, which is important for applications in high-speed imaging. This is the time necessary for an electron to return to the ground state from the excited state. The decay time generally follows the law shown below and has the relationship $\tau_d \approx \lambda^2$ [80]:

$$\tau_d = \frac{cm\lambda^2}{8\pi e^2 f n_{scin}} \left(\frac{3}{n_{scin}^2 + 2} \right)^2 \tag{4.57}$$

Here, c is the speed of light, m is the electron mass, λ is the wavelength, n_{scin} is the refractive index of the scintillator material, and f is the vibrator strength of the transition; in other words, scintillators that emit ultraviolet light and purple visible

light are suited for high-speed imaging. Furthermore, the light emission intensity $I(t)$ of the scintillator expresses decay following an exponential function, as in the following equation:

$$I(t) = I_0 e^{\left(\frac{-t}{\tau_d}\right)} \tag{4.58}$$

Here, I_0 is $I(t)$ at time $t = 0$. For example, the decay time of thallium-activated cesium iodide is approximately 1100 ns according to Table 4.14 but the rise time is about 2 orders of magnitude smaller at approximately 20 ns. For this reason, the decay time is a larger issue in actual practice. Increases in activator concentration also decrease the rise time [79]. As shown in Table 4.14, scintillators with thallium doping have a high photon yield but a lengthy decay time. Meanwhile, those with cerium doping have a comparatively shorter decay time. Actual decay behavior data with *gadolinium aluminum gallium garnet* (*GAGG (Ce)*) ($Gd_3Al_2Ga_3O_{12}$) as an example are shown in Fig. 4.103.

Generally, a single scintillator material also has multiple metastable states, and the reported decay times shown in the data in Table 4.14 are the result of adding these together. In actual practice, the scintillation of several inorganic scintillators are the sum of the fast-decay component and slow-decay component. This type of decay behavior is schematically shown in Fig. 4.104. When considering the decay behavior in such cases, Eq. (4.58) should be summed as a percentage of the intensities of each material, as shown in the following equation:

$$I(t) = I_0^f e^{\left(\frac{-t}{\tau_d^f}\right)} + I_0^s e^{\left(\frac{-t}{\tau_d^s}\right)} \tag{4.59}$$

Here, the superscripts f and s each express the fast and slow components, respectively. For example, barium fluoride has fast components of 0.8 ns in addition to the

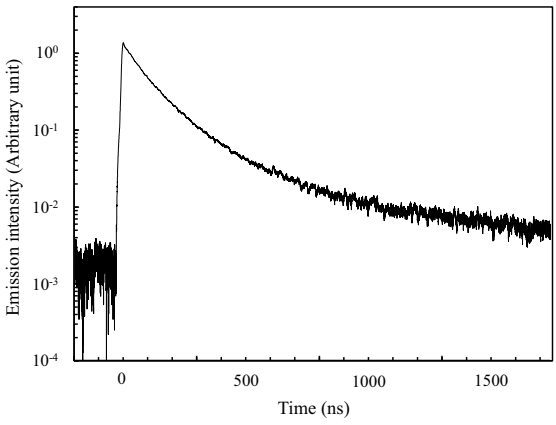

Fig. 4.103 GAGG (Ce) decay properties (courtesy of Hiroki Sato of Furukawa Scintitech)

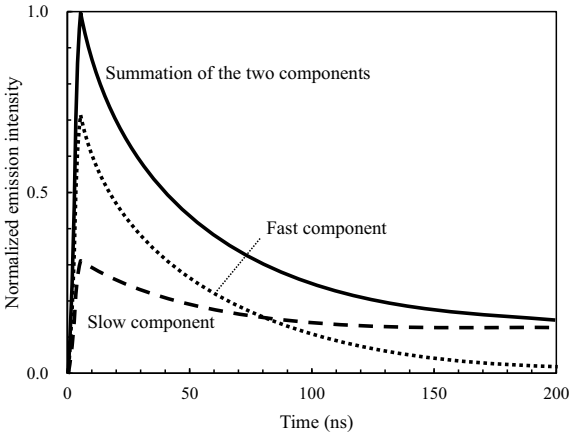

Fig. 4.104 Schematic of light emission behavior in scintillator materials comprising components with fast and slow light emission decay

slow components of 630 ns shown in Table 4.14; thallium-activated cesium iodide has a fast component of 3.34 ns as well [79].

(f) Afterglow

The phenomenon referred to as *afterglow* is phosphorescence that occurs due to the thermal release of electrons from a trap and can last as long as several ms. The origin of the trap is from crystal defects and impurities and its extent varies widely even in the same material according to its manufacturing process or heat treatment. This can also depend on impurity element concentration. The extent of afterglow can also vary widely depending on the material; for example, thallium-activated sodium iodide reaches a maximum of 5% after 6 ms of elapsed time, whereas this can be constrained to 0.005% for BGO (after 3 ms elapsed time) [79].

As decay and afterglow both result in time lags during imaging, this can be a problem when trying to achieve a high frame rate. Furthermore, afterglow results in the decreased dynamic range of the detector and is thus an important characteristic in X-ray tomography.

(g) Miscellaneous

Although not shown in a table, the form in which a scintillator can be used (e.g. whether it is a powder, bulk crystal, or thin film) is also important. For example, GOS scintillators are network-like thin films in which a binder is added to a powder and consolidated so that it can be formed to a thickness of approximately 5–100 μm. The packing fraction in this case is considerably lower than 1. Crystals or thin films are used in other materials. Thin films are used as a general rule for microtomography to avoid worsening spatial resolution. A film thickness that corresponds to the necessary spatial resolution must be used. Thin-film fabrication includes pulse laser deposition, spattering methods, liquid-phase epitaxial methods, sol-gel methods, and

cutting/polishing methods. Furthermore, columnar crystals can be formed to increase the spatial resolution, as in the cesium iodide introduced in Sect. 4.4.2 (5).

Localized debonding can occur due to long-term X-ray irradiation when a thin film is created on a substrate, which can result in visible irregularities in the image. This ease by which scintillator damage can occur is also a problem in actual practice. Moreover, materials like sodium iodide, *lithium iodide* (*LiI*), cesium iodide, and lanthanum bromide ($LaBr_3$) have hygroscopic and deliquescent characteristics. For this reason, these are made commercially available by being placed in a case and cut off from the atmosphere, as shown in Fig. 4.105.

(3) Characteristics of Various Scintillator Materials

(a) Thallium-activated Sodium Iodide

The fact that thallium-activated sodium iodide is a scintillator material with a high photon yield was discovered in 1948 by the U.S. physicist Hofstadter, who later won the Nobel Prize in Physics for his research on high-energy electron scattering with linear accelerators. Sodium iodide is an ion crystal with a sodium chloride-type crystal structure, whose {100} plane is the *cleavage* plane, exhibiting brittle fracture. Today, many scintillator materials, which are superior in terms of photon yield, have been discovered and applied to actual practice, as shown in Table 4.14. However, large-scale crystals can be fabricated inexpensively using the Bridgman-Stockbarger method and currently sodium iodide remains widely used for gamma cameras. In addition to the components with a 230-ns decay time, as shown in Table 4.14, slow components with a 150-ms decay time are included at a percentage comprising 9% of the total photon yield [76]. Sodium chloride without an activator has a short decay time at approximately 100 ns but its photon yield is low. However, cooling this to liquid nitrogen temperatures generates photon yields that are at the same level as thallium-activated materials at room temperature [76].

(b) Thallium- or Sodium-Activated Cesium Iodide

Fig. 4.105 Example of a commercially available inorganic scintillator; Saint-Gobain lanthanum bromide scintillator (courtesy of Seiko EG & G)

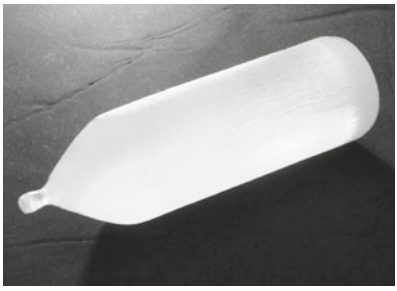

(a) GAGG (Ce) ingot grown by the Czochralski method

(b) LuAG (Pr) ingots grown by the Czochralski method

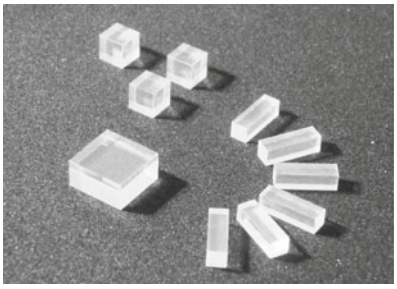

(C) GAGG (Ce) scintillator cut down from an ingot

Fig. 4.106 Examples of commercially available inorganic scintillators. Furukawa Scintitech GAGG (Ce) and LuAG (Pr) (courtesy of Hiroki Sato of Furukawa Scintitech)

The ion radius of cesium is larger than sodium and cesium iodide has a cubic crystal structure in which the fluoride ions are at the corner of the cube and the cesium ion is in the center. This structure does not have any cleavage planes and exhibits some degree of flexibility. It is also easier to handle due to its weaker deliquescence compared to sodium iodide. Sodium iodide and cesium iodide both have a reduced photon yield at X-ray energies lower than 10 keV. The photon yield of cesium iodide in particular rapidly decreases [76]. This has the characteristic of having a lengthy decay time even after undergoing thallium or sodium doping. Meanwhile, the photon yield without any doping drops to 1/10 or lower but the decay time shortens by several dozen factors to approximately 10 ns.

Cesium iodide uses an aluminum or amorphous carbon substrate and depositing on these can form a columnar crystal, introduced in Sect. 4.4.2 (5). For this reason, they are often used in flat-panel detectors. Please refer to Sect. 4.4.2 (5) for other characteristics.

(c) Europium-Activated Lithium Iodide

The two isotopes ^{6}Li and ^{7}Li are present in europium-activated lithium iodide. Although the abundance ratio of ^{6}Li is 7.5%, reactions occur between ^{6}Li and thermal neutrons, therefore, europium-activated lithium iodide is important for the detection of thermal neutrons.

(d) Europium-Activated Calcium Fluoride and Barium Fluoride

Europium-activated *calcium fluoride* (CaF_2) is produced naturally as fluorite. It has the characteristics of phosphorescence and light emission with the application of heat. It has a fluorite-type cubic crystal structure in which fluoride ions fit inside the tetrahedral gaps of the face-centered cubic lattice made of calcium ions. Calcium fluoride is used with europium doping as a scintillator material. Calcium fluoride has low stopping power and a significantly long decay time due to its small effective atomic number. Furthermore, its cleavage plane is the {111} plane and it is easily susceptible to brittle fracture. For these reasons, its range of applications is relatively narrow [76]. Moreover, as it has no deliquescence and low vapor pressure, it can be used in special environments such as vacuum.

There were several publications on barium fluoride in the 1980s. It has a fluorite-type structure similar to calcium fluoride and its cleavage planes are the same. It is fabricated through the Bridgman-Stockbarger method. This material is used as a scintillator without an activator, and as an optical material for high-output infrared lasers; it is also known to be deliquescent. For a scintillator, in addition to the slow-decay component shown in Table 4.14, the extreme fast-decay (0.6 ns) component exists at 20% intensity in the ultraviolet wavelength range [76, 82]. The former is due to light emission from self-trapped excitons and the latter is due to Auger-free luminescence. The presence of the slow-decay component hinders the application of this fast-decay component and large effective atomic number. Heating barium fluoride to 200 °C reduces the peak intensity of the slow-decay component to below 1/10 its original value, whereas the fast-decay component has no temperature dependency and is virtually unchanged. Reports have also indicated applications of these characteristics.

(e) Cerium-Activated Lanthanum Bromide

Of the crystals that use lanthanoids, the only elements that are transparent and emit light under bulk conditions are lanthanum, gadolinium, and lutetium. Lanthanum bromide was reported in 2002 by van Loef of the Netherlands [83]. Alongside *gadolinium gallium garnet* ($Gd_3Ga_5O_{12}$) (*GGG*) and *lutetium oxyorthosilicate* (Lu_2SiO_5) (*LSO*), these new scintillator materials have been developed from the 1990s to the 2000s [84]. Lanthanum bromide has a hexagonal crystal structure referred to as a UCl_3 type. This has a high photon yield, short decay time, and some degree of stopping power. Therefore, it is considered a superior scintillator material with regard to its high-speed response. It has further advantages of not being dependent on temperature and having a virtually fixed photon yield.

Cerium-activated *lanthanum chloride* ($LaCl_3$ (Ce)), which is also a halide-group crystal, has the same type of crystal structure as lanthanum bromide and is a scintillator material with a similar short light emission lifespan, high density, and high photon yield.

Although this material has no cleavage planes, it has a deliquescence that is even stronger than sodium iodide [76], therefore, it needs to be used while sealed in a case

made of materials such as aluminum. Furthermore, thermal stresses are generated during heating and cooling due to the anisotropy of the hexagonal crystal, which can result in its fracture. Care must be taken with compounds that include lanthanum as 789 keV and 1436 keV γ-rays are emitted from naturally-occurring ^{138}La, which has an abundance of 0.09% [84]. Furthermore, α-rays emitted from ^{227}Ac, which cannot be removed even with lanthanum refining, form a continuous spectrum between 1850–3000 keV [84]. Care must also be taken with regard to the usage of lanthanum given that their Kα-rays are 33.436 keV.

(f) BGO

All scintillator materials discussed from here onwards are oxides. The hygroscopic properties, strength, and toughness of these materials are mostly stable compared to the iodides discussed above. BGO, which was discovered in 1973 by Weber et al., does not use any activators and functions as a scintillator through the energy transitions of the bismuth ions (Bi^{3+}) itself. Its effective atomic number is the highest among those shown in Table 4.14 and it has superior stopping power. Furthermore, it has minimal afterglow. However, its photon yield is the lowest among those shown in Table 4.14 and its refractive index is considerably high. In addition, it is difficult to obtain a flat surface with BGO; [76] it has the added disadvantage of a lengthy decay time. As seen in Fig. 4.101, its light emission intensity has a strong temperature dependency and its photon yield further decreases under high temperature. Meanwhile, cooling it to liquid nitrogen temperatures enables it to function effectively as a scintillator [76]. Therefore, its usage is limited to specialized uses with high-energy X-rays or γ-rays. It is fabricated through the Czochralski method, after which it is cut and polished.

(g) Cerium-Activated Perovskite-Type Aluminum Composite Oxides ($ReAlO_3$)

Yttrium aluminum perovskite ($YAlO_3$) (*YAP*) and *lutetium aluminum perovskite* ($LuAlO_3$) (*LuAP*) belong to these groups. These have a perovskite structure similar to barium titanate ($BaTiO_3$). One type of metallic atom is present in each vertex of the unit lattice of the orthorhombic crystal, another type of metallic atom is located on the body center of the unit lattice, and the oxygen is located in the face-center of the cubic crystal.

YAG (Nd), which has neodymium doping, is the most often used with industrial-use lasers, but YAP (Nd) also has similar applications. As a scintillator material, YAP (Ce) has the advantages of a shorter decay time and shorter emission peak wavelength compared with those of YAG (Ce). LuAP (Ce), which exchanges yttrium with lutetium, has an effective atomic number that increases by a factor of about two, giving it superior stopping power. This material was first reported by Moses et al. in 1995. This has an even shorter decay time when compared to YAP (Ce), as well as a feature where the fast-decay component with a decay time of 17 ns, shown in Table 4.14, comprises 80% of the total light emission intensity [76]. However, care must be taken in that lutetium exists in the form of naturally-occurring ^{175}Lu, which is stable and has an abundance of 97.41%, but also radioactive ^{176}Lu, which has an

abundance of 2.59% and a half-life of 3.8×10^{10} years. There have also been reports on $Lu_xY_{1-x}AlO_3$ that replace a part of lutetium with yttrium to stabilize the crystal growth process. However, these have also indicated a problem wherein the generated light is absorbed within the scintillator material interior due to this replacement [76].

(h) Garnet-Type Aluminum Complex Oxide ($Re_3(Al, Ga)_5O_{12}$、$Re_3Al_2Ga_3O_{12}$)

YAG and *lutetium aluminum garnet* ($Lu_3Al_5O_{12}$) (*GGG*), LuAG, and GAGG belong to this group. YAG (Ce) was reported in 1967 by Blasse et al. and is a scintillator material that has seen widespread use. A garnet structure has a cubic unit lattice with eight unit-lattices of $A_3B'_2B''_3O_{12}$, where ion A is a dodecahedral coordination, ion B' an octahedral coordination, and ion B″ a tetrahedral coordination. In the case of YAG, the A site is the yttrium ion and the B′ and B″ sites are aluminum ions. Lutetium is used in place of yttrium for LuAG. Care must be taken for radioisotopes for this reason, as mentioned above. Furthermore, GGG has gadolinium and gallium placed instead of the yttrium and aluminum, respectively, in YAG. Furthermore, GAGG has aluminum present in the B' ion of GGG.

As shown in Table 4.14, garnet-type aluminum composite oxides have an extremely long light emission peak wavelength and a relatively small refractive index. As observed in the spectral response characteristics of the CCD camera shown in Figs. 4.61 and 4.80, there are many detectors with a quantum efficiency peak of approximately 600 nm or higher. The garnet-type aluminum composite oxide is considered advantageous in such circumstances. Figure 4.107 shows the light emission spectra of GAGG (Ce) as examples. YAG is also used in the form of powder with a diameter up to 1 μm, referred to as *P46* in these cases. Compared with P43 (discussed later), this has the characteristics of short decay time and long light emission peak wavelength. Furthermore, those with praseodymium (Pr) doping instead of cerium have an even shorter light emission wavelength. As shown in Eq. (4.57), Pr-doping considerably reduces the decay time, making it a scintillator material even more suited for high-speed applications; LuAG (Pr) is shown as an example of this in Table 4.14. LuAG has a superior stopping power than YAG (Ce) and the superiority of both GGG (Eu) and GAGG (Ce) increases with higher energy. Meanwhile, YAG (Ce), LuAG (Ce), and LuAG (Pr) all have average photon yield levels, as can be observed in Table 4.14. GGG (Eu) and GAGG (Ce) levels are several times higher and are considerably more favorable.

Compared to YAG (Ce), GGG (Eu) has the characteristics of a shorter afterglow and a considerably higher dynamic range, with values between 16–17 bits in the detector as opposed to the 10 bits of YAG (Ce) [85]. However, the disadvantage of an extremely long decay time exists. Generally, materials doped with cerium have a shorter decay time than those doped with europium and are suited for microtomography cases where the number of projections is large and short exposure time is required.

As shown in Fig. 4.106, a single crystal is obtained using the Czochralski method and then fabricated after cutting and polishing when a bulk scintillator is necessary. Meanwhile, reports have indicated examples with LuAG (Ce) where a 2.9 μm-thick

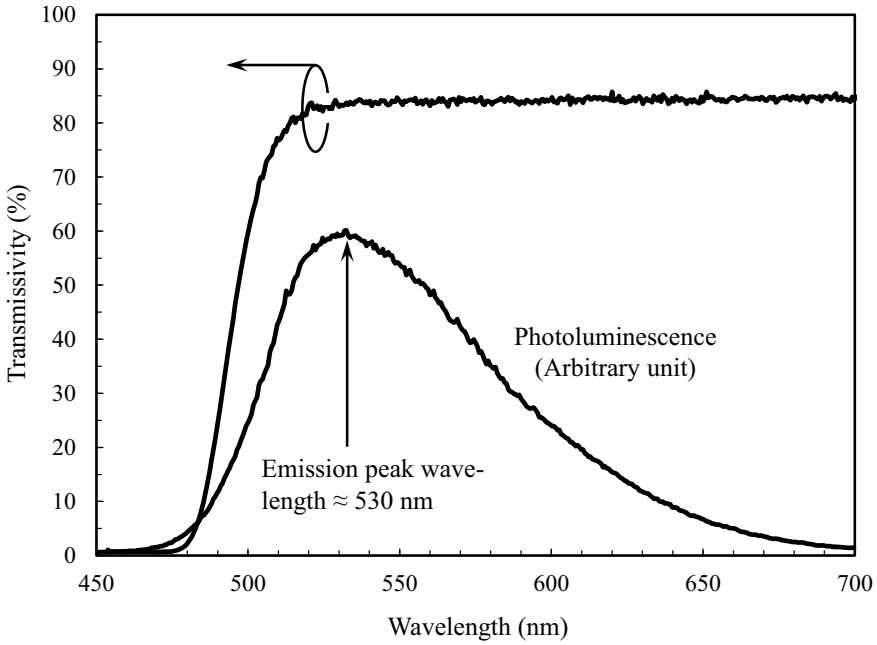

Fig. 4.107 Transmissivity and light emission spectrum of GAGG (Ce) (5-mm thickness) (courtesy of Hiroki Sato of Furukawa Scintitech)

LuAG (Ce) film with 0.07% Ce-doping was attached on top of a 150-μm-thick YAG substrate [86]. Approximately 3% of europium is needed for GGG (Eu) and reports have indicated examples where a 2-μm thick film is deposited on a 170-μm GGG substrate with no activator [86]. A similar procedure is also used for GAGG (Ce), where single-crystal films are created for both using a liquid-phase epitaxial method [86]. A 1–25-μm thick thin-film scintillator material often comprises thin films according to the necessary spatial resolution or the X-ray energy used on the transparent substrate. Having a lattice constant mismatch between the substrate and scintillator material less than 1% is important in forming a high-quality scintillator layer.

(i) Rare-Earth Silicates (Re_2SiO_5)

These correspond to LSO, *gadolinium oxyorthosilicate* (Gd_2SiO_5) (*GSO*), and *yttrium oxyorthosilicate* (Y_2SiO_5) (*YSO*); $Re^1_xRe^2_{(2-x)}SiO_5$-type LGSO and LYSO also belong to this group. GSO (Ce) crystals have a light-yellow color when Ce concentrations are high. Takagi and Fukazawa from Hitachi Chemical, Co., Ltd. showed in 1983 that GSO (Ce) could be used as a scintillator by trace additions of zirconium [87]. Afterward, Melcher from Schlumberger Ltd. reported in 1992 on an LSO (Ce) scintillator that replaced gadolinium with lutetium [88]. Compared

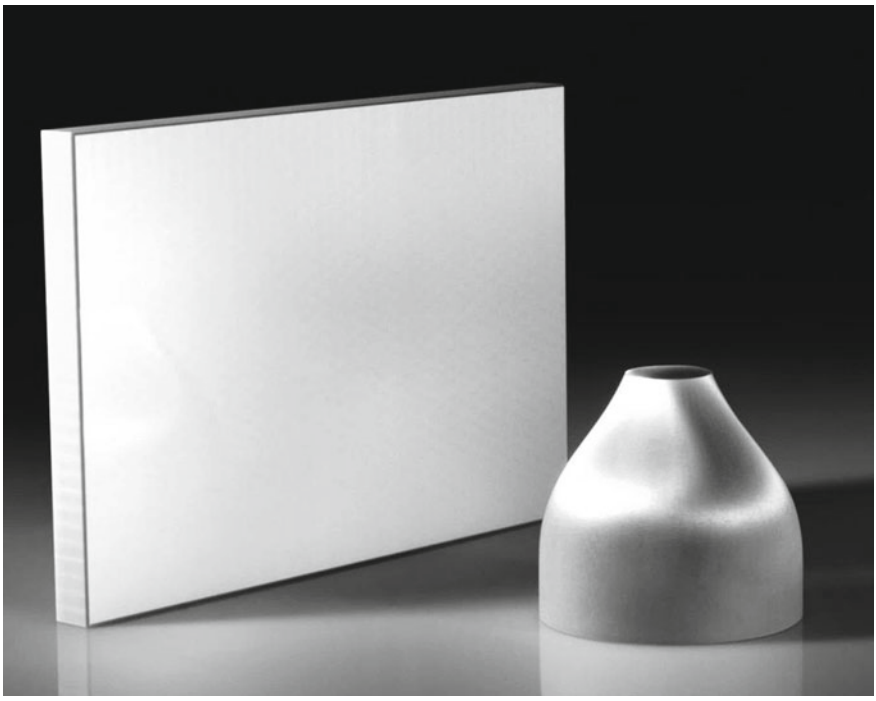

Fig. 4.108 Example of a commercially available fiber optic plate and fiber optic taper (photograph provided by Edmund Optics Japan)

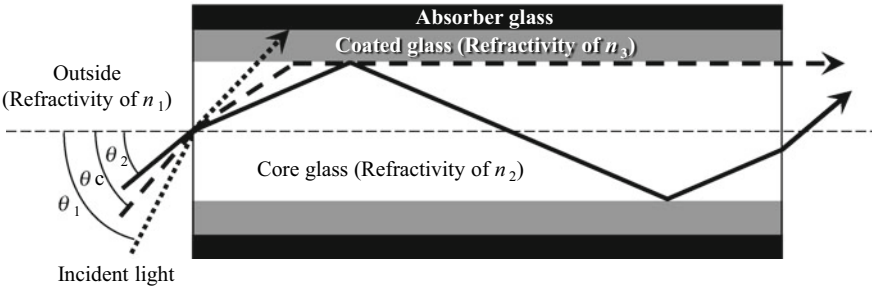

Fig. 4.109 Schematic of the light propagation behavior when visible light is incident to the fibers in the fiber optic plate

to garnet-type aluminum composite oxides, both materials had light emission peak wavelengths that were shorter by 100 nm and had superior stopping power.

The Si included in Re_2SiO_5-type silicates is tetracoordinated due to its sp3 hybrid orbital and its monomer is a regular SiO_4 tetrahedron. For this reason, rare-earth silicates have a structure where the regular SiO_4 tetrahedron encloses the lutetium or

gadolinium atoms. The chemical formula for GSO and LSO are both Re_2SiO_5 but its crystal structure and characteristics are different. GSO belongs to the monocline phase of the space group P2 1/C and its cleavage plane is the (100) plane. The thermal expansion coefficient in the [010] axis is several times larger than in other directions, so brittle fracture due to cleavage can occur during fabrication. Meanwhile, LSO is a monocline of the space group C2/c and has no cleavage planes.

The photon yield of GSO (Ce) is maximal when cerium is 0.5 at.%; the crystal becomes colored when cerium is increased to 1.5 at.%. The decay time decreases when cerium concentration increases. This material has the characteristics of a long rise time at 10–20 ns and a relatively short decay time at 60 ns. Either the Czochralski method or Bridgman-Stockbarger method is used for fabrication.

LSO (Ce) has a shorter decay time than GSO and favorable photon yield. However, the ^{176}Lu included in lutetium generates 240 cps of background noise per cm^3 of LSO [88]. Background due to other radioisotopes caused by Lu_2O_3 used in this context also exists [76]. Furthermore, LSO has been reported to have afterglow lasting for several seconds. The Czochralski method is used for its fabrication. Other than LSO, LYSO has been developed, applying the simple fabrication and low-cost advantages of YSO and partially replacing lutetium with yttrium [76]. The concentration of yttrium in this case can be freely adjusted to 5–70%. The light emission peak wavelength and decay time of LYSO do not significantly vary with LSO; however, significant decreases in stopping power are unavoidable due to the large atomic number differences between lutetium and yttrium. Meanwhile, reports have indicated that the additions of combinations of rare-earth elements have improved the distribution of cerium and increased photon yield [89].

(j) Terbium-Activated GOS

The GOS crystal structure has trigonal symmetry, comprised of three sulfur ions and four oxygen ions joined around the gadolinium ion and the two enclosed gadolinium ions forming a unit lattice. Terbium-activated GOS is a scintillator that applies the light emission that accompanies the 4f–4f transitions due to the trivalent rare-earth ion Tb^{3+} and has the characteristics of an extremely high photon yield and long decay time. Furthermore, it is relatively low-cost as it can be fabricated with chemical reactions between 88% gadolinium oxide and 12% sulfur. Protium, which creates the trivalent rare-earth ion Pr^{3+} or protium with cerium or fluoride additions can be used as activators, as well. Additions of cerium or fluoride aim to reduce the afterglow in exchange for photon yield. Even after considering their limited packing fraction, due to being used in powder form, and their semi-transparency, they are still advantageous in terms of light emission efficiency. A green light emission peak is observed at a 545 nm wavelength when terbium is used as an activator. There are issues with particle diameter/grain diameter due to its use as thick films or as a powder/polycrystal; moreover, there are often limitations due to spatial resolution.

(k) Cadmium tungstate

Cadmium tungstate is an MWO_4 compound referred to as wolframite, which includes a divalent transition metal M and hexavalent tungsten and is monoclinic. The cadmium and tungsten atoms are placed in the center of an extremely distorted octahedron comprised of oxygen atoms. The W-O bonds include 4 short bonds and 2 long bonds. These long and weak bonds, particularly in single-crystal materials, are susceptible to brittle fracture due to cleavage in the (010) plane. Cadmium tungstate is primarily used as thin films with a 50–60-μm thickness. The sol-gel process is applied when thinner scintillators are used.

As mentioned above, cadmium tungstate emits light due to charge transfer. Cadmium tungstate as a scintillator material has a short decay time, no problems with afterglow, and relatively favorable stopping power.

4.4.4 Coupling Between the Camera and Scintillator

Multiple optical lens combinations or glass fibers are used when combining a camera with a scintillator to efficiently guide visible light or to magnify/demagnify an image. An objective lens for microscopes is used for the former. Optical elements that use glass fiber bundles (Fig. 4.110) will primarily be discussed below.

Of the optical devices that use glass fibers, the plate on the left in Fig. 4.108 is referred to as a fiber-optic plate (FOP) and the tapered device on the right in Fig. 4.108 is referred to as a fiber-optic taper (FOT). The material in fiber-optic plates comprises a high-refractive-index glass fiber core inserted in a low-refractive-index coated glass tube, with the gaps between the glass fibers in the core filled in with absorbent glass fibers. This repeatedly undergoes a process of heating the bundle to 500–700 °C and drawing it. The thin glass fiber clumps obtained are cut, processed, and polished, from which a fiber optic plate is formed. In the case of the fiber optic taper, both ends of the cylindrical billet are retained and the central part is stretched while heated. This stretching is stopped when the central neck area obtains the desired magnification, from which two fiber optic tapers can be obtained by cutting at the center. Images are transferred at a magnification factor of 1 between the incidence and emission surfaces of the fiber optic plate. The fiber diameters within the final product are between 6–25 μm and are selected depending on the necessary spatial resolution. Meanwhile, the

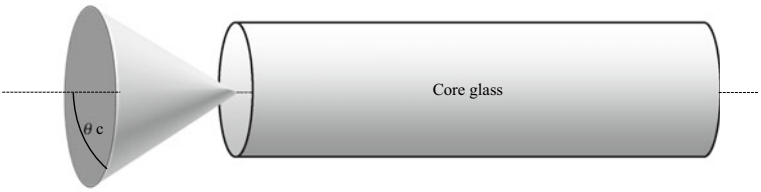

Fig. 4.110 Schematic of the conical region under which the incident light must fall for total reflection to occur within the inner fiber surface when visible light is incident to the fiber of the fiber optic plate

fiber optic taper can magnify or demagnify an image by a factor corresponding to the ratio of the larger and smaller diameters of the fiber optic taper. Generally, the diameter of the end surface is made to match the sensor sizes of a CCD camera or CMOS camera.

Figure 4.109 shows a schematic of the visible light incident to a single fiber. Light incident to the fiber axis at a large angle θ_1 (dotted line arrow in the figure) enters the coated glass from the core glass and then the absorbent glass, whereupon it is absorbed. For this reason, it does not influence adjacent fibers by producing crosstalk. Light incident at an angle θ_c (dashed line arrow in the figure) is propagated along the interface between the core glass and coated glass after entering the former. The term θ_c is the critical angle and light incident at an angle θ_2 smaller than θ_c (solid line arrow in the figure) is propagated within the fiber while repeatedly experiencing total reflection within the inner core glass surface and is guided to the other end surface. In other words, light received on the inner side of the cone in Fig. 4.110 will be efficiently transferred due to the fiber. This critical angle is expressed as follows, with n_1–n_3 as the refractive indices of the external environment, fiber core, and coating material, respectively:

$$NA = \sqrt{n_2^2 - n_3^2} = n_1 sin\theta_c \tag{4.60}$$

Here, *NA* is the *numerical aperture*. Its dependency on the refractive index difference between the core material and coating material can be seen. The numerical aperture of commercially-available fiber optic plates is between 0.35 to 1.0.

Meanwhile, fiber optic tapers are as shown in Fig. 4.111. In the case of Fig. 4.111, the image is magnified by being incident to the small-diameter side and coming out of the large-diameter side. The following relational expression is established when the incidence and emission angles are respectively set as θ_{in} and θ_{out}, and the diameters on the incidence and emission sides are respectively set as d_{in} and d_{out}:

$$d_{in} sin\theta_{in} = d_{out} sin\theta_{ou} \tag{4.61}$$

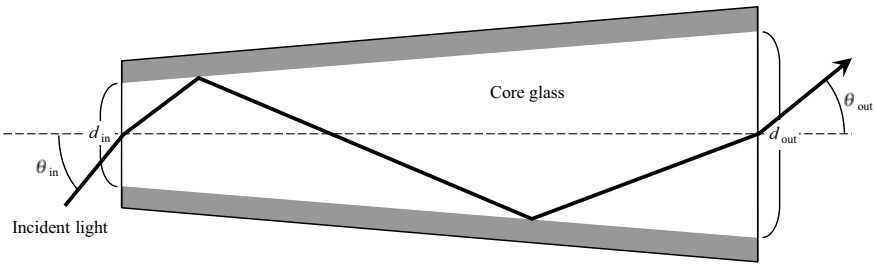

Fig. 4.111 Schematic of light transfer behavior when visible light is incident to a fiber of a fiber optic taper

In other words, the beam narrows in the emission side. Conversely, incidence from the large-diameter side results in the beam being magnified when emitted relative to the incident side.

Images must be minimized with the fiber optic taper when the scintillator size is larger than the sensor size in CCD or sCMOS detectors, such as in industrial X-ray CT scanners. Meanwhile, images produced by X-ray microtomography using synchrotron radiation may conversely need to be magnified. We investigate the former case and analyze efficiency under two scenarios where either an optical lens or fiber-optic taper is used. First, the coupling efficiency η_{OL} when the optical lens is used is as shown below when a powder scintillator is used (assuming a Lambert light source) [91]:

$$\eta_{OL} = \frac{T_L}{1 + 4f^2(1+m)^2} \tag{4.62}$$

Here, T_{L} is the lens transmissivity, f is the f-value determined by dividing the focal distance by the effective diameter, and m is the minification ratio. Generally, T_{L} is 0.7–0.8 at a wavelength of 545 nm [91]. The f-value uses a lens of approximately 1.2. Furthermore, m is approximately 1 to 10. Meanwhile, the transmission efficiency η_{FOT} of the fiber-optic taper is expressed as follows for the same Lambert light source [91]:

$$\eta_{FOT} = \left(\frac{1}{m}\right)^2 \left(\frac{\left(n_2^2 - n_3^2\right)^{1/2}}{n_1}\right)^2 T_F(1 - L_R)F_c \tag{4.63}$$

Here, T_{F} is the transmissivity of the fiber core, L_{R} is the loss at the surface due to Fresnel diffraction, and F_{c} is the fill factor of the fiber core. T_{F} is expressed as follows, with the transmissivity of the fiber core material as μ_{F} and fiber length as l_{F}:

$$T_F = e^{-\mu_F l_F} \tag{4.64}$$

Generally, T_{F} is roughly 0.8, L_{R} is an extremely small value, and F_{c} is approximately 0.85 [91]. Here, we assume $L_{\mathrm{R}} = 0$, $n_1 = 1.0$ (in air), $n_2 = 1.8$, and $n_3 = 1.5$. Figure 4.112 shows a comparison between η_{OL} and η_{FOT}. The numerical aperture, in this case, is approximately equal to 1. When the minification ratio is 2 (i.e. magnification is 0.5), the transmission efficiencies of the fiber-optic taper and optic lens are 16.8% and 1.4%, respectively. The fiber-optic taper is approximately 12 times more efficient than the optic lens. Furthermore, the practical-use range of the fiber-optic taper is below a minification ratio of about 3 when considering the transmission efficiency. In this manner, the photon number per pixel can be increased and the detection system sensitivity can be improved by using the fiber-optic taper. Conversely, the coupling efficiency in the optic lens approximates 0.2 when images must be magnified through coupling during X-ray microtomography using synchrotron radiation; this becomes a level for practical use.

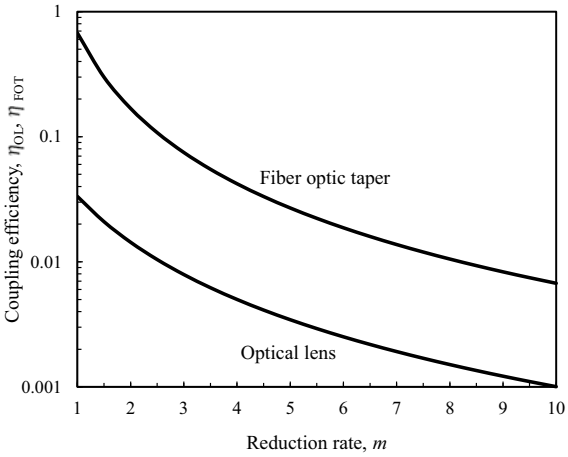

Fig. 4.112 Comparison of coupling efficiencies when using either an optical lens or fiber optic taper

However, considerable accuracy is required for outfitting a fiber optic taper or plate on a detector [85]. CCD cameras are frequently used in a cooled state and need to be outfitted so that they can withstand thermal cycles between room temperatures and operational temperatures. Furthermore, spot and line blemishes caused by the fabrication process (low-sensitivity areas), as well as image distortion, are disadvantages that should be considered.

Glass deterioration due to the X-rays, which transmit through the scintillator, becomes an issue when using an optic lens. For example, Akutagawa et al. reported that the glass surface layer was discolored into a brown color when they were irradiated with soft X-rays that had an energy of 1.24 keV for several hours [90]. Furthermore, reports have indicated that significant irradiation damage appeared in lenses when X-ray energy was 65 keV and exposure 70 s [85]. Glass discoloration is considered removable to some extent using ultraviolet irradiation [73]. As shown in Fig. 4.113, an effective countermeasure against optic glass damage/deterioration is to divide visible light and X-ray paths using visible light mirrors, ensuring that X-rays do not pass through an optic lens. This takes advantage of the fact that X-rays are simply transmitted through the optic lens without being reflected. This countermeasure is widely used in synchrotron radiation facilities. As shown in Fig. 4.114, reports have indicated that ESRF has implemented countermeasures using combinations of convex and concave mirrors [85]. This takes advantage of the fact that X-rays propagate in a virtually straight line, whereas the visible light generated from a scintillator tends to expand outwards. The countermeasures shown in Figs. 4.113 and 4.114 are effective for preventing the damage/deterioration of visible light cameras through the irradiation of X-rays, which have been transmitted through the scintillator.

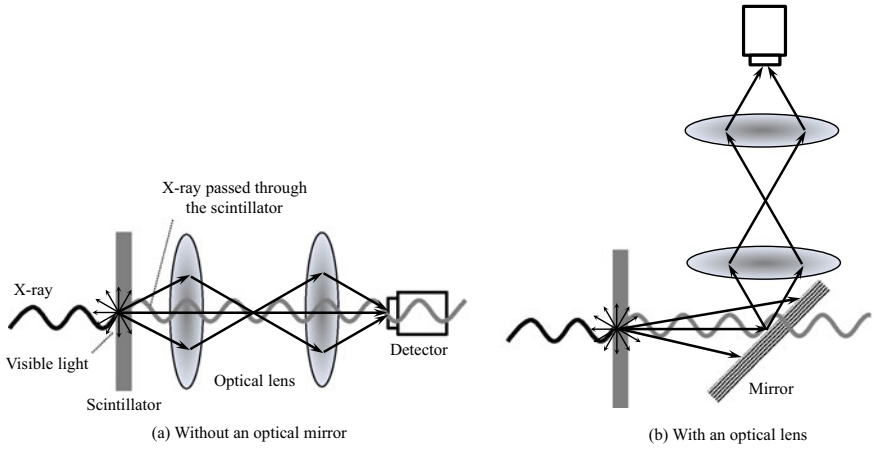

Fig. 4.113 Schematic showing the coupling between the visible light detector, which uses an optical lens, and the scintillator

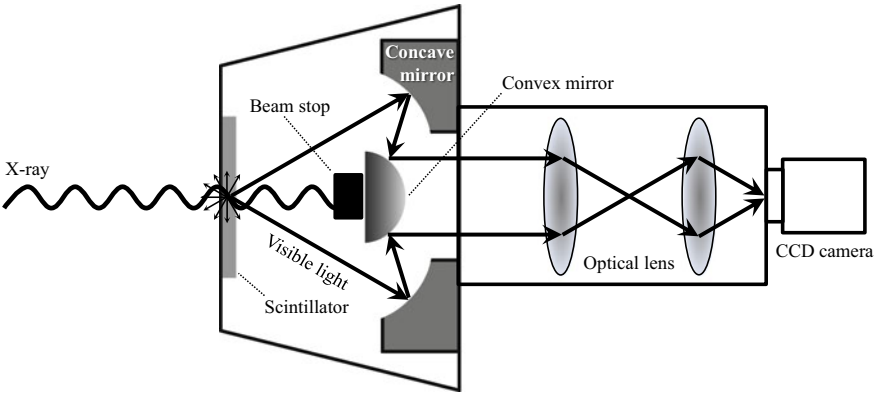

Fig. 4.114 Schematic of a detection system that uses a reflective optical system developed at ESRF [85]

4.4.5 Photon Counting Measurements

The difference between standard X-ray CT scanners and *photon counting*-type (also referred to as "counting-type scanners") X-ray CT scanners is whether they use a *photon-counting detector* (*PCD*). The detectors discussed until now in Sect. 4.4 are so-called *energy integrating detectors* (also referred to as just "integrating detectors"). Energy integrating detectors provisionally convert incident X-rays into visible light, which is then converted to photoelectric charge. As shown in Fig. 4.115a, the amount of photoelectric charge is measured by integrating across only the exposure time and setting that integrated value as the X-ray intensity. Noise influences

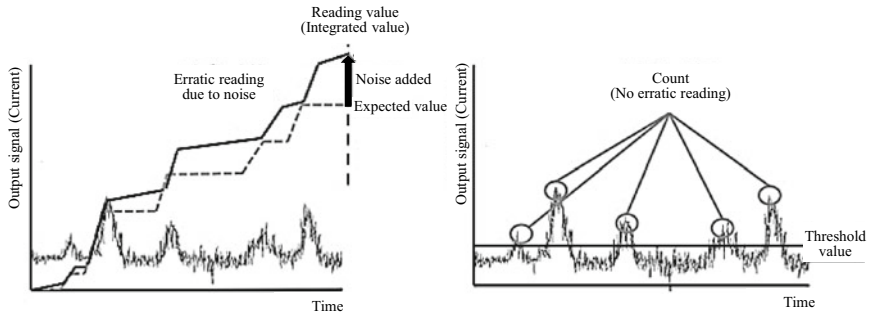

Fig. 4.115 Detection output signal in the energy integrating detector and photon counting detector (courtesy of Akifumi Koike of ANSeeN)

may be strong in this case, particularly when noise is high. Meanwhile, PCDs count each of the photoelectrons generated by incident X-rays, as shown in Fig. 4.115b. Measurements from PCDs are not influenced by the energy of incident X-rays, and an image that is proportional to the number of X-ray photons can be obtained. As a general rule, there is no dynamic range limit and a high dynamic range that follows the measured number of photons can be obtained. Figure 4.116 shows a comparison of images obtained at low light intensity. A cleaner image can be obtained with PCDs even when there is sufficient exposure, as shown in the figure (see example on the furthest right). Favorable images can be obtained with photon-counting even when the exposure drops down to 1/800, whereas the noise becomes so high that the image is no longer recognizable with energy integrating detectors. Furthermore, PCDs can achieve a favorable image even when the pixel size is smaller, thus, higher spatial resolutions can also be achieved with this.

In this manner, measurements with PCDs not only enable noise/artifact control, higher contrast, and higher spatial resolution, but also provide various functional additions to X-ray tomography, including the measurement of X-ray photon energies

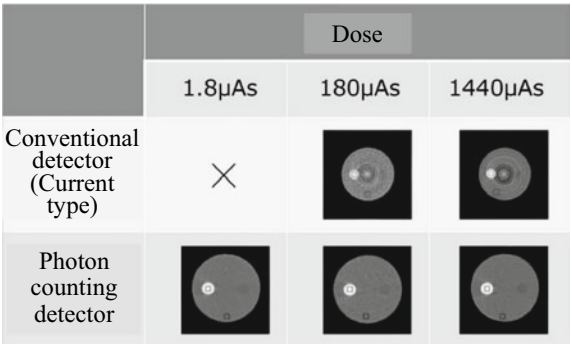

Fig. 4.116 Relationship between the 3D image (cross-section) and dose between an energy integrating detector (conventional) and photon counting detector. The dose is expressed in units of tube current (A) multiplied by exposure time (s) (courtesy of Akifumi Koike of ANSeeN)

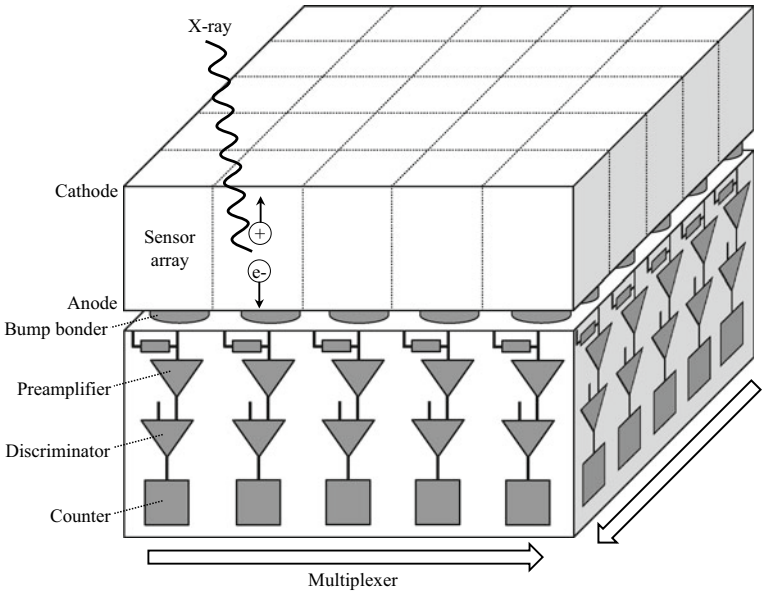

Fig. 4.117 Schematic of the photon counting detector structure

or the mapping of elemental concentrations. In the future, this is suited to become an important device in both medical-use and industrial X-ray CT scanners [92].

(1) Structure

Figure 4.117 shows a schematic of the PCD structure. Semiconductors, which can directly convert X-rays into photoelectric charge (e.g. *cadmium telluride* (CdTe)), are generally used as sensors and a signal processing circuit for photon counting is added. Electron-hole pairs are excited through X-ray incidence. A bias voltage of approximately several hundred V is applied to the sensor and the photoelectric charge is captured by an electrode with a positive voltage. The application of high voltages prevents the rejoining of electrons and holes in the sensor interior, which results in higher measurement accuracy. The semiconductor does not need to be physically divided and the pixel size of the detector can be set up using a smaller electrode. The obtained signal enters an integrated circuit referred to as an *application-specific integrated circuit* (*ASIC*) and amplified with a preamplifier. The number of photons is counted after passing through the pulse formation circuit and divided between pulse and noise using a threshold. This *discriminator* is also used in X-ray photon energy measurements.

(2) Semiconductor

Cadmium zinc telluride and silicon are used in addition to cadmium telluride in direct conversion-type semiconductor detectors used in PCDs. Mercury iodide and gallium

Table 4.15 Representative semiconducting materials used in photon counting detectors and their characteristics [92]

Material	Density (g/cm^3)	Decay distance, $\delta(\mu m)$			E_g (eV)	$\mu\tau(cm^2/V)$		Electron-hole pair creation energy (eV/pair)
		Effective atomic number	20 keV	60 keV		Electron	Hole	
Cadmium telluride (CdTe)	5.85	50	36	107	1.44	3.3×10^{-3}	2×10^{-4}	4.43
Cadmium zinc telluride (Cd0.9Zn0.1Te)	5.78	49	35	110	1.572	$3–5 \times 10^{-3}$	5×10^{-5}	4.64
Silicon (Si)	2.33	14	438	5593	1.12	>1	1	3.62

arsenide have also been reported. The characteristics of these materials are shown in Table 4.15 [93] (the $\mu\tau$ (cm^2/V) value of cadmium zinc telluride is different from that shown in Tables 4.12 and 4.15 but this is thought to be due to material differences and has, therefore, been left as per the original source. Cadmium telluride and cadmium zinc telluride have a stopping power similar to LSO and LuAG, as well as the cesium iodide in Table 4.14. Cadmium telluride has what is referred to as a sphalerite structure. A sphalerite structure is a cubic system where the telluride forms the face-centered cubic lattice and cadmium is placed in tetracoordinated positions of a regular tetrahedron type. Furthermore, the single crystal cleaves along the {110} plane. In contrast, cadmium zinc telluride has a structure where approximately 10% of the cadmium in cadmium telluride is replaced with zinc.

As shown in Eq. (4.51), the electron-hole pair creation energies of these materials are approximately 3 times that of the band gap energy. For example, cadmium telluride has an electron-hole pair creation energy of 4.43 eV/pair, and an average of 4500 electron-hole pairs are created for a single X-ray photon incident at 20 keV of energy. Furthermore, the product of electron lifespan and mobility $\mu_e\tau_e$ is approximately 10^{-3} cm^2/V, which is several orders of magnitude smaller than the value in silicon. $\mu_h\tau_h$ for the hole becomes 1–2 orders of magnitude smaller compared to $\mu_e\tau_e$. Furthermore, $\mu_e\tau_e$ and $\mu_h\tau_h$ multiplied by the electric field strength F correspond to the average transfer distance until the holes and charge are trapped or rejoined. The thickness of the sensor section must be smaller than $\mu_h\tau_h F$ to capture most of the produced charge at the electrode. The charge collection efficiency η_{cc} at a distance from the cathode z is expressed as follows, with the thickness of the sensor section as L_s [93].

$$\eta_{cc} = \frac{\mu_e\tau_e F}{L_s} \tag{4.65}$$

When taking the $\mu_e\tau_e$ and $\mu_h\tau_h$ values of cadmium telluride from Table 4.15 and setting L and F as 100 μm and 1 V/μm, respectively, $\eta_{cc} = 99.9\%$ (contribution of the first term in Eq. (4.65) is approximately 90%) at $z = 10$ μm, $\eta_{cc} = 99.3\%$ at $z =$

50 μm (middle of the thickness direction), and $\eta_{cc} = 98.0\%$ (contribution of the first term in Eq. (4.60) is approximately 10%) at $z = 90$ μm. The differences in charge collection efficiency between the two sides of this thin film show that a higher value is observed on the side where the X-ray is incident on the cathode side and where the charge is collected from the anode side [93].

A phenomenon known as *charge sharing*, where a single photon supplies charge to multiple pixels, occurs in PCDs. Electron sharing induces errors in the X-ray photon count and makes energy information inaccurate. It is important to consider the ratio L_s/w_s between pixel size w_s and L_s and ensure that L_s/w_s is not too large (i.e. the pixel does not become too small) to prevent charge sharing. For example, reports have indicated energy resolution worsened at $L_s/w_s = 10$ and that energy could not be resolved at $L_s/w_s = 18$ when X-rays with 60 keV energy were detected with cadmium telluride [94].

(3) Measurements of X-Ray Energy Spectra

The energy of incident X-rays and photoelectric charge number are generally proportional to one another. The energy of X-ray photons can thus be distinguished when measuring the amount of charge within a range where this proportional relationship is present. As shown in the schematic in Fig. 4.118, a histogram of the X-ray photon

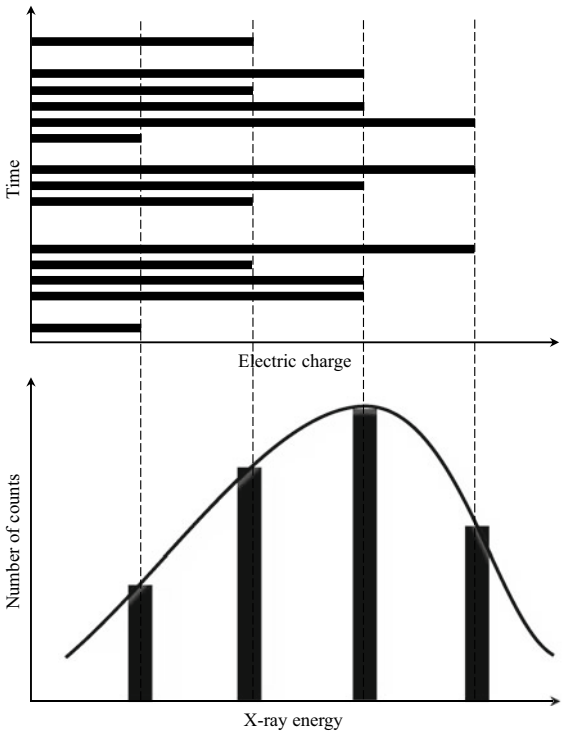

Fig. 4.118 Schematic of the basic principles of X-ray energy spectra measurement using the photon counting detector

energy can be obtained when measurements are continued for a given period. This becomes the energy spectrum of the incident X-ray. Furthermore, projection data for each energy range can be used to highlight the contrast of specified elemental components. Further advancing this, energy discrimination allows for the implementation of absorption edge subtraction imaging methods (discussed later) without using monochromatic X-rays; moreover, 3D mapping of alloy element concentration distributions in a material can be conducted in a simple manner. Furthermore, artifacts (beam hardening) can be controlled by applying X-ray energy discrimination.

4.5 In Situ Observation Devices

X-ray CT scanners have a large advantage in that they can accurately measure the internal structure or outer appearance of actual materials. Furthermore, it is not an exaggeration to state that directly and accurately observing changes in the internal structure of actual materials or parts due to external disturbances can only be completed with X-ray CT scanners. The disturbance to be studied must be recreated on the sample rotation stage of the X-ray CT scanner to realize these observations. This section introduces various devices that make this possible. Many of the devices introduced here are for specialized setups.

The sample rotation stage of the X-ray CT scanner is placed in room temperature and atmospheric pressure in most cases. Furthermore, the X-ray source and detector are frequently placed over several dozen millimeters away from the sample. As such, there is enough space for setting up in situ observational devices compared with electron microscopes. As previously mentioned, the positional accuracy of the sample rotation stage is determined by the spatial resolution necessary from the X-ray CT scanner. A sample rotation stage with higher accuracy generally results in a lower load capacity. Thus, in situ observation devices need to be set up and placed within an acceptable range of load capacity in the sample rotation stage. Furthermore, these may be supplied in an optional or general-use form for industrial X-ray CT scanners.

4.5.1 In Situ Observations of Deformation/Fracture Behavior

Figure 4.119 shows a material testing rig at the author's laboratory, which has primarily been used for X-ray tomography in synchrotron radiation facilities. These are all material testing rigs used in the material science/mechanical engineering disciplines. In most cases, these are used in *time-lapse* in situ *observations*, where observations are made by stopping the load and fixing the deformation, but these can also be used in *full in situ observations* with high-speed tomography, introduced in Sect. 5.3.

Figure 4.119a shows a tension/compression testing machine used since 2003 that applies an actuator that uses compressed air. The load frame which supports load

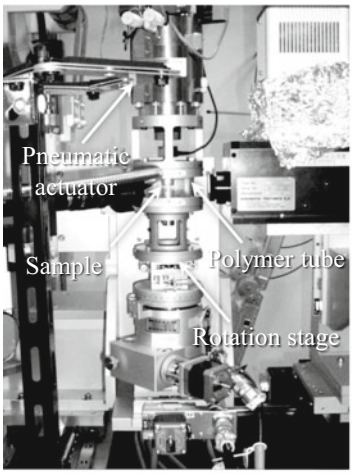

(a) Pneumatic tension/compres-sion testing machine

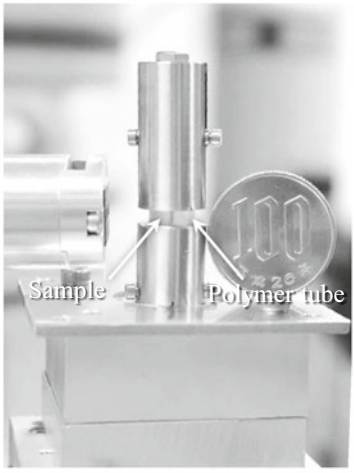

(b) Miniature testing machine for the imaging CT

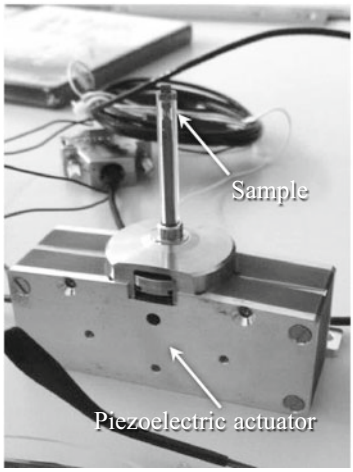

(c) Piezoelectric fatigue testing machine

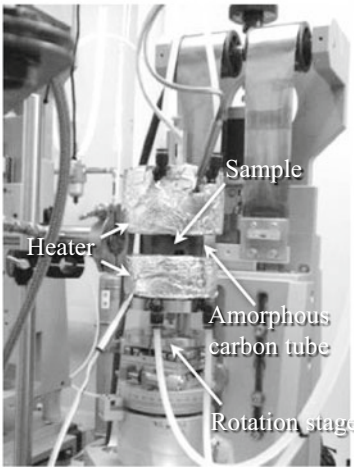

(d) High temperature tension/creep testing machine

Fig. 4.119 Various material testing machines that can be set up on a rotation

does not take the form of a pillar as in typical material testing machines but rather that of a cylinder. The material used is a polymer (polycarbonate) and its thickness is 5 mm. This structure and material satisfy the two conditions of being able to image under consistently equal conditions even when the sample is rotated and with minimal X-ray absorption. Tension, compression, and fatigue tests are conducted with this testing machine under loads of up to 2 kN.

We now consider the implementation of tensile tests of high-strength steel with generated loads of 500 N using this testing machine. For a 0.7 mm by 0.7 mm square area in a gauge section, loads of 1020 MPa and 0.3 MPa are applied to the miniature sample for synchrotron radiation-based X-ray tomography and polymer load frame, respectively. The stress applied to the load frame appears extremely small at first glance. However, the modulus of elasticity of the polycarbonate is 2.25 GPa and that of the steel is larger by a factor of approximately 100. For this reason, the elastic elongation of the steel sample in the 1-mm distance gauge length is approximately 4.9 μm, whereas the elastic deformation of the approximately 40-mm high polycarbonate part is roughly 5.7 μm. This is far removed from typical material tests, where the sample device stiffness is extremely high and does not deform. In contrast with this deformation of the testing machine, the material testing rig in Fig. 4.119a is controlled to a total weight of 5 kg and both the eccentricity and surface runout amount of the sample rotation stage are minimized to maintain a spatial resolution of approximately 1 μm. This testing device is available at BL20XU in SPring-8; interested parties should contact the author. Furthermore, the load capacity of the sample rotation stage becomes even more strict when high spatial resolutions are obtained with X-ray microscopy. Figure 4.119b is a manual testing machine that was miniaturized by removing as much weight as possible from the machine.

A fatigue testing machine with a piezoelectric actuator is used when strokes are not necessary, an example is shown in Fig. 4.119c. Furthermore, a testing machine with a heater attached is used for observations at high temperatures, as shown in Fig. 4.119d. These have been used to successfully conduct in situ observations of creep deformation behavior in aluminum alloys at a temperature of 500 °C [95]. An amorphous carbon cylinder whose X-ray absorption is as small as a polymer is used as a load frame in these cases.

4.5.2 In Vivo Observations of Living Bodies

Drug development requires animal experimentation with small animals whose specified genes can be easily altered; moreover, it is important to be able to image the insides of their bodies while still alive at a high resolution. Figure 4.120 shows a schematic where synchrotron radiation was used as an X-ray source to conduct dynamic 3D observations of the coronary arteries and bronchioles in living rats and mice [96]. To conduct in vivo *observations* (referring to the observations of living bodies) in small animals, their airway pressure and electrocardiograms must be constantly monitored and transmission images are continuously taken while coordinating the opening/closing of the X-ray shutter and exposure start timing with airway pressure and electrocardiogram signals. This can significantly reduce motion artifacts due to small movements of the living body. In these cases, high-speed X-ray shutters have been introduced to minimize the radiation dose in animals as much as possible.

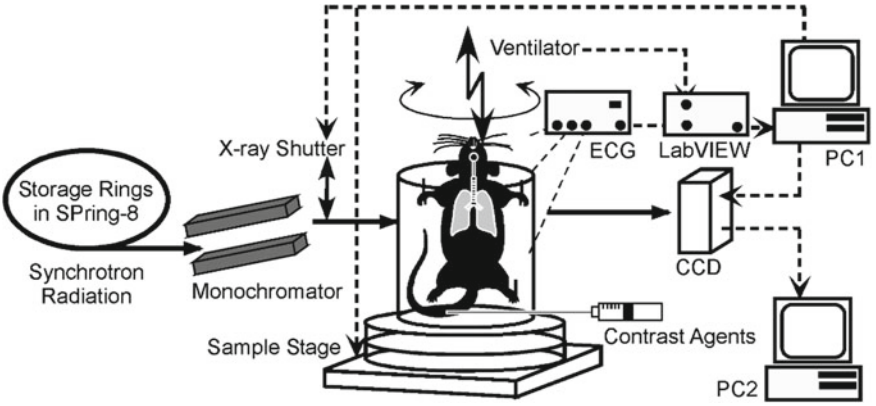

Fig. 4.120 Overview of high-resolution in-vivo CT system (courtesy of Professor Toshihiro Sera of Kyushu University)

References

1. K. Sanderson, Nature digest, **5** (2008). https://doi.org/10.1038/ndigest.2008.081211
2. C.G. Camara, J.V. Escobar, J.R. Hird, S.J. Putterman, Nature **455**, 1089–1092 (2008)
3. C.A. Clark, Los alamos/tribogenics create highly portable imaging system, Los Alamos Daily Post (2013). June 26. http://www.ladailypost.com/content/los-alamostribogenics-create-highly-portable-imaging-system
4. J.M. Boone, J. Beutel, H.L. Kundel, R.L. VanMetter (eds.). *Handbook of Medical Imaging*, Bellingham, Washington, SPIE Press, 1, 78 (2000)
5. H.A. Kramers, Phil. Mag. **46**, 836–871 (1923)
6. T.M. Buzug, *Computed Tomography: From Photon Statistics to Modern Cone-Beam CT* (Springer, Berlin, Germany, 2008)
7. Chemical Society of Japan, Ed.: Structure of Materials III: Diffraction, Fifth Series of Experimental Chemistry Vol. 11, Maruzen, (2006), ISBN 9784621073100
8. International Tables for X-Ray Crystallography, Vol.3, Physical and Chemical Tables, editors C.H. Macgillavry and G.D. Rieck, D. Reidel Publishing Company, (1985). (published online http://xdb.lbl.gov/xdb.pdfhttp://xdb.lbl.gov/xdb. Accessed August 2017
9. Japan Institute of Metals and Materials, Ed.: Metals Databook, Revised 4th Edition, Maruzen, Co., Ltd., (2004), 228
10. O.W. Richardson, Philosophical of the Cambridge Philosophical Society **11**, 286–295 (1901)
11. M.N. Avadhanulu, P.G. Kshirsagar, *A Textbook of Engineering Physics* (S Chand & Co., Ltd., New Delhi, 1992), p. 348
12. M. Hagino, Surf. Sci. **8**, 472–479 (1987)
13. T.M. Buzug, *Computed tomography: from photon statistics to modern cone-beam CT* (Springer, Berlin, Germany, 2008), pp. 18–19
14. L.A.G. Perini, P. Bleuet, J. Filevich, W. Parker, B. Buijsse, L.F.Tz. Kwakman, *Review of Scientific Instruments*, 88 (2017), 063706-1-10
15. G.G. Poludniowski, P.M. Evan, Med. Phys. **34**, 2164–2174 (2016)
16. T. Fujita, H. Anno, Toshiba Rev. **66**, 24–28 (2011)
17. E. Lassner, W.-D. Schubert, *Tungsten: Properties, Chemistry, Technology of the Element, Alloys, and Chemical Compounds* (Kluwer Academic/Plenum Publishers, New York, 1999), pp. 256–258
18. Y. Mutoh, K. Ichikawa, K. Nagata, J. Soc. Mater. Sci. Japan **40**, 882–888 (1991)

19. R.L. Sproull, W.A. Phillips, *Modern Physics: The Quantum Physics of Atoms, Solids, and Nuclei*, 3rd edn. (Dover Publications, New York, 1980), p. 455
20. S. Yamamoto, H. Aoyama, Toshiba Rev. **69**, 57–59 (2014)
21. H. Sugie, M. Tanemura, V. Filip, K. Iwata, K. Takahashi, F. Okuyama, Appl. Phys. Lett. **78**, 2578–2580 (2001)
22. W. Sugimoto, S. Sugita, Y. Sakai, H. Goto, Y. Watanabe, Y. Ohga, S. Kita, T. Ohara, J. Appl. Phys. **108**, 044507 (2010)
23. Comcraft website: http://www.comcraft.co.jp/products/05.html. Accessed August 2017
24. Matsusada Precision website: https://www.matsusada.co.jp/product/xm/xunit/. Accessed August 2017
25. Hamamatsu Photonics website: http://www.hamamatsu.com/jp/ja/product/category/1001/3028/index.html. Accessed August 2017
26. Japanese Inspection Instruments Manufacturers' Association: Association-handled product information. http://www.jima.jp/content/assen.html#assen_d. Accessed August 2017
27. M. Ito, Radioisotopes **52**, 699–703 (2003)
28. M.M. Nasseri, Nuclear Eng. Technol. **48**, 795–798 (2016)
29. R.W. Hamm, M.E. Hamm, *Industrial Accelerators and their Applications* (World Scientific, Singapore, 2012), pp. 307–369
30. H.E. Martz, C.M. Logan, D.J. Schneberk, P.J. Shull, *X-Ray Imaging: Fundamentals* (CRC Press, Boca Raton, Industrial Techniques and Applications, 2017), pp. 176–177
31. G. Claus, *Introduction to radiation protection: practical knowledge for handling radioactive sources* (Springer, Berlin, 2010), pp. 323–325
32. J. Davis, P. Wells, Industrial Metrology **2**, 195–218 (1992)
33. R. Hoffmann, T. Kögl, Flow Meas. Instrum. **53**, 147–153 (2017)
34. M.S. Rapaport, A. Gayer, NDT&E International **24**, 141–144 (1991)
35. D.C. Copley, J.W. Eberhard, G.A. Mohr, JPM, 15–26 (1994)
36. C. Rizescu, C. Besliu, A. Jipa, Nuclear Instrum. Methods Phys. Res. A **465**, 584–599 (2001)
37. SPring-8 website: http://www.spring8.or.jp/ja/about_us/whats_sp8/facilities/accelerators/ http://www.spring8.or.jp/ja/about_us/whats_sp8/facilities/accelerators/, etc. Accessed September 2017
38. K. Kora, editor-in-chief: Synchrotron Radiation in Practical Use, Council for the Promotion of Photon Science Technologies, Nikkan Kogyo Shimbun (1997)
39. T. Kaneyasu, Y. Takabayashi, Y. Iwasaki, S. Koda: Proceedings of The 12th International Conference on Accelerator and Large Experimental Control System, Kobe, pp. 307–309 (2009)
40. Y. Takashima, M. Hosaka, N. Yamamoto, K. Takami, T. Takano, A. Mano, H. Morimoto, M. Katoh, Y. Hori, S. Sasaki, S. Koda, Y. Takeda: Proceedings of the 10th Annual Meeting of Particle Accelerator Society of Japan, Nagoya, pp. 385–387 (2013)
41. H. Yonehara, Journal of the Japanese society for synchrotron. Radiat. Res. **16**, 178–185 (2003)
42. T. Asaka, H. Dewa, H. Hanaki, T. Kobayashi, A. Mizuno, S. Suzuki, T. Taniuchi, H. Tomizawa, K. Yanagida, Proceedings of EPAC 2002, Paris, France, pp. 2685–2687 (2002)
43. H. Yonehara: SPring-8 user information, highlights, 2, 1–14 (1997)
44. K. Wille, Rep. Prog. Phys. **54**, 1005–1068 (1991)
45. Council for the Promotion of Photon Science Technologies (K. Kora, Ed.): Synchrotron Radiation in Actual Use, Nikkan Kogyo Shimbun (1997)
46. H. Wiedemann, *Synchrotron Radiation* (Springer, Berlin, 2003)
47. S. Kikuta, *X-Ray Scattering and Radiation Science* (Tokyo University Press, Fundamentals, 2011)
48. H. Tanaka, H. Ohkuma: SPring-8 user information, 298–304 (2003)
49. T. Tomimasu, *Synchrotron Radiation Technologies.* Kogyo Chosakai Publishing pp. 131–133 (1990)
50. Y. Sakurai, H. Kitamura, *SPring-8 User Information*,pp. 6–8 (1997)
51. K. Uesugi, *(Riken SPring-8 Center): Personal Communication* (2017)
52. H. Ohashi, K. Hirano (Eds.), Introduction to radiation beamline optics—for first-time radiation users. Japanese Society for Synchrotron Radiation Research (2008)

53. Y. Kashihara, JAERI-M Report, 91-008, Japan Atomic Energy Research Institute (1991)
54. E.L. Nickoloff, H.L. Berman, Radiographics **13**, 1337–1348 (1993)
55. C. Engblom, Overview of some feedback- & control systems in synchrotron SOLEIL. In The 11th International Workshop on Personal Computers and Particle Accelerator Controls (PCaPAC), Brazil (2016)
56. A. King, N. Guignot, P. Zerbino, E. Boulard, K. Desjardins, M. Bordessoule, N. Leclerq, S. Le, G. Renaud, M. Cerato, M. Bornert, N. Lenoir, S. Delzon, J.-P. Perrillat, Y. Legodec, J.-P. Itié, Rev. Sci. Instrum. **87**, 093704 (2016)
57. H. Toda, M. Kobayashi, Y. Suzuki, A. Takeuchi, K. Uesugi, Microscopy **44**(2009), 199–205 (2009)
58. S.M. Gruner, J.R. Milch, G.T. Reynolds, IEEE Trans. Nucl. Sci. **25**, 562–565 (1978)
59. C. Ponchut, Journal Synchrotron Radiation **13**, 195–203 (2006)
60. K. Ito, Y. Amemiya, N. Sakebe, Development of Array-CCDX line detector and protein crystal structure analysis applications. In Proceedings of the Joint Symposium on the 13th Annual Meeting of Japan Synchrotron Radiation Society and Synchrotron Radiation Science, 9-P-60 (2001)
61. M. Tomizawa, J. Japanese Soc. Non-destructive Inspection **63**, 221–231 (2014)
62. M. Abe (Contr.), A. Ota (Ed.): Latest Trends in CMOS Image Sensors—From High Performance, High Functionality, to Application Developments,CMC Publishing, 10 (2014)
63. D.J. Denvir, C.G. Coates, Proc. SPIE., *Biomedical Nanotechnology Architectures and Applications*, 4626, 502–512 (2002)
64. Hamamatsu Photonics: Photosemiconductor Element Handbook, https://www.hamamatsu.com/resources/pdf/ssd/05_handbook.pdf. Accessed January 2018
65. Y. Kimura, Microscopy **45**, 257–263 (2010)
66. H. Shibata, *Design Wave Magazine*, 128–129 (2009)
67. T. Kuroda, *Journal of the Institue of Image Information and Television Engineers*, 68, 216–222 (2914)
68. S. Risticj, Proceedings of Goran Conference on medical physics and biomedical engineering. Macedonia, 65–71 (2013)
69. S. Kasap, J.B. Frey, G. Belev, O. Tousignant, H. Mani, J. Greenspan, L. Laperriere, O. Bubon, A. Reznik, G. DeCrescenzo, K.S. Karim, J.A. Rowlands, Sensors **11**, 5112–5157 (2011)
70. T. Yamasaki, J. Soc. Photographic Sci. Technol. Japan **70**(separate issue), 24–25 (2007)
71. Physical Measurement Laboratory (PML), National Institute of Standards and Technology (NIST): X-Ray Form Factor, Attenuation and Scattering Tables, NIST, U.S. Commerce Department, USA, (2011). https://www.nist.gov/pml/x-ray-form-factor-attenuation-and-scattering-tables. Accessed January 2018
72. G. Bizarri, J. Cryst. Growth **312**, 1213–1215 (2010)
73. Y. Suzuki (part-time lecturer at Tokyo University, formerly of Japan Synchrotron Radiation Research Institute), personal communication
74. T. Jing, A. Goodman, J. Drewery, G. Cho, W.S. Hong, H. Lee, S.N. Kaplan, V. Perez-Mendez, D. Wildermuth, Nucl. Instrum. Methods Phys. Res., Sect. A **368**, 757–764 (1996)
75. A. Yoshikawa, FBNews No. 463, 1–6 (2015)
76. G.F. Knoll, *Radiation Detection and Measurement*, 4th edn. (Wiley India, Noida, Uttar Pradesh, 2011)
77. K. Saegusa, T. Irifune, M. Fukushi, H. Saitoh, G. Nakaya, *Basic Radiation Metrology*, Iryo Kagaku Co. (2001)
78. S.R. Cherry, J.A. Sorensen, M.E. Phelps, *Physics in Nuclear Medicine*, 4th edn. (Elsevier, Philadelphia, 2012)
79. P.A. Rodny, *Physical Processes in Inorganic Scintillators* (CRC Press, Boca Raton, FL, 1997)
80. G. Blasse, B.C. Grabmaier, *Luminescent materials* (Springer-Verlag, Berlin, 1994)
81. C.L. Melcher, J.S. Schweitzer, A. Liberman, J. Simonetti, IEEE Trans. Nucl. Sci. **32**, 529–532 (1985)
82. M. Laval, M. Moszynski, R. Allemand, E. Carmoreche, P. Guinet, R. Odru, J. Vacher, Nucl. Instrum. Meth. Phys. **206**, 169 (1983)

83. E.V.D. van Loef, P. Dorenbos, C.W.E. van Eijk, K.W. Kraemer, H.U. Guedel, Appl. Phys. Lett. **79**, 1573 (2001)
84. T. Suzuki (National Institute of Radiology Sciences): *Recent Trends in Scintillators*, 6th Annual JRSM Symposium, 120–122 (2011)
85. H. Graafsma, T. Martin, *Advanced Tomographic Methods in Materials Research and Engineering*, ed. John Banhart, Oxford University Press, (2008), Section 10
86. M.S. Alekhin, J. Renger, M. Kasperczyk, P.-A. Douissard, T. Martin, Y. Zorenko, D.A. Vasilév, M. Stiefel, L. Novotny, M. Stampanoni, Opt. Express **25**, 1251–1261 (2017)
87. K. Takagi, T. Fukazawa, Appl. Phys. Lett. **42**, 43–45 (1983)
88. C.L. Melcher, J.S. Schweitzer, Nuclear instruments and methods in physics research section a: accelerators. Spectrometers Detectors Assoc. Equip. **314**, 212–214 (1992)
89. L. Qin, G. Ren, S. Lu, D. Ding, H. Li, IEEE Trans. Nucl. Sci. **55**, 1216–1220 (2008)
90. J. Akutagawa, D. Yamamoto, W. Pong, J. Electron Spectrosc. Relat. Phenom. **82**, 75–77 (1996)
91. S. Hejazi, D.P. Trauernicht, Med. Phys. **24**, 287–297 (1997)
92. K. Kan, Y. Imura, H. Morii, K. Kobayashi, T. Minemura, T. Aoki, World J. Nuclear Sci. Technol. **3**(2013), 106–108. https://doi.org/10.4236/wjnst.2013.33018. published online
93. P. Russo, A.D. Guerra, Chapter 2 "Solid-State Detector for Small-Animal Imaging", Molecular Imaging of Small Animals Instrumentation and Applications, Edited by H. Zaidi, Springer, New York (2014)
94. K. Spartiotis, A. Leppänen, T. Pantsar, J. Pyyhtiä, P. Laukka, K. Muukkonen, O. Maännistö, J. Kinnari, T. Schulman, Nucl. Instrum. Methods Phys. Res., Sect. A **550**, 267–277 (2005)
95. H. Toda, Z.A.B. Shamsudin, K. Shimizu, K. Uesugi, A. Takeuchi, Y. Suzuki, M. Nakazawa, Y. Aoki, M. Kobayashi, Acta Mater. **61**, 2403–2413 (2013)
96. T. Sera, H. Yokota, K. Fujisaki, K. Fukasaku, H. Tachibana, K. Uesugi, N. Yagi, R. Himeno, Phys. Med. Biol. **53**, 4285–4301 (2008)